Evolution of space weathering and its components – effect of solar wind and microimpacts on reflectance spectra of airless planetary surfaces

KATEŘINA FLANDEROVÁ

ACADEMIC DISSERTATION
To be presented, with the permission of the Faculty of Science of the University of Helsinki, for public examination in auditorium E204, Physicum, Kumpula campus, on the 4th of November 2022, at 1 p.m.

DEPARTMENT OF GEOSCIENCES AND GEOGRAPHY A107 / HELSINKI 2022

Cover photo: Kateřina Flanderová (Spectral measurements of laser-irradiated olivine.)

Author´s address: Kateřina Flanderová
Department of Geosciences and Geography
P.O.Box 64
00014 University of Helsinki, Finland
katerina.chrbolkova@helsinki.fi

Supervised by: Docent Tomáš Kohout
Department of Geosciences and Geography
University of Helsinki, Finland

Professor Ilmo Kukkonen
Department of Geosciences and Geography
University of Helsinki, Finland

Docent Josef Ďurech
Astronomical Institute of Charles University
Charles University, Czech Republic

Reviewed by: Professor Ian Garrick-Bethell
Earth & Planetary Sciences Department
University of California, California, United States of America

Senior scientist Faith Vilas
Planetary Science Institute, Arizona, United States of America

Opponent: Senior scientist Amanda Hendrix
Planetary Science Institute, Arizona, United States of America

ISSN 1798-7911
ISBN 978-951-51-8149-7 (paperback)
ISBN 978-951-51-8150-3 (PDF)
http://ethesis.helsinki.fi

Unigrafia
Helsinki 2022

This dissertation is the result of a double doctorate program carried out at:

UNIVERSITY OF HELSINKI
FACULTY OF SCIENCE

University of Helsinki
Faculty of Science
Department of Geosciences and Geography
Helsinki, Finland

and

FACULTY
OF MATHEMATICS
AND PHYSICS
Charles University

Charles University
Faculty of Mathematics and Physics
Astronomical Institute of Charles University
Prague, Czech Republic

“It doesn’t stop being magic just because you know how it works.”

(Terry Pratchett, The Wee Free Men)

Flanderová K., 2022. Evolution of space weathering and its components – Effect of solar wind and microimpacts on reflectance spectra of airless planetary bodies. Unigrafia. Helsinki. 37 pages and 8 figures.

Abstract

Our knowledge about mineralogy and physical conditions on airless planetary bodies in the Solar system is based mainly on remotely captured reflectance spectra. However, reflectance spectra are influenced by many effects, a major one is the space weathering.

The term space weathering refers to a set of processes, also called space weathering agents, mainly the solar wind irradiation and micrometeoroid impacts, which on long timescales darken the surfaces and alter reflectance spectra of airless bodies. Here, I focused on finding the difference between the effect of the two, above-mentioned, space weathering agents on reflectance spectra of silicate-rich airless planetary bodies.

Firstly, I studied areas of magnetic anomalies on the Moon, so-called lunar swirls. The swirls' spectra are influenced mostly by micrometeoroid impacts. I compared these spectra to spectra of surrounding areas, influenced by both the space weathering agents. The results suggested that there is a difference in the effect of micrometeoroid impacts and the combination of the two space weathering agents. There are also additional effects that contribute to the evolution of spectra on the Moon, such as the position with respect to the near and far side, which relates to the shape of Earth's magnetotail and an increased shielding of the solar wind ions.

During the laboratory experiments, I, with the help of colleagues, irradiated pellets made of silicates typically found on airless planetary bodies, i.e. olivine and pyroxene. To simulate the effect of solar wind, I used ions of H, He, and Ar. To simulate micrometeoroid bombardment, I used individual femtosecond laser pulses. The main conclusions were that the difference between the two space weathering agents can be seen mainly in the longer near-infrared (NIR) wavelengths (around 2 μm). Micrometeoroid impacts cause greater changes there, resulting in smaller spectral slope changes. Otherwise, the original mineralogy seemed to influence the way the weathering proceeds more significantly, which agrees with previous studies and also with observations of A-type asteroids or asteroids (4) Vesta and (433) Eros.

The differences in irradiated samples were then analysed on micro-scale using electron microscopy. Ion irradiation caused only mild blistering on the surface while laser irradiation caused extended melting with associated melt splashes. The subsurface changes were also different. Ion irradiations induced vesiculation in partially amorphised topmost layers of the samples. Laser irradiation induced creation of the nanophase iron ($npFe^0$) particles in the olivine sample, but not in the pyroxene sample. Changes in ion-irradiated samples caused alterations in the visible spectral slope, while $npFe^0$ particles in laser-irradiated olivine also altered the NIR spectral slope. The pyroxene sample irradiated by laser showed only a significant amorphous layer full of large vesicles. The spectral slope did not change as a result, the sample only showed alteration of the absorption bands. This analysis highlighted the significance of wavelength-sized structures on the resulting reflectance spectra.

Based on these results, I gained an insight into the evolution of the spectra and subsurface structures. Nevertheless, more simulations on different minerals are needed to gain a complete understanding of the space weathering mechanism.

Abstrakt (Abstract in Czech)

Naše znalosti o mineralogii a podmínkách na malých tělesech ve Sluneční soustavě pocházejí především z naměřených reflektančních spekter, která jsou ale ovlivněna mnoha efekty. Jeden z hlavních je kosmické zvětrávání.

Kosmické zvětrávání ovlivňuje povrchy, a tedy i spektra malých těles na dlouhých časových škálách. Způsobují ho dva hlavní procesy: ozařování slunečním větrem a dopady mikrometeoritů. V této práci jsem se soustředila na porovnání vlivu těchto dvou procesů na spektra asteroidů bohatých na silikáty.

Nejprve jsem zkoumala spektra měsíčních swirlů, kde ve zvětrávání dominují mikroimpakty. Porovnávala jsem spektra ze swirlů s okolními oblastmi, které ovlivňují oba zvětrávací procesy. Ukázalo se, že mikroimpakty ovlivňují spektra jinak než sluneční vítr. Kromě toho jsem objevila, že swirly na přivrácené a odvrácené straně Měsíce vykazují odlišné trendy z důvodu stínění přivrácené strany Měsíce asymetrickým magnetickým polem Země.

Během laboratorních experimentů jsem, ve spolupráci s kolegy, ozařovala peletky vyrobené ze silikátů, které se běžně vyskytují ve Sluneční soustavě, tj. olivínu a pyroxenu. Vliv slunečního větru jsem simulovala ozařováním ionty H, He a Ar. Vliv mikroimpaktů byl realizován pulzy femtosekundového laseru. Z pořízených spekter bylo jasné, že v oblasti okolo 2 μm se tyto dva procesy odlišují. Reflektance se u laserem ozářeného materiálu zmenšila v dané oblasti mnohem více než u toho ozářeného ionty, což způsobilo menší změnu spektrálního sklonu. Kromě popsané změny se ale zdá, že mnohem více závisí na ozařovaném materiálu, než na způsobu ozáření. Moje výsledky souhlasí např. s pozorováními asteroidů typu A nebo asteroidů (4) Vesta a (433) Eros.

Rozdíly mezi vzorky jsem poté zkoumala za využití elektronového mikroskopu. Zatímco povrchy peletek ozářených ionty vykazovaly přítomnost puchýřů, laserem ozářené vzorky obsahovaly velké množství nataveného a rozstříknutého materiálu. Také podpovrchové změny byly pro dva zkoumané způsoby ozáření jiné. Ve vzorcích ozářených ionty byly identifikovány podpovrchové puchýře a částečná amorfizace vrchních vrstev. V důsledku toho došlo ke změnám spektrálního sklonu ve viditelné oblasti. Laserem ozářený olivín obsahoval částice nanoželeza (npFe^0), které způsobily změnu sklonu spektra také v blízké infračervené oblasti. V laserem ozářeném pyroxenu byla patrná tlustá vrstva plně amorfního materiálu s velkými puchýři. V důsledku těchto struktur se nezměnil sklon spektra, pouze hloubka absorpčních pásů. Je tedy vidět, jaký význam mají struktury o velikosti srovnatelné s vlnovou délkou pozorování na výsledná spektra.

Získané výsledky nás posunuly v chápání vývoje reflektančních spekter a podpovrchových struktur v důsledku kosmického zvětrávání. Nicméně k úplnému pochopení problematiky je zapotřebí provést další experimenty s využitím jiných minerálů.

Acknowledgements

First of all, I would like to show my gratitude to my supervisors. Having difficulty naming either one in the first place, I decided to go alphabetically. Dr. Josef Ďurech has always been ready to discuss with me and give me hints on how to proceed further. His calm, patient, and friendly approach really helped me to get to this point. My thanks belong in the same extent to my second supervisor, Dr. Tomáš Kohout. It was he, who pushed me to aim at higher goals than I would set myself and thanks to him I decided to travel to Finland. I highly value the expertise of both my supervisors and cannot express how much I learned from them.

I would also like to highlight the contribution of Prof. Ilmo Kukkonen and Prof. David Vokrouhlický, who were always truly kind to me and supported me in conducting my thesis in the cotutelle regime, even though I was the first one at the Astronomical institute doing so. Additionally, I would like to thank Dagmar Zádrapová and Dr. Mia Kotilainen for their help with preparing the cotutelle agreement.

Among the co-authors, I would like to emphasize the input of Dr. Rosario Brunetto, who especially during preparations of the second manuscript devoted a significant amount of his time to discussions with me and, for me, unofficially, became my third supervisor. I would also like to appreciate the contribution of Dr. Antti Penttilä, Dr. Cateline Lantz, Prof. Petr Malý, Dr. Václav Dědič, Dr. Patricie Halodová, Dr. Kenichiro Mizohata, Dr. František Trojánek, Dr. Alessandro Maturilli, Stefano Rubino, and others who are not named here, but helped me with preparation and execution of the experiments, which are an important part of this dissertation.

My studies and experiments would not proceed to the extent they did, if it were not for funding from the University of Helsinki Foundation, Vilho, Yrjö and Kalle Foundation of the Finnish Academy of Science and Letters, GeoDoc doctoral programme, and DONASCI Travel grants.

I am also grateful to Dr. Pasi Heikkilä, Dr. Anu Kaakinen, Dr. Seija Kultti, Prof. Tapani Rämö, and Dr. Aku Heinonen for introducing me, with no previous background, to the field of geology and for preparing materials in English for me.

Dr. Maria Gritsevich and Dr. Johanna Salminen, thank you very much for agreeing to be my thesis committee. We discussed only a few times, but it evoked a genuinely nice and secure feeling that there is someone who supports me, and I can ask for help if needed.

I cannot omit all wonderful fellow students with whom I spent the majority of my time. From Helsinki this would be especially Dr. Juulia Gabrielle Moreau, Dr. Liisa Ilvonen, Dr. Henrik Kalliomäki, Dr. Radoslaw Michallik, and many others. From Prague I would like to thank Jan Kára, Dr. Jaroslav Merc, and Dr. Ondřej Chrenko for amazing time spent together in one office and during our tea breaks. I would also like to thank Dr. David Korda, Dr. Daniela Korčáková, Nela Dvořáková, and others for nice time we spent together.

Last, but not least, I would like to show my gratitude to my family, mainly to my parents, my sister, and my wonderful husband. Without them, I would not have written this thesis today.

Contents

List of original publications

This thesis is based on the following publications:

I **Chrbolková, K.***, Kohout, T., and Ďurech, J. (2019). Reflectance spectra of seven lunar swirls examined by statistical methods: A space weathering study. *Icarus*, 333, 516-527.

II **Chrbolková, K.***, Brunetto, R., Ďurech, J., Kohout, T., Mizohata, K., Malý, P., Dědič, V., Lantz, C., Penttilä, A., Trojánek, F., and Maturilli, A. (2021). Comparison of space weathering spectral changes induced by solar wind and micrometeoroid impacts using ion- and femtosecond-laser-irradiated olivine and pyroxene. *Astronomy & Astrophysics*, 654, A143.

III **Chrbolková, K.*,** Halodová, P., Kohout, T., Ďurech, J., Mizohata, K., Malý, P., Dědič, V., Penttilä, A., Trojánek, F., and Jarugula, R. (2022). Sub-surface alteration and related change in reflectance spectra of space-weathered materials. *Astronomy & Astrophysics*, 665, A14.

*maiden name: **Chrbolková K.**, married name: **Flanderová, K.**
The publications are referred to in the text by their roman numerals.

Author's contribution to the publications

I	Study design:	T. K. and **K. F.**
	Material collection:	**K. F.**
	Analyses:	**K. F.**
	Interpretation:	**K. F.**, T. K., and J. Ď.
	Preparation of manuscript:	**K. F.**
	Corrections of manuscript:	J. Ď. and T. K.
II	Study design:	**K. F.**, T. K., R. B., and J. Ď.
	Measurements:	**K. F.**, R. B., K. M., P. M., V. D., C. L., F. T., and A. M.
	Analyses:	**K. F.**
	Interpretation:	**K. F.**, R. B., T. K., and J. Ď.
	Preparation of manuscript:	**K. F.**
	Corrections of manuscript:	R. B., T. K., and J. Ď.
III	Study design:	**K. F.**, T. K., and P. H.
	Measurements:	P. H.
	Analyses:	**K. F.**
	Interpretation:	**K. F.**, P. H., T. K., and A. P.
	Preparation of manuscript:	**K. F.**
	Corrections of manuscript:	J. Ď., P. H., and T. K

Abbreviations

EDS	energy dispersive X-ray
IAS	L'Institut d'Astrophysique Spatiale
MBA	Main belt asteroid
MGM	Modified Gaussian Model
NEA	near Earth asteroid
NIR	near-infrared
$npFe^0$	nanophase iron
OC	ordinary chondrite
PC	principal component
PCA	principal component analysis
SRIM	stopping and range of ions in matter
TRIM	transport of ions in matter
VIS	visible

List of figures

Fig. 1. An example of landslide uncovering regolith of higher albedo on asteroid (433) Eros. Courtesy NASA/JPL/JHUAPL.

1 Motivation and objectives

During my Master's studies, I focused on the Yarkovsky and YORP effects. These are the non-gravitational effects that significantly alter the semimajor axis and rotation state of small airless planetary bodies by uneven thermal radiation from their surface (see, for example, Rubincam, 2000; Vokrouhlický et al., 2015). The uneven radiation may originate in several ways such as irregularity in shape, or variations of albedo on the surface, which influences the thermal emission. To model these effects correctly, I had to know what the distribution of albedo features usually is. I gained the knowledge that such albedo variations appear especially in the areas of fresh impact craters and steep slopes of asteroids, see Fig. 1. The reason for such changes is mainly the space weathering. I thus decided to study more deeply what this process means and how it affects the planetary bodies in the Solar system.

Space weathering is a complex process, as will become obvious in the following sections of this thesis. I thus decided to start with one of the most common groups of airless planetary bodies – bright silicate-rich bodies. The way space weathering affects them has long been known: darkening, reddening, and loss of spectral contrast in the visible (VIS) and near-infrared (NIR) part of the spectral curves. Nevertheless, what is still unknown is what changes the individual space weathering agents cause.

Many previous studies focused on how one agent influences a given mineral or meteorite, see Sect. 2.3, but this problem also requires a more complex approach. Recently, work by Zhang et al. (2022) focused on a wide range of materials to compare the space weathering changes, which is a step forwards, but they still used only one space weathering agent.

An outstanding work in this respect is the one by Loeffler et al. (2009), who compared olivine spectral changes induced by He^+ ion irradiation to those caused by laser impact. They concluded that spectral changes can be similar even if the weathering mechanisms are different. They found a difference in the timescale that is needed for the two weathering agents to saturate the spectral change, which differs by two orders of magnitude.

Another example is the study by Gillis-Davis et al. (2018), who compared laser- and electron-irradiated samples made of the Murchison meteorite. They found that combination of space weathering agents may lead to greater space weathering changes than using just one of them.

The main aim of this work thus was to evaluate what the differences and similarities in the effect of the two most significant space weathering agents (solar wind and micrometeoroid impacts) are onto spectra of silicate-rich airless planetary bodies. For that, I firstly compared spectra from the areas of lunar swirls to those in the surrounding areas to see if I could distinguish the effect of micrometeoroids. Then I simulated the two space weathering agents during laboratory experiments on very common rock-forming minerals, olivine and pyroxene. And lastly, I focused on laboratory experiments using electron microscopy

to see if there is a difference in the subsurface structure of the minerals dependent on the space weathering agent. My work revealed that there is a difference in the effect of the two agents, as you may see in Sect. 4.

2 Theoretical background

In this section, I will describe the basics of reflectance spectroscopy and how to model reflectance spectra. Then I will focus on the space weathering phenomenon and its special cases. The last part of the introduction will comment on laboratory experiments focused on space weathering simulations.

2.1 Reflectance spectrum

Reflectance spectroscopy is a method of examination of the material by sending photons of various wavelengths and recording photons that were reflected back to the sensor.

As a photon reaches a boundary of two materials with different refractive indices, it may either reflect from the boundary or refract into the second material. If a photon encounters an ion, it interacts with its valence electrons. If the energy of this photon corresponds to the difference in the energy levels of the ion's electron states, it may cause the electron to get into an excited state. As the excited state is not the stable one, the electron eventually falls back into the stable configuration and re-radiates a photon, which is slightly different to the incoming one. Like this the signal into the sensor is decreased and we see an absorption at the wavelength (energy) specific to the material.

The light absorption in the medium is described by Beer's law:

$$I = I_0 \exp(-\gamma z), \quad \gamma = \frac{4\pi\Gamma}{\lambda},$$

where I is the intensity of the observed light, I_0 is the original intensity, γ is the absorption coefficient, Γ is the extinction coefficient (imaginary part of the complex refractive index), z stands for the distance that the light travels through the material, and λ is the wavelength of the light (both equations are valid only for one specific wavelength). Reflection of the light, on the other hand, follows the Fresnel equation, which connects the reflectance R to the real part of the refractive index and to the extinction coefficient. For more information see Bishop et al. (2019) and references therein. A reflectance spectrum then consists of two parts, the continuum and the sudden drops in reflectance (absorption bands).

In planetary spectroscopy, we do not study individual ions, but ions embedded in a crystalline structure. These are usually the transition metal ions, mainly Fe^{2+}, but also an abundance of other ions such as Mg^{2+}. Transition metal ions are characteristic by having their 3d orbital filled with six electrons. The presence of other ions in the crystalline structure causes distractions to the original energetic states in transition ions, which are then characteristic to the reflectance spectrum and cause absorption bands.

This dissertation focuses on two of the most common rock-forming minerals in the Solar system, i.e. olivine and pyroxene. The crystalline structure of both of them is based on silica-oxygen tetrahedrons. Between them, we may most frequently find the above-mentioned ions of Fe and Mg. The ions may consist solely of Fe or solely of Mg ions, but may have various combinations of these ions as well. We then say that the mineral occurs in solid-solution series. For olivine, the iron-rich endmember is called fayalite (Fa), the magnesium-rich endmember is called forsterite (Fo). Pyroxene's endmembers are ferrosilite (Fs, iron-rich) and enstatite (En, magnesium-rich).

2.1.1 Olivine spectra

In olivine, $(Mg, Fe)_2SiO_4$, the metal ions occur in two different crystallographic sites, also known as M(1) and M(2). Visible and NIR spectra of olivine are characteristic by three overlapping absorptions at around 1 μm. The central absorption band originates in the M(2) site, while the two weaker absorptions at both sides of the central band are caused by M(1) site (Burns, 1970). For an example of olivine spectrum, see Fig. 2.

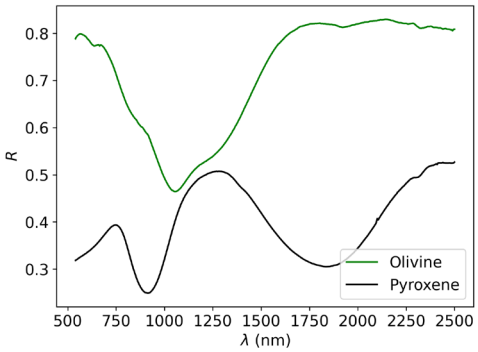

Fig. 2. An example of a spectrum of olivine, Fo_{90}, and pyroxene, En_{67}. Reflectance is denoted by *R*, wavelength by *λ*.

2.1.2 Pyroxene spectra

Spectra of pyroxenes, $(Ca, Mg, Fe)_2(Si, Al)_2O_6$, are characteristic by two major absorption bands at 1 μm and 2 μm, see Fig. 2. These two bands originate in the pyroxene M(2) site (Burns, 1989). Except for M(2), we can also find an M(1) site in pyroxene, but this is more regular and thus produces weaker bands at around 0.97 and 1.2 μm

2.1.3 Changes to the spectral features

Several effects alter the reflectance spectra. For example, the bands shift to longer wavelengths with increasing amounts of Fe in the mineral. These shifts are more pronounced for olivines than for pyroxenes (Clark, 1999). In pyroxenes, we can also see how the crystalline structure influences shapes and positions of the absorption bands, as clinopyroxenes, crystallizing in the monoclinic crystal system, have bands at longer wavelengths than orthopyroxenes, crystallizing in orthorhombic crystal system, see, for example, Fig. 6 in Burns (1989).

The temperature conditions on airless planetary bodies significantly influence the recorded spectrum. As the temperature increases, bands get wider, shift the positions of their minima, and as a consequence, even the band area ratios differ, see, for example, Burns (1989, Fig. 9). The differences do not necessarily occur only between bodies at different distances from the Sun, but also within one body. For example, temperature variations on the dayside and nightside of an asteroid in the Main belt can be 150 K (Bishop et al., 2019). These changes can be accounted for using correction equations to the spectral parameters. The equations are specific for individual minerals, see, for example, Reddy et al. (2015).

Another factor influencing the spectral shape is the size of the regolith particles. The larger the particles in the sample are, the smaller the albedo is, the bluer the spectral slope is, and the deeper the absorption bands are (Reddy et al., 2015). The reason is the bigger surface-to-volume ratio of small grains that causes surface reflections to be more important than internal photon path lengths causing absorptions (Clark, 1999).

The phase angle is another factor influencing spectra. It is defined as an angle between the Sun, the body, and the probe or instrument measuring the spectrum. This viewing geometry influences the spectral slope, albedo, and the position and depth of the absorption bands. All these changes are due to the dependence of the reflectance curves on the observation geometry (Gradie et al., 1980). Sanchez et al. (2012) found that for

the near-Earth asteroids, the spectral slope and depth of absorption bands increase with increasing phase angle. Deepening of the 1-μm band and reddening of spectra with increasing phase angle was also verified on data from the Sloan Digital Sky Survey by Carvano et al. (2014). Yang et al. (2017) found that dark minerals redden with increasing phase angle and bright ones tend to have bluer spectra; the key factor being the multiple scattering effect. Some correction equations have been derived for different types of bodies (Reddy et al., 2015).

2.1.4 Mid-infrared spectra

Part of this dissertation touches on spectral features in the mid-infrared region (MIR), i.e. approximately 3 to 13 μm in this case, other studies go even to longer wavelengths. In this region, the spectroscopy does not proceed in the same regime as in VIS and NIR. The spectral features result from vibrations in the crystalline structure, which are caused by stretching, bending, or rotation of the chemical bonds in the molecules (Bishop et al., 2019; Salisbury et al., 1991). The probed volume is much smaller at longer wavelengths than in the case of the VIS and NIR wavelengths due to rapid increase of the refractive index resulting in strong surface scattering (Brunetto et al., 2020; Lantz et al., 2017).

The main features in the region I probed are the Christiansen feature, associated with the strongest molecular vibration band around 8 μm – 9 μm, and the Reststrahlen bands, originating from Si-O vibrations. For pyroxene, the main Reststrahlen bands may be found between 8.5 μm and 9.5 μm, and in olivine we observe mainly a reflectance plateau between 10.5 μm and 11.5 μm and two minor peaks near 9.5 μm and 10.2 μm. Even MIR spectra depend on many parameters, such as grain size and surrounding conditions, see, for example, Salisbury et al. (1991).

2.1.5 Planetary spectroscopy

Planetary spectroscopy is a very useful technique in Solar system studies. The main advantage is that we can study the surfaces remotely. We do not need to posses and prepare any samples, and this method is non-destructive. Spectroscopy can be used for both crystalline and amorphous materials and as seen above is sensitive to small changes in chemistry and/or mineral structure, which helps to reveal detailed information about the mineralogy of the studied bodies (Adams, 1974; Clark, 1999; McCord et al., 1970; McCord et al., 1981). We usually use VIS and NIR spectral regions, which means wavelengths from 400 nm to 700 nm and from 700 nm to 3000 nm, respectively.

However, remotely measured spectra usually suffer from loss of spectral details due to several factors, chief among them being lower resolution of spectrometers on board of interplanetary spacecrafts. Further, in case we measure the spectra from the Earth, the atmosphere debases part of the information because of the absorptions caused mainly by water and hydroxyl (around 3000 nm), but also by atmospheric ozone (350 nm), oxygen (760 nm), and carbon dioxide (2000 nm and 2060 nm). For more details, see for example, Clark (1999).

2.1.6 Spectral fits – Modified Gaussian Model

This thesis is based on comparison of different spectra and also on comparison of spectral parameters. To obtain the spectral parameters, a model of the spectrum needs to be introduced. One of the most acknowledged tools, of the last two decades (Clénet et al., 2011), for fitting re-

mote mineral reflectance spectra is the Modified Gaussian Model (MGM) by Sunshine et al. (1999). First introduced in year 1990 (Sunshine et al., 1990), MGM significantly improved estimates of the basic spectral characteristics such as the spectral slope, depth of mineral absorption bands, their position, etc. The spectrum is fitted in the space of natural logarithm of reflectance ln(R) and energy x. This combination allows for a simple mathematical summation of the spectral continuum C and absorption bands, based on the equation:

$$\begin{aligned} \ln R(x_k) &= \sum_{i=1}^{l} m(x_k)_i + C \\ &= \sum_{i=1}^{l} m(x_k)_i + ax_k + b, \end{aligned}$$

where a, b are the slope and intercept of the continuum, index k = 1,..., n, n is the number of individual wavelengths of measured spectra, and i = 1,..., l, l being the number of modified Gaussian distributions/mineral absorption bands in the spectrum. The modified Gaussian distribution m has the following form:

$$m(x_k)_i = s_i \exp\left(\frac{-(x_k^{-1} - \mu_i^{-1})^2}{2\sigma_i^2}\right),$$

where s stands for the strength or amplitude of the distribution, μ is its centre (mean), and σ its standard deviation. The difference between the Gaussian (also called normal) and the modified Gaussian distributions is in the exponent $^{-1}$ in the $-(x_k^{-1} - \mu_i^{-1})^2$ parenthesis. The general Gaussian (normal) distribution has this equation:

$$G(\mu, \sigma^2) = \frac{1}{\sqrt{2\pi\sigma}} \exp\left(\frac{-(x-\mu)^2}{2\sigma^2}\right). \quad (1)$$

The modification coefficient for the modified Gaussian curve was derived empirically, using a single-crystal orthopyroxene spectrum, and allows for the asymmetry of the slopes of distribution wings (for more details see Sunshine et al., 1990). An example of olivine spectrum fitted using MGM is shown in Fig. 3.

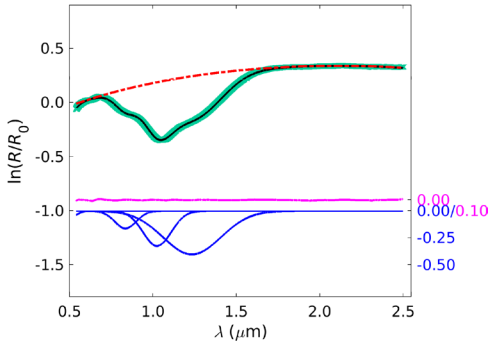

Fig. 3. An example of fit of olivine spectrum using MGM. The green line represents the measured spectrum. The red dashed line is the continuum curve, the blue lines are individual modified Gaussian curves that summed together with the continuum result in the black line representing an overall fit. The purple line marks the error of the fit, R is the reflectance, R_0 reflectance of the fresh spectrum at 750 nm, and λ is the wavelength. Note that the y axis is in natural logarithm.

2.2 Space weathering

As emphasized in previous sections, several effects (such as the temperature of the surface, viewing geometry, and grain size) significantly change the overall appearance of the spectra. Errors in mineralogy interpretation do not occur only due to these effects though. Space weathering is another important factor influencing the physical and chemical properties of airless planetary surfaces (Hapke, 2001; Pieters et al., 2016). Space weathering does not refer to only one process but encompasses several processes, the prime of which are the irradiation by solar wind ions and impacts of micrometeoroids. Several other processes also influence the space weathering state of airless planetary bodies, such as galactic radiation or contamination by the material of impactors, but these do not have as significant impact for the bodies I refer to in this thesis. As a result of space weathering, the chemical and physical state of topmost surface layers, approx. hundreds of nm, is altered

(Hapke, 1965; Hapke, 2001; Pieters et al., 2000; Pieters et al., 2016; Wehner et al., 1963).

In this thesis, I deal with the silicate-rich bodies. It was found that as a result of space weathering, VIS-NIR spectra of these bodies darken (albedo decreases), darkening is more intense towards the shorter wavelengths (resulting in spectral slope reddening), and the characteristic mineral absorption bands fade away, see, for example, Hapke (2001).

2.2.1 Lunar space weathering

The studies of space weathering originate in work of Gold (1955), who noticed that the craters on the Moon degrade with time. The main boom of interest in space weathering started after the Apollo missions, which brought lunar soils and boulders back to the Earth. At that point, it started to be evident that the spectrum of the space weathered soil does not match the spectrum of the preserved interior of the boulder crushed to the same particle size, see, for example, Hapke et al. (1970).

Originally the spectral changes have been incorrectly prescribed to the presence of impact glasses, but Cassidy et al. (1975) showed, that space weathering is caused by the creation of small particles of metallic iron, so-called nanophase iron particles ($npFe^0$). The $npFe^0$ particles have (on the Moon) typical sizes of several nm (≈ 3 nm) and are found in thin surface layers (≈ 100 nm layer of the 60 μm grain) of the topmost regolith grains (Pieters et al., 2000; Pieters et al., 2016). The main changes these particles produce in the spectra are reddening with a small contribution of darkening (Keller et al., 1998; Noble et al., 2007).

Nanophase iron may grow to larger sizes. Upon impacts, individual particles merge into larger structures held together by impact glasses, also known as agglutinates, which consequently cause darkening of the spectra (Keller et al., 1998; Noble et al., 2007).

Both types of these particles are opaque and thus disable the repeated reflections in the material, which is the main reason for the darkening (Chapman, 2004). The main reasons for their creation are melting caused by microimpacts and solar wind sputtering. The melting creates vapours of the impacted and target material, during which light gasses, such as oxygen or magnesium, escape the surface, which is then depleted in them. The unbound metallic iron condensates and settles back on the surface of the grain (Cassidy et al., 1975; Hapke, 2001). During the sputtering event, iron is unbound from the silicate and settles on the surrounding grains. Small $npFe^0$ particles are created mainly by sputtering, whereas large ones are created by melting (Blewett et al., 2011; Noble et al., 2007).

Lunar swirls

A natural laboratory for evaluation of space weathering may be one of the lunar swirls. A lunar swirl is a curvilinear bright patch on the lunar surface, whose shape is not connected to the local topography. Lunar swirls may be found all over the lunar surface (Hood et al., 1989). When localized in a lunar mare, the swirl is usually more complex in shape and the albedo contrast to the background material is stronger than in highlands, where the swirls tend to be simpler and less visible (Blewett et al., 2011). All lunar swirls are associated with increased magnetic field, so-called magnetic anomaly. On the other hand, it is not true that all magnetic anomalies would be associated with lunar swirls. Hood et al. (1989) showed that an average magnetic field in the Apollo landing site is approximately 327 nT, and in lunar swirl areas, it can be greater than 1000 nT.

A typical example of lunar swirl is the Reiner Gamma in Oceanus Procellarum or the Mare

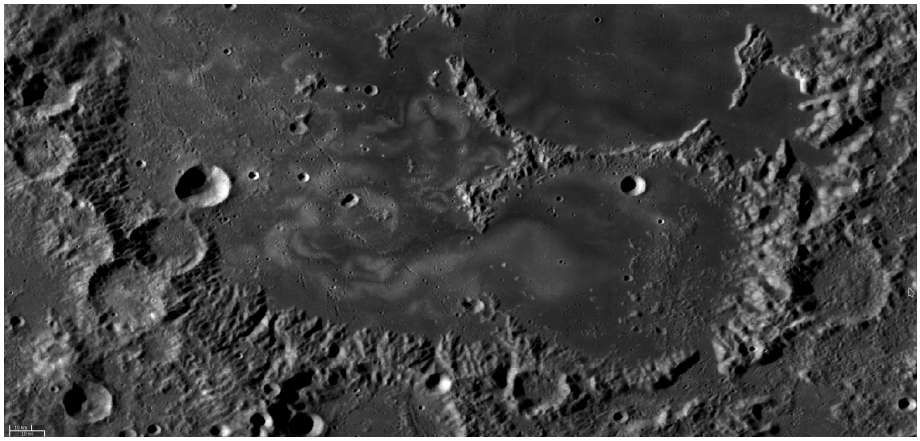

Fig. 4. Mare Ingenii swirl. Exported from Lunar QuickMap, https://quickmap.lroc.asu.edu/.

Ingenii swirl (see Fig. 4). Both show large spectral contrast and a complex shape. An example of the highland swirl is, e.g., the Gerasimovich anomaly, which is also the area of the strongest magnetic field on the Moon.

Due to the higher albedo, the lunar swirls were thought to be fresh, or at least similar to the fresh material (Blewett et al., 2011), but several recent studies showed that the swirl material may be distinct from the fresh material we find in craters (Pieters et al., 2016). Except for the higher albedo, the lunar swirls have slightly lower FeO abundance than the rest of the lunar surface (Blewett et al., 2011).

Another unresolved question is the origin of the lunar swirls. Soon after their discovery, Schultz et al. (1980) suggested that the swirls originated in the cometary impact event. Other theories commented on meteorite impacts causing high enough temperatures for creation of magnetic fields. Nevertheless, this theory is inconsistent with the fact that Glotch et al. (2015) did not observe any changes of the cm-scale roughness or temperature of the swirl areas that would support such events in the Lunar Reconnaissance Orbiter Diviner Lunar Radiometer data. On the other hand, a newer study of Bhatt et al. (2021) comments on the differences in the regolith microstructure in the Reiner Gamma swirl compared to the surroundings. Some of the swirls are placed in antipodes to the big impact basins on the Moon (Hood et al., 1989). This led to a theory that the material ejected during the basin's creation circulated around the Moon and collided in the antipode, creating the swirl. Not all swirls are found in the antipodes though.

The main factor influencing the state of lunar surface in the area of lunar swirl is the presence of the magnetic field. This field protects the surface from the majority of incoming charged particles (such as the solar wind ions). The ions are deflected and move along the magnetic field lines, by which they are concentrated into narrow areas of so-called dark lanes (Kramer et al., 2011). The theory of surface preservation from incoming ions is called the Magnetic field stand-off theory (Hood et al., 1980; Hood et al., 1989).

The magnetic field stand-off does not influence the micrometeoroids, as they are not charged. The lunar swirls are believed to be ≈ 3.9 Gyr old (Blewett et al., 2011). Micrometeoroids would thus have a sufficiently long time to weather their surface. Another mechanism causing the bright nature of the swirls has thus been proposed. Neugebauer et al. (1972) was the first one who associated the magnetic field on the Moon with the creation of electric fields. An electric field is created by separation of electrons

and protons in the presence of a magnetic field. This is how the electric potential is generated. Fine dust is then lifted by the terminator crossing and transported great distances. According to Stubbs et al. (2006), 0.1 to 1 μm particles can be transported up to several kilometres on the surface of the Moon and bright highland material may get transported into the swirls.

2.2.2 Asteroidal space weathering

Asteroids may be divided for example based on their position in the Solar system (into near Earth asteroids, NEAs, and Main belt asteroids, MBAs), based on their size, or based on their mineralogy. As this thesis focuses on the spectral features that are strongly connected to the mineralogy, let us focus on this aspect. Generally, there are two types of asteroids: bright and dark ones. Based on the classification of DeMeo et al. (2009), the bright asteroids are those of Q-, S-, A-, R-, and V-type and these are the aim of my work[1].

One of the prime motivations to study asteroidal space weathering is to understand the evolution of asteroidal families. The dynamical age of a family correlates with reddening of the spectra of its members, because we expect that the parent body of the family was fresh in its volume, and during the catastrophic collision, its inner parts became the surfaces of individual members of the family. The space weathering evolution state may thus be useful for identification of members of one family among other families, estimates of their evolution, etc.

Asteroidal space weathering studies originate in the disagreement between spectra of ordinary chondrite (OC) meteorites and their expected parent bodies, S-type asteroids (Brunetto et al., 2015). It was soon found out that if we apply changes consistent with space weathering to the OC spectra, we obtain remarkable similarity with S-type asteroidal spectra. It was also found that the Q-type asteroids are fresher analogues of S-type asteroids, see for example, Binzel et al. (2004) and Chapman (2004).

Several missions have studied bright asteroids in greater detail. The prime among them in the extent of the mission is the Hayabusa sample-return mission organized by the Japan Aerospace Exploration Agency to asteroid (25143) Itokawa. This mission delivered material from the asteroid back to the Earth for a more detailed examination. Based on it, we know that even at asteroids, the spectral changes may originate from the nanoparticles, in the case of Itokawa mainly of FeS and MgS, immersed in amorphous rims created by vapour deposition. Based on Brunetto et al. (2015), the observed particles do not contain agglutinates, as was seen on the Moon, which points to the lack of high-velocity impacts on the body. Also, based on the pictures of the surface, we can see that interplanetary dust particles may cause albedo variations at larger boulders. Generally, Itokawa shows considerable variations of brightness and colour corresponding to the presence of steep slopes and elevated areas (Hiroi et al., 2006). All of this is consistent with expectations about the space weathering behaviour.

Other missions visited, for example, asteroids (4) Vesta or (433) Eros and based on the images obtained we may also evaluate their space weathering trends. For example, Eros shows great variations of albedo, especially in the steep slopes, but small variations of spectral slope (Chapman, 2004). Vesta shows only low levels of space weathering and its changes may, according to Pieters et al. (2016), be associated

1 In recent years, space weathering studies also focused on dark asteroids (such as C-types) to support ongoing planetary missions to asteroids (101955) Bennu and (162173) Ryugu. These materials weather in a different way. For example, they experience spectral blueing instead of reddening, see, e.g., Brunetto et al. (2018) and Brunetto et al. (2020).

mainly to the mixing with impactor material. The space weathering does not proceed in the lunar style there.

2.2.3 Typical space weathering timescales

The speed at which planetary surfaces weather is dependent on the environment they inhabit and also on their properties (Hapke, 2001; Pieters et al., 2000; Pieters et al., 2016). Firstly, the position of the body with reference to the Sun is important, as the flux of the solar wind particles changes with the square of the distance from the Sun. The conditions are thus different for Near-Earth asteroids and for asteroids in the Main belt. Also the speed of micrometeoroids relative to the body is position-variable. It is expected that on Mercury, the amount of impact-induced melt is an order of magnitude larger than on the Moon (Bishop et al., 2019). Dependent on the position in the Solar system, other processes interconnected to space weathering become important, such as thermal cycling, which cracks the boulders, or sublimation on bodies rich in ices. For an overview of space-weathering processes, see Fig. 5.

Additionally, there is a strong correlation with surface mineralogy, as the higher abundance of silicate minerals implies higher iron content and thus more material for creation of $npFe^0$ particles. Another factor is the surface texture, as it was shown that space weathering is dominant mainly in porous materials (Hapke, 2001), and spectral properties are influenced mainly by < 45 μm particles on the Moon.

Moreover, the time the surface is subject to the space environment is crucial for its weathering stage. Solar wind saturates the weathering state after $\approx 10^5$ yr at 1 au, but weathering by micrometeorites is ≈ 1000-times slower (Hapke, 1977; Noguchi et al., 2011; Yamada et al., 1999). Laboratory experiments showed that olivines are more easily weathered than pyroxenes (Yamada et al., 1999), which was later supported also by atomic-scale computational study of Quadery et al. (2015). On the other hand, space weathered surfaces are rejuvenated by several effects, see Section 2.2.4.

2.2.4 Rejuvenation processes

Even though asteroids are older than the typical weathering timescales, they do not generally look completely weathered. A group of processes rejuvenate their surfaces so they appear fresh.

The collisional lifetime of a 1-km body is > 10 Myr, which is few orders of magnitude larger time than the typical space-weathering timescale, disruption thus is not a source of rejuvenation of the surface. Smaller, non-catastrophic, impacts on the other hand, may overturn the topmost regolith layers of asteroids and uncover the fresh, underlying layers. Other rejuvenation processes are, for example, planetary encounters, spin-up by the YORP effect, or in the case of NEAs the thermal fatigue fragmentation (Brunetto et al., 2015).

2.3 Space weathering laboratory experiments

Because of the sparsity of real space samples, laboratory irradiation experiments on terrestrial samples or meteorites are the most widespread mean of analyses aiming for a better understanding of the effects of space weathering. The two main space weathering agents are usually simulated by different types of experiments. Solar wind ions are represented by accelerated ions of light elements (see, for example, Lantz et al., 2017; Loeffler et al., 2009; Vernazza et al., 2013), while micrometeoroid impacts are simulated mostly by laser irradiation (see, for example, Sasaki et al., 2002; Yamada et al., 1999; Fazio et al., 2018). The experiments have one aspect

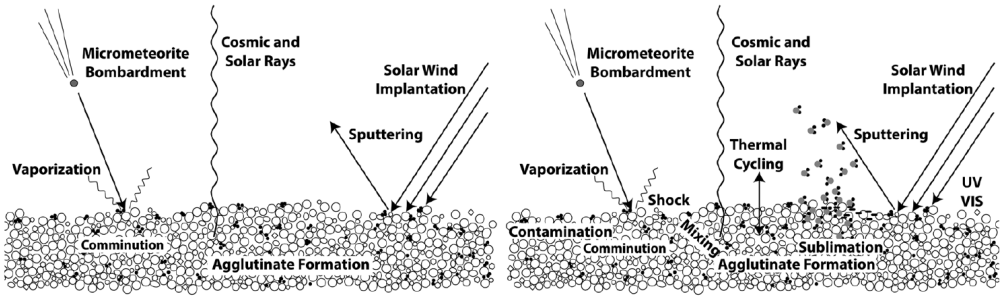

Fig. 5. An overview of space-weathering related processes. (left) Situation on the Moon, i.e. at 1 au. (right) Situation elsewhere in the Solar system. Depending on the position, contribution of the mentioned processes differ. Overtaken from Pieters et al., *Journal of Geophysical Research: Planets*, published online 21 October 2016, page 1866, see Pieters et al. (2016).

in common. All are done under vacuum conditions. Even though the previous studies did not simulate the space environment perfectly, there are increasing efforts to improve the conditions of the experiments, mainly in terms of surface textures, pressures, temperatures, and used materials, to get nearer to the reality (Brunetto et al., 2015).

2.3.1 Solar wind component

Ion irradiation experiments differ by the type of the ion used. Most of the studies up to date focused on the most common solar wind ions, i.e. hydrogen, H, and helium, He, that make up to 99 % of the total flux (see, for example, Brunetto et al., 2005; Brucato et al., 2004). Some works also used heavier ions, to simulate other components of the solar wind (see, for example, Kaňuchová et al., 2010; Fulvio et al., 2012).

Another aspect that differs is the energy of ions. Generally higher energies than what are the typical energies of the regular solar wind are used. Typically, the most common H^+ ion has an energy of about 1 keV, and He^+ ion energy of approximately 4 keV. Nevertheless, many works used even more than 10 times greater energies, see, for example, Lantz et al. (2017). These studies thus simulated particles from the solar flares, which are not as common as the regular, calm, solar wind but may also have a significant impact (Brunetto et al., 2015).

Most previous work on silicate-rich materials verified the general space weathering trends, i.e. spectral darkening, reddening, and decrease of spectral contrast (see, for example, very early work by Hapke et al. (1970) on lunar samples irradiation). Many studies focused on individual bodies, such as Brunetto et al. (2005) who managed to estimate the surface exposure age of asteroid (832) Karin based on their irradiations of olivine and pyroxene samples. By correlating observations of irradiated eucrite meteorites with the observed slopes of V-type asteroids, Fulvio et al. (2012) managed to better explain connection between asteroid Vesta, V-type asteroids and HED meteorites.

2.3.2 Micrometeoroid impacts component

The effect of micrometeoroid impacts would be convenient to study through irradiations by micrometer-sized dust particles. At the moment there are not many facilities that would be capable of producing high enough fluences of such particles to significantly weather the sample. Nevertheless one such rare experiment has been conducted by Fiege et al. (2019). More often the way to simulate the impacts is through irradiation by laser pulses.

The most widely used laser is yttrium-aluminium garnet doped by neodymium, with the typical wavelength of 1064 nm (see, for example, Corley et al., 2017; Sasaki et al., 2002). Usual pulse duration is between 6 ns and 8 ns, as this timescale is comparable to the duration of 1 μm–10 μm dust impacts (Yamada et al., 1999; Sasaki et al., 2002). Also as shown by Fulvio et al. (2021) the created impact craters resemble the naturally occurring craters. Fazio et al. (2018) were the first who conducted a new type of experiments using femtosecond laser pulses. Based on their work, femtosecond pulses represent the reality of the micrometeoroid impact better as for high enough irradiance the created shock wave propagating through the sample resembles the actual impact, while nanosecond pulses just heat and melt the surface. Even in the case of femtosecond pulses, the morphology of created craters resembles observations from the lunar samples (see, e.g. Noble et al., 2015) and particles from asteroid Itokawa (see, for example, Harries et al., 2016).

Also laser irradiation experiments aim to explain observations from the Solar system. Based on their laser irradiations of olivine, Brunetto et al. (2007) estimated that the age of surface of A-type asteroid (1951) Lick is very high, $\approx 10^7$ yr. Sasaki et al. (2002) noted that crystal samples of olivine do not show traces of structural changes, while in powder pellets, nanophase iron particles are abundant. From that they concluded that small asteroids, which do not possess regolith layers, will be very hardly weathered. This correlates with observations of Q-type asteroids, which are mostly small and look fresher than larger S-type asteroids of similar composition (Binzel et al., 2004).

2.3.3 Subsurface changes

Very early after the community began to work on irradiation experiments, researchers wondered what the origin of spectral changes is, i.e. what is the subsurface cause of the spectral alteration. Sasaki et al. (2001) studied olivine irradiated by laser and found that it contains amorphous rims rich in nanophase iron particles, similar to those observed in the lunar samples by Keller et al. (1993).

Many studies on terrestrial samples focused on the dimensions of either the amorphous rims or nanoparticles, see, for example, Fazio et al., 2018; Sasaki et al., 2002; Weber et al., 2020. Many worked with the samples from airless bodies, such as the Moon (Kling et al., 2021) or asteroid Itokawa (Noguchi et al., 2014b; Noguchi et al., 2014a). Based on these studies, we may conclude that weathering-induced nanoparticles on the Moon and asteroids do not have the same characteristics, e.g. we see larger particles on the Moon than on Itokawa. Except for the observed $npFe^0$ particles, space weathered rims show abundant vesicles (see, for instance Dobrică et al., 2016; Matsumoto et al., 2015).

Subsurface changes thus proceed differently for different airless planetary bodies. To see the reason for this, Weber et al. (2020) studied laser-weathered olivine and pyroxene samples. They found that the subsurface structure of these two materials differs both in the thickness and in the nanostratigraphy but the reflectance spectra are not dependent on the source of changes.

Our knowledge of space weathering changes still improves, for instance in a new study by Cymes et al. (2022), electron microscopy images revealed that some of the soils from the Apollo 17 mission contain $npFe^0$ particles that contain vesicles. These vesicles are expected to be created by solar wind, as in some cases the vesicles are larger at the near-surface side of the particle and are filled with He.

3 Methods

Here, I describe what were the main methods I used when working on this dissertation. I will start by describing the experimental setups for laboratory simulations of space weathering. Then I will focus on how I obtained the reflectance spectra for the various analyses. The next part will describe observations using electron microscopy. Then I will briefly introduce one of the most useful methods I used for finding the spectral trends in the data, i.e. the principal component analysis (PCA). The last part will briefly comment on some of the statistical methods used. For a more detailed description of the apparatuses and the data sets, please see the attached Papers I, II, and III.

3.1 Laboratory simulations of space weathering

For all the irradiations, I used the same material. This gives additional value to the results, as I was then able to compare the effect of the two space weathering agents without the need of further discussions about possible influence of varying mineralogy, which is the great contribution of this work to the field, as other studies did not focus on such comparison earlier.

Irradiations have been conducted using two materials: olivine and pyroxene, which are commonly found on silicate-rich airless planetary bodies, see Chrbolková et al. (2021), i.e. Paper II. The materials were ground and dry-sieved to obtain only grains smaller than 106 μm, which I consequently pressed into pellets with KBr base, as was done previously e.g. in work of Lantz et al. (2017). All the irradiation experiments were conducted in vacuum conditions to match the real situation.

3.1.1 Effect of solar wind

I simulated the effect of solar wind by irradiations with three different types of ions: the most common solar wind ion H^+, the second most common He^+, and an ion representing heavier elements Ar^+. I used low energies (5 keV H^+, 20 keV He^+, and 40 keV Ar^+) to get close to the real standard solar wind situation.

Different fluences (ranging from 10^{14} ions/cm^2 to 10^{18} ions/cm^2) simulated different levels of space weathering. Simulations covered timescales from fractions of a year to several hundreds of years for lighter ions and several hundreds of thousands of years for Ar^+.

The irradiations using H^+ ions were done at the University of Helsinki Accelerator laboratory and led by Dr. Kenichiro Mizohata. The whole set of pellets was placed into a vacuum chamber onto a rotating carousel, see Fig. 6 (a). Each pellet simulated one space weathering state and one pellet was left un-irradiated as a comparison sample. The samples were stabilized before extracting from the vacuum chamber as in Kohout et al. (2014).

The irradiations by He^+ and Ar^+ ions proceeded at L'Institut d'Astrophysique Spatiale (IAS-CSNSM), Orsay, with the help of Dr. Cateline Lantz and Dr. Rosario Brunetto. The pellets were placed onto a sample holder, see Fig. 6 (b), and after irradiation immediately measured for spectral changes. After the spectral measurement, the irradiations with greater doses proceeded onto the same pellet.

3.1.2 Effect of micrometeoroid impacts

Based on work by Fazio et al. (2018), I decided to simulate the effect of micrometeoroid impacts using individual femtosecond laser pulses. This is a rather novel approach as most previously published experiments used nanosecond pulses. We

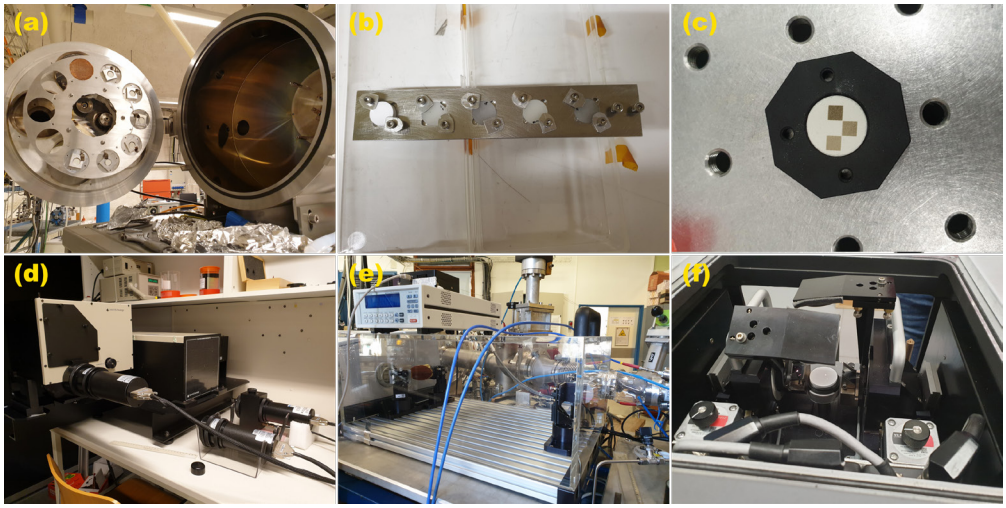

Fig. 6. Photographs of the experimental setup. (a) Carousel holder for multiple pellets irradiated by H^+ ions at the Accelerator laboratory of the University of Helsinki. (b) Sample holder for multiple pellets and the Spectralon standard (the left-most position) for He^+ and Ar^+ irradiations at IAS. (c) Sample holder for one pellet for laser irradiation at the Department of Chemical Physics and Optics, Charles University. (d) Spectrometer at the University of Helsinki. Integrating sphere is attached from the bottom of the spectrometer. (e) Part of the path of spectral signal at the IAS. Samples are in the vacuum chamber to the right, spectrometers are to the left. (f) Variable angle reflection accessory for spectral measurements at Charles University.

built, with Prof. Petr Malý and Dr. František Trojánek, a new experimental setup at the Department of Chemical Physics and Optics, Charles University.

The laser in my experiment shot pulses into a square grid in which the spatial distance between individual laser-induced craters differed, see Fig. 7 for an example. The denser the craters were, the higher weathering stage the material experienced. In this way, I simulated timescales ranging from several hundreds to several thousands of years. In the experiment, the laser never shot into the exactly same place twice, as is seen in some other works (e.g. Brunetto et al., 2005), but in the denser configurations, the craters could overlap. The experiment was designed so that each sample contained four different squares, three containing an increasing weathering stage and one left un-irradiated as a reference. Each sample had its own sample holder made from Teflon, see Fig. 6 (c). Before extracting from the vacuum chamber, the samples were surface passivated, as in H^+ irradiation case, and taken out of the sample holders.

3.2 Reflectance spectroscopy

In this work, I focused on two main wavelength ranges: VIS and NIR. Paper I uses spectra of the lunar surface measured in the VIS-NIR wavelengths. My laboratory experiments (Paper II) then describe changes in the VIS, NIR, and also briefly in the MIR part of the spectra. In Paper III, I connected the observed changes found with electron microscopy to the VIS-NIR changes.

3.2.1 Lunar study

Reflectance spectra of the Moon come from the Moon Mineralogy Mapper (M^3) instrument, which was part of the Chandrayaan-1 probe orbiting the Moon from November 2008 to December 2009 (Green et al., 2011). When mapping the lunar surface, M^3 used two modes: target (with maximum possible spectral and spatial

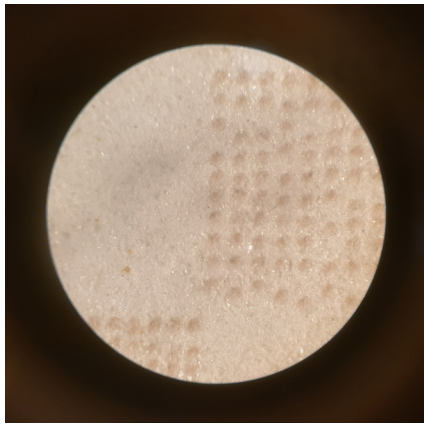

Fig. 7. An example of an olivine pellet surface after laser irradiation. The right part shows part of a square with craters approx. 300 µm apart, in the bottom, the craters are approx. 250 µm apart.

resolution, i.e. 260 spectral channels and 70 m per pixel spatial sampling) and global (with reduced spectral and spatial resolution). The global mode measurements covered more than 95 % of the lunar surface in 1386 downlinked files, while the target mode covered only a small portion of the surface (156 downlinked files). I thus used the global mode as with the target mode I would not be able to cover all the desired areas.

The spectral measurements of Level 2 reflectance data that I used span from 541 nm to 2976 nm covered in 83 channels. These spectra were thermally and photometrically corrected (Besse et al., 2013; Clark et al., 2011). All of them were uploaded to the Planetary Data System's Geosciences Node, from where I downloaded them.

I selected the spectra from the regions of interest, i.e. the areas of the fresh craters, containing pristine material, areas of lunar swirls, containing material weathered presumably mainly by micrometeoroid impacts, and mature areas influenced by all the space weathering agents, using the ENVI software. These spectra were then subject to spectral fitting using the Modified Gaussian Model, and comparison using the histogram plots and the principal component analysis.

3.2.2 Asteroidal study

To compare my results with measurements of real asteroidal spectra, I used data from DeMeo et al. (2009), which they used to construct the new asteroid taxonomy. The original dataset contains 371 asteroidal spectra. The part from 400 nm to 900 nm comes from the Small Main Belt Asteroid Spectroscopic Survey, the part from 800 nm to 2500 nm was obtained using the low- to medium-resolution NIR spectrograph and imager SpeX at Mauna Kea, Hawaii. For the purposes of my work, only spectra of silicate-rich asteroids were extracted, i.e. S-, Q-, V-, and A-type asteroids. The spectra were then subject to PCA.

3.2.3 Laboratory study

Paper II is based on spectral analysis of the irradiated pellets, see Sect. 3.1. As is mentioned in the paper, reflectance spectroscopy has been conducted in three different laboratories, mainly because of the complexity of the task. The major point is that all the measurements covered a very similar wavelength range (from 540 nm to 2500 nm) and thanks to the observational conditions, and the fact that I mainly searched for relative trends, were comparable.

H^+-irradiated pellets

I measured the spectra resulting from the H^+ irradiation using the Gooch and Housego OL-750 automated spectroradiometric measurement system located at the Department of Physics, University of Helsinki. The spectra were captured relative to golden and PTFE standards, with incidence angle of the spectral beam 10° relative to the normal to the surface. The measurements were conducted under ambient pressure and room temperature, see Fig. 6 (d).

He^+- and Ar^+-irradiated pellets

Spectra of pellets irradiated by He^+ and Ar^+ were measured by Maya2000 Pro, OceanOptics, and Tensor 37, Bruker, using the Spectralon standard at IAS. Compared to the H^+ irradiations, these spectra were measured in situ in the same vacuum chamber where the irradiations proceeded, see Fig. 6 (e). Incidence and collection angles varied for the VIS and NIR sections of the spectra, the phase angles were therefore 20° and 15° for the VIS and NIR range respectively.

Laser-irradiated pellets

After extracting the laser-irradiated pellets from the vacuum chamber, I measured their spectra using Vertex 80v, Bruker, with A513/Q variable angle reflection accessory and using the Spectralon standard, see Fig. 6 (f). The spectrometer worked in mild vacuum conditions. The incidence angle was 0° and the collection angle was 30°.

In all cases, the spot from which the spectrum has been captured was significantly larger than the inhomogeneities of the sample and reflected the typical sizes of alteration in the sample.

3.3 Electron microscopy

Samples irradiated by ions and laser were then subject to electron microscopy done mainly by Dr. Patricie Halodová at the Science Centre Řež, the Czech Republic. The aim of the electron microscopy was to obtain information on the surficial and subsurface changes in the samples, their dependency on the space weathering agent/irradiation type, and their connection to the spectral changes.

Scanning electron microscopy aimed mainly at the changes in the surface structure and chemical conditions on the surface. I based the research mainly on images using the backscattered secondary electrons and on energy-dispersive X-ray analysis (EDS) of the elemental abundances. Transmission electron microscopy, on the other hand, aimed at the changes in the top-most 1 μm of the samples. My conclusions on subsurface alterations were then based mainly on bright-field transmission images and also on the EDS.

3.4 Principal component analysis

PCA is, at least in my work, used as a dimensionality reduction technique, which enables separating valuable information from noise through linear transformations in multidimensional space (Connolly et al., 2014).

In general, the input into PCA is an *n*-dimensional cloud of points, where *n* represents number of measured parameters, in this work the number of wavelengths at which the spectrum has been captured, and individual cloud points represent different measurements. These values are written in the form of $m \times n$ matrix (m being the number of points), which is then, using the Singular value decomposition algorithm, converted into a set of three matrices containing eigenvectors and eigenvalues of the covariance matrix of the data. Using these, we can then calculate the transformation into the new coordinate system. In this new system, the first coordinate (principal component, PC) corresponds to the direction, in which the original data had the greatest variance. Orthogonal to this direction, in the direction of the greatest variance that was left in the data after the first PC was subtracted, lies the second PC, etc. until we reach the *n*-th direction.

Obviously the first few components explain a majority of the variance in the data and the rest of them represent the random noise. We can then select only the relevant PCs and search for the trends in an easier-readable data.

There are a few major points one should have in mind when using PCA:

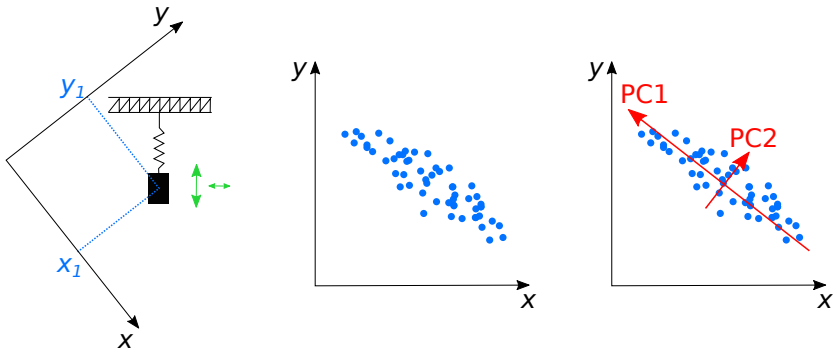

Fig. 8. An illustration of the basic principle of PCA. (left) A weight on a spring moves in up-down direction with a slight left-right movement. We measure the coordinates of the weight in given time intervals. The coordinate system is set as in the figure. (center) The resulting measured positions. (right) PCA finds the first coordinate, which corresponds to the direction of the greatest variance in the data, i.e. the direction of the up-down movement of the weight. The second component is perpendicular to it and refers to the right-left movement of the weight.

- PCA is a mathematical apparatus that does not necessarily transform the dataset into physically realistic variables. The interpretation of the results may thus be abstract. Even though in some cases, it may be possible to do so, see an example in Fig. 8.

- PCA is very sensitive to pre-processing of the dataset, for example to whether we normalized the variance in the data or whether we subtracted the mean.

In my thesis, PCA was mainly used on sets of spectral curves. For example, in Paper I, I used m = 1324 spectra of the Reiner Gamma swirl with n = 83 measured values of reflectance in each spectrum. The PCA then showed that only the first few PCs explain the shape of the spectra, while the rest is noise. Using plots of, mainly, the first two PCs, I could then see that the spectra from the fresh craters have a slightly different shape than the spectra from the Reiner Gamma swirl and are different from the spectra of the mature soil in the vicinity of the swirl.

Similarly, I then used PCA in Paper II. Based on the PC space calculated on my spectral measurements, I evaluated the space weathering trend in the Q- and S-type asteroid population and did further conclusions.

3.5 Statistical methods

Statistical methods are widely used in astronomy and planetary science. By using huge statistical sets of low or average quality data, we are generally able to make conclusions on the same level of reliability as those made from a smaller amount of high-quality data.

3.5.1 Histograms

A histogram shows a frequency distribution of a statistical dataset (de Smith, 2018). Based on how rough we want the histogram to be, we use a variable number of bins, into which we group the values. The selection of the number of bins may influence the interpretation of the results and is thus very important. For my work, I used the Sturges' binning algorithm (Sturges, 1926). This algorithm assumes that the data are normally distributed and requires big datasets, with more than 30 samples. The algorithm uses $\log_2(N) + 1$ bins, where N is the number of measurements of the given variable. In case the number is not an integer, it rounds the result up.

To enable comparison of different histo-

grams, their normalisation is needed. Therefore, this work used the Probability density function normalisation. This normalisation causes the total sum of all bins' areas to be less than or equal to 1.

Histogram plots were used mainly in Paper I, where I compared distributions of various spectral parameters with respect to the position inside or outside the swirl.

3.5.2 Two-sample t-test

Hypothesis testing is an inevitable part of statistical analysis. In this thesis (Paper I), I tested whether two sets of spectral parameters have the same means or not. As a result, I could say if there is a difference in the parameters of the individual swirls and their surrounding material.

For testing, I used the Two-sample t-test (de Smith, 2018). This test assumes that the two datasets come from a normal distribution, as in Eq. 1, with the same variance. The null hypothesis is that also the means of the datasets are the same. The zero hypothesis is then rejected or not based on comparison of a probability value *P*, resulting from the test, with the given threshold value, which is usually set to 5 %. If the null hypothesis is rejected, then the two datasets are different, and I could say that the two sets of spectral parameters show a trend.

4 Overview of research output

In this section, I am going to point out the most significant results of this thesis, which were published and are attached at the end of this text. In Paper I, I focused on evaluating spectral evolution in the areas of lunar swirls. Paper II relates to experimental work, based on which I compared the two major space weathering agents and their influence on the silicate-rich bodies' spectra. And in Paper III, I evaluated what the subsurface structure of the irradiated material is and what consequences it has for the spectral evolution.

4.1 Paper I – Effect of micrometeoroids in lunar swirls

In the beginning of my work, I searched for some natural laboratory, where the two most significant space weathering agents would be separated. An ideal candidate were the areas of lunar swirls. Based on the solar wind stand-off theory, the surface of the Moon in the area of swirl is shielded by the magnetic field from the majority of incoming solar wind ions. As a result, the area is influenced mainly by the micrometeoroid impacts, see Sect. 2.2.1 for more details. I could thus see what the natural spectra influenced by micrometeoroids look like and compare them to the spectra of the areas influenced by both the space weathering agents and to the areas of the pristine soil found in the larger impact craters.

Selecting seven different swirls from distinct locations around the Moon, I found two main dichotomies in the spectral evolution:

1. The mare/highland dichotomy in the albedo and 1 μm band depth behaviour. This dichotomy may potentially be prescribed to the different FeO content of the two types of terrain, which is the first hint to the observations in Paper II.

2. The near-/far-side dichotomy in the spectral slope behaviour, which probably results from the fact that the Moon is in synchronous rotation with the Earth and the Earth's magnetotail is elongated with respect to the radial direction from the Sun. As a result, all the near-side swirls are subject to a decreased flux of solar wind ions compared to the far-side swirls.

Based on these two dichotomies, I posed constraints on the probability of the creation of lunar swirls by cometary impacts. I also indicated that the origin of the magnetic field in the area of lunar swirl is irrelevant to the rest of its evolution.

Based mainly on the observations of the principal component space, it was obvious that the micrometeoroid impacts do not induce the same complex of spectral changes as the solar wind ions, but I could not make a more exact description of the differences between the two space weathering agents at that point. That is why I decided to proceed with the laboratory experiments.

4.2 Paper II – Irradiations of silicates

In Paper II, I describe the ion- and laser-irradiation experiments of olivine and pyroxene pellets. This set of experiments was designed to better understand the difference in the effect of the two space weathering agents on the spectra of the most common silicate-rich materials.

The irradiations using the H^+ ions were done with the help of Dr. Kenichiro Mizohata at the University of Helsinki Accelerator Laboratory. He^+ and Ar^+ irradiations were conducted in the already well-established laboratory for that kind of experiments at IAS with the help of Dr. Cateline Lantz and Dr. Rosario Brunetto, see Sect. 3.1 for more details. The experimental set-up for the laser irradiations has been designed mainly by Prof. Petr Malý and me based on the experiments of Fazio et al. (2018).

This paper shows three major results:

1. There is a difference between the effect of the ion and laser irradiation on the longer NIR wavelengths. Laser irradiation caused greater changes at around 2 μm than ion irradiation. This was prescribed to the different penetration depths of the laser and ions. As laser penetrated deeper into the material, the spectral change is more significant. In the VIS part of the spectra, this difference is not evident probably because of the dependence of the extinction coefficients of the darkening agents on the wavelength. I thus expect that this means that the solar wind irradiation can be distinguished from the micrometeoroid impacts at NIR wavelengths.

2. The above-mentioned difference was the only one I identified in the data. Otherwise, it seemed that the original mineralogy of the irradiated material had a greater significance for the spectral evolution than the space weathering agent. This was demonstrated on the time-evolution plots in which the change in any spectral parameter is similar for the given material and varying space weathering agent, but different for the two materials.

3. Based on the findings, I could make several conclusions on the evolution of individual observed asteroids in the Solar system. For example, (433) Eros shows albedo changes, but no significant variations of the spectral slope. This is consistent with my finding that the spectral slope in olivine changes on short timescales, while in pyroxene, the change is mild. As Eros' surface is rather old, the olivine changes already saturated and we observe only pyroxene-related spectral changes, i.e. the slope is stable and albedo is still varying. Similarly, this work also explained the high observed spectral slopes in the A-type (olivine-rich) asteroids.

4.3 Paper III – Subsurface changes and their connection to the spectra

The samples I obtained during the irradiations for Paper II were the source material for the next examination. In Paper III, I examined what the sub-

surface structure of the pellets was and how it correlates with the observed spectral changes. The scanning and transmission electron microscopy analyses were conducted by Dr. Patricie Halodová at the Science Center Řež, see Sect. 3.3.

The main conclusion of this paper is that the main factor influencing the spectral changes is the presence of amorphous structures in the shallow subsurface layers that have sizes similar to the wavelength of incident light. I observed such structures in both H^+-irradiated samples and also in the laser-irradiated olivine. In laser-irradiated olivine, I also observed the nanophase iron particles that also have a major impact on the spectra, even in the NIR region.

The only sample that did not contain such small structures was the pyroxene irradiated by laser. This sample also showed a very distinct evolution of the spectra, as it did not exhibit changes in the spectral slope, only changes in the depths of the absorption bands and constant darkening.

Based on these observations, I could construct the subsurface evolution scenario. In the beginning of the evolution, the material will suffer from the creation of small vesicles in partially amorphous layers induced by solar wind ions. The subsurface changes will cause rapid changes to the VIS slope. Later the nanophase iron particles will appear which will contribute to the alteration of the NIR spectral slope as well. Only in the later stages will the spectral slope changes cease as the wavelength-sized structures will be overcome by the growing vesicles and thickened amorphous layer caused by an increased contribution of the micrometeoroid impacts.

5 General discussion

In this section, I will discuss how results from individual papers connect to each other and will make some more comments on the experiments than what can be found in the papers. In the end, I will connect the findings of this thesis to a broader perspective of the planetary science.

5.1 Lunar swirls and npFe^0

In Paper I, I discussed the differences in the trends inside and outside the swirls. I cited a paper by Trang et al. (2019), who noticed depletion of npFe^0 inside lunar swirls. I hypothesised that the smaller amount of npFe^0 particles is due to a different operation of micrometeoroid impacts in the shielded areas of lunar swirls.

Now, when I have knowledge about the subsurface changes from my experiments (Paper III), it seems that it also may be explained differently. In samples irradiated by H^+ ions, I observed only vesicles and amorphous layers. Based on the experiments, I would thus not have concluded that solar wind induces creation of npFe^0 at the timescales I simulated, i.e. the protected lunar swirl area should not contain almost any npFe^0 induced by exceptional solar wind ions.

The olivine sample irradiated by laser showed npFe^0 particles, but I have not identified them in the pyroxene sample irradiated by laser. It may thus mean that the creation of the npFe^0 particles is dependent not only on the weathering agent, but also on the material in the lunar swirl area. And also, that the present and by Trang et al. (2019) identified microphase iron particles may have been created by larger impacts than those I modelled in the experiments.

5.2 Surface amorphisation and penetration depths

In Appendix D of Paper II, I hypothesised that the spectral changes in olivine significantly increased starting with the fluence of 2×10^{17} H^+ ions/cm^2

because the sample had undergone a collapse of crystalline structure, i.e. amorphisation. Based on the findings from Paper III, I now know that this hypothesis was most probably correct, as I saw a significant partially amorphous layer in this sample. My experiments thus agree with the findings of Brucato et al. (2004).

At this point I also may comment on a statement of Demyk et al. (2004), who claimed that the maximum damage in the sample happens at the penetration depth of the impacting ions. For Paper II, I conducted the SRIM and TRIM simulations (The stopping and range of ions in matter and Transport of ions in matter, Ziegler et al., 1985). These simulations are based on a Monte Carlo code, which calculates interactions of the ions of given energy with a material consisting of layers of given thickness. One of the outputs of SRIM is the penetration depth of the ions in the material.

For my simulations, the average penetration depths of 5 keV H^+ ions were approximately 60 nm. Nevertheless, the images from the transmission electron microscopy (Paper III) revealed that the thickness of the amorphous layers in H^+-irradiated samples is approximately 200 nm. There is thus a mismatch of the values. It is obvious that the value of penetration depths from SRIM comes from a statistical distribution resulting from the simulation. Each ion may thus create the damage at slightly different locations. Additionally, the SRIM/TRIM simulations are done under several assumptions. The one which may explain the mismatch between the observed damage and the simulated penetration depth is the assumption that each of the simulating ions enters the un-altered material (the zero dose assumption). But in reality the later the ion hits the material the more different its behaviour in it will be, as the material will already be altered and the interactions will proceed in a different manner. Demyk et al. (2004) thus may be correct, but we cannot base our estimates of the thicknesses of the amorphous layers solely on the SRIM simulations.

5.3 Comments on the experimental approach

In Papers II and III, I focused on two minerals, olivine and pyroxene. These are very common in the silicate-rich airless planetary bodies in the Solar system (see, e.g. Binzel et al., 2004; de León et al., 2006; Isaacson et al., 2010). Nevertheless, as mentioned at the beginning of this thesis, these minerals occur in solid solution series. Having different abundance of Fe in my samples, the results could have differed, as seen by different results of my pyroxene experiments to experiments by Vernazza et al. (2006). Also, there are many other minerals that are very abundant in the Solar system, such as anorthositic plagioclase in lunar highlands (Bishop et al., 2019), which I did not focus on, but deserve to be studied in future research.

Hapke (2001) commented on the fact that only a loose porous surface weathers as it gives the opportunity of sputtering. When preparing the materials for the experiments, I bore this in mind. Finally, I decided to use pressed powder pellets instead of completely loose powder. The main reason was the need to transport the samples. Having only a pile of loose grains would make the transport uneasy. Nevertheless, even in my setup, the topmost grains created a rough surface which was loose to the extent that the top grains could have been blown away. But the compactness of the pellet assured that I did not mix the top and underlying layers when carrying the samples around the laboratory. Lantz et al. (2017) commented on the differences in spectral behaviour of loose powder and pressed pellets. In my experiments, I mainly compared the relative trends rather than absolute values, and

that is why I do not see the use of pressed pellets as problematic.

Also, when extracting the samples for transmission electron microscopy (Paper III), Dr. Patricie Halodová focused mainly on the areas of larger grains, as the focused-ion-beam thin section would break if it was done out of completely loose material. For that I see another benefit (to those commented on in Paper II) in using particles with sizes up to 106 μm for creation of pellets.

If conducting these experiments again, I should definitely focus on ion energies that would be more representative to the standard solar wind situation, i.e. 1 keV per each nucleon. Also, as noted in Paper II, my olivine samples suffered from contamination, which most probably did not influence the final results, but in the following research it may be beneficial to irradiate another olivine to cross-check my results.

5.4 Implications for planetary science

5.4.1 Origin of lunar swirls

My work on lunar swirls (Paper I) states that based on the dichotomies I found, it is unlikely that the cometary impact hypothesis of lunar swirl formation is correct. Looking at the issue with some time distance, I would slightly reformulate the result. The dichotomies may rather relate to the evolution of the swirls after their formation and be independent of the way the swirls formed. Additionally, as I already commented in Sect. 2.2.1, new evidence has been found that the swirl surface texture may be, on small scales, different to the surrounding material. This may support either the cometary impact hypothesis or the fine dust transport hypothesis.

5.4.2 Surface exposure age estimates

I have observed a difference in the effect of the two space weathering agents on longer NIR wavelengths, especially in the area of around 2 μm (Paper II). It seems that micrometeoroid impacts (simulated by laser shots) will have a greater impact on the spectra in that wavelength range than any of the ions I used.

As a consequence, the spectral slope will probably evolve fast soon after exposure of the material to a space environment, when the solar wind contribution is dominant. Later, as the NIR wavelengths will also be affected by increasing contribution of micrometeoroid impacts, the spectral slope changes will not be as pronounced because of the smaller relative difference at long and short wavelengths. Based on the changes in the NIR wavelengths, it thus may be possible to give rough estimates on the surface exposure ages of various areas on airless planetary bodies.

5.4.3 Material dependence

My experiments showed that spectral evolution due to space weathering (Paper II) is very dependent on the material on the surface of an airless planetary body. While olivine showed major changes of the spectral slope, pyroxene irradiated under the same or similar conditions experienced only a mild alteration of the spectral slope. Also the subsurface changes differed with respect to the mineral (Paper III). Laser irradiation developed presence of nanophase iron particles in olivine, but not in pyroxene. Similarly, H^+-irradiation caused vesicles that appeared in partially amorphous layers to be of different sizes and shapes in olivine and in pyroxene.

Such observations are consistent with previous works, see e.g. Weber et al. (2020) or Quadery et al. (2015), and have great consequences for studies of the Solar system. In general, it seems

that it is not possible to describe the effect of space weathering on the whole set of minerals that are usually found in the Solar system bodies. Furthermore, the same rules will not be valid even within one group of materials, such as silicates. On the other hand, very specific groups, such as the A-type asteroids, made mostly of one mineral, can be described by one overall trend. As A-type asteroids are composed mainly of olivine, I expect that their evolution will resemble the evolution of my olivine samples. And indeed, A-type asteroids are known to have high spectral slopes (Cruikshank et al., 1984; DeMeo et al., 2009), which matches my observations that olivine's spectral slope is significantly and quickly altered even by H^+ irradiation.

As a result of the dependency of space-weathering induced evolution of reflectance spectra on the surface mineralogy, I could explain the observed behaviour of asteroid (4) Vesta, which shows deep absorption bands and nearly no continuum changes (Pieters et al., 2012), which is consistent with my pyroxene simulations.

My laboratory simulations also help to explain observations of other asteroids. For example, asteroid (433) Eros is an S-type asteroid, which means that it is probably composed of a mixture of minerals, including olivine and pyroxene. Eros shows high albedo variations, but nearly no spectral slope changes (Clark et al., 2001). This may be explained by the fact that Eros' surface is rather old, so the spectral slope changes are already saturated, while the absorption bands and the albedo of pyroxene mineral are still changing as they take longer to develop. The surface of asteroid (25143) Itokawa, on the other hand, is considered young, which matches the fact that variations in spectral slope are observed on it (Hiroi et al., 2006), as the spectral slope changes have not been saturated yet.

5.4.4 Evolution due to space weathering

Based on this work, I could make a prediction of how a freshly exposed silicate-rich material and its spectrum will evolve in time. In the beginning, when solar wind irradiation is believed to be dominant, the material will suffer mainly of partial amorphisation of the topmost layers and creation of small vesicles, ten(s) of nm in diameter. This will cause changes mainly in the VIS spectral slope. Later in the evolution (approximately after 10^8 yr, Blewett et al., 2011), the contribution of the micrometeoroid impacts will increase, which should, based on my observations, have different results based on the material in question. Olivine-rich material will experience creation of nanophase iron particles, which will induce changes also to the NIR spectral slope, as previously mentioned also by Pieters et al. (2016). Spectra of pyroxene-rich material will, on the other hand, cease to be altered in the spectral slope, as the vesicles and the amorphous layer will grow. The changes will then be mainly in the depths of absorption bands and in overall darkening probably due to increased contribution of volume absorptions over surface scattering.

6 Final conclusions

The main conclusions of my thesis are:

- Spectral changes due to space weathering are more dependent on the original mineralogy of surface than on the space weathering agent. *(Observations of ion- and laser-irradiated pellets.)*

- Micrometeoroid impacts do not cause the same extent of changes as the solar wind irradiation or the two effects combined. *(Observations of lunar spectra.)*

- The two space weathering agents are discernible based on evolution of spectra in the region around 2 μm. In this region, micrometeoroid bombardment causes greater changes than solar wind irradiation. *(Observations of ion- and laser-irradiated pellets.)*

- The VIS spectral slope changes more significantly upon ion irradiation than micrometeoroid impacts. *(Observations of ion- and laser-irradiated pellets.)*

- H^+ irradiation influences surface morphology differently to the micrometeoroid impacts. *(Observations of scanning electron microscopy images.)*

- Spectral changes are dependent on dimensions and level of amorphisation of subsurface layers and on the presence of nanophase iron particles. *(Comparison of spectral changes and transmission electron microscopy images.)*

- Evolution of a silicate-rich spectrum will start in the VIS spectral slope changes. Later, also the NIR spectral slope will change in case nanophase iron particles develop in the material. Finally, the spectral slope will stop developing and only the absorption bands will evolve. *(Evaluation of time dependence of spectral changes.)*

Nevertheless, there are still many unknowns in the space weathering process and evolution of the reflectance spectra. It would thus be very beneficial to conduct additional irradiation experiments using more various minerals and also samples from meteorites and material brought to the Earth by space missions. This is partially happening as Lakshika Palamakumbure (from the University of Helsinki) conducts the same H^+ irradiation experiments as I did, using samples of the Avanhandava, Bjurböle, and Luotolax meteorites. Additionally, using more varied types of ions with more accurate energies or mixing the contribution of the space weathering agents on one sample could also give us new insights into the problem.

Proper understanding of the whole space weathering process is a complex task which requires gathering expertise from many different fields of science. I consider it very valuable that I managed to start cooperation with Dr. Patricie Halodová, who helped to enrich these analyses by the electron microscopy images. Continuing in establishing such types of cooperation have great potential for future research. Furthermore, based on my research, we now may be able to describe time evolution of surface albedo features on an A-type asteroid, which then may serve as an input to the calculations of the Yarkovsky and YORP effects.

Acknowledgements (sources)

I acknowledge the use of imagery from Lunar QuickMap (https://quickmap.lroc.asu.edu), a collaboration between NASA, Arizona State University & Applied Coherent Technology Corp.

The thesis has made use of NASA Astrophysics Data System Bibliographic Services.

References

Adams, J. B. (1974). "Visible and near-infrared diffuse reflectance spectra of pyroxenes as applied to remote sensing of solid objects in the solar system". *J. Geophys. Res.* 79, pp. 4829–4836.

Besse, S. et al. (2013). "A visible and near-infrared photometric correction for Moon Mineralogy Mapper (M^3)". *Icarus* 222, pp. 229–242.

Bhatt, M. et al. (2021). "Regolith Characteristics of the Reiner Gamma Swirl as Revealed by Polarimet-

ric Observations". In: *52nd Lunar and Planetary Science Conference.* Lunar and Planetary Science Conference, p. 2430.
Binzel, R. P. et al. (2004). "Observed spectral properties of near-Earth objects: results for population distribution, source regions, and space weathering processes". *Icarus* 170, pp. 259–294.
Bishop, J. L., J. F. Bell, III, and J. E. Moersch (2019). *Remote Compositional Analysis: Techniques for Understanding Spectroscopy, Mineralogy, and Geochemistry of Planetary Surfaces.* Cambridge Planetary Science. Cambridge University Press.
Blewett, D. T. et al. (2011). "Lunar swirls: Examining crustal magnetic anomalies and space weathering trends". *J. Geophys. Res. (Planets)* 116, E02002.
Brucato, J. R. et al. (2004). "Forsterite amorphisation by ion irradiation: Monitoring by infrared spectroscopy". *Astronomy and Astrophysics* 413, pp. 395–401. arXiv: astro-ph/0307402[astro-ph].
Brunetto, R., J. de León, and J. Licandro (2007). "Testing space weathering models on A-type asteroid (1951) Lick". *Astronomy and Astrophysics* 472.2, pp. 653–656.
Brunetto, R. and G. Strazzulla (2005). "Elastic collisions in ion irradiation experiments: A mechanism for space weathering of silicates". *Icarus* 179.1, pp. 265–273.
Brunetto, R. et al. (2015). "Asteroid Surface Alteration by Space Weathering Processes". In: *Asteroids IV*. Ed. by P. Michel, F. E. DeMeo, and W. F. Bottke, pp. 597–616.
Brunetto, R. et al. (2018). "Hyperspectral FTIR imaging of irradiated carbonaceous meteorites". *Planetary and Space Science* 158, pp. 38–45.
Brunetto, R. et al. (2020). "Characterizing irradiated surfaces using IR spectroscopy". *Icarus* 345, 113722.
Burns, R. G. (1970). "Mineralogical Applications of Crystal Field Theory". In: Cambridge University Press. Chap. *Electronic spectra of transition metal ions in silicate minerals*, p. 83.
Burns, R. G. (1989). "Spectral Mineralogy of Terrestrial Planets: Scanning Their Surfaces Remotely". *Mineralogical Magazine* 53.
Carvano, J. and J. Davallos (2014). "Solar-phase-angle effects on the taxonomic classification of asteroids". In: *Asteroids, Comets, Meteors 2014*. Ed. by K. Muinonen et al.
Cassidy, W. and B. Hapke (1975). "Effects of darkening processes on surfaces of airless bodies". *Icarus* 25, pp. 371–383.
Chapman, C. R. (2004). "Space Weathering of Asteroid Surfaces". *Annual Review of Earth and Planetary Sciences* 32, pp. 539–567.
Chrbolková, K. et al. (2021). "Comparison of space weathering spectral changes induced by solar wind and micrometeoroid impacts using ion- and femtosecond-laserirradiated olivine and pyroxene". *Astronomy and Astrophysics* 654, A143. arXiv: 2108.00870[astro-ph.EP].
Clark, B. E. et al. (2001). "Space weathering on Eros: Constraints from albedo and spectral measurements of Psyche crater". *Meteoritics and Planetary Science* 36.12, pp. 1617–1637.
Clark, R. N. (1999). "Spectroscopy of Rocks and Minerals, and Principles of Spectroscopy". In: *Manual of Remote Sensing*, Volume 3, Remote Sensing for the Earth Sciences, 3rd Edition. Ed. by A. N. Rencz and R. A. Ryerson, pp. 3–52.
Clark, R. N. et al. (2011). "Thermal removal from near-infrared imaging spectroscopy data of the Moon". *J. Geophys. Res. (Planets)* 116, E00G16.
Clénet, H. et al. (2011). "A new systematic approach using the Modified Gaussian Model: Insight for the characterization of chemical composition of olivines, pyroxenes and olivine-pyroxene mixtures". *Icarus* 213.1, pp. 404–422.
Connolly, A. J. and J. T. VanderPlas (2014). "Statistics, Data Mining, and Machine Learning in Astronomy: A Practical Python Guide for the Analysis of Survey Data". In: Princeton University Press. Chap. *Dimensionality and Its Reduction*, pp. 289–302.
Corley, L. M., J. J. Gillis-Davis, and P. H. Schultz (2017). "A Comparison of Kinetic Impact and Laser Irradiation Space Weathering Experiments". In: *Lunar and Planetary Science Conference*. Vol. 48. Lunar and Planetary Inst. Technical Report, p. 1721.
Cruikshank, D. P. and W. K. Hartmann (1984). "The Meteorite-Asteroid Connection: Two Olivine-Rich Asteroids". *Science* 223.4633, pp. 281–283.
Cymes, B. A., K. D. Burges, and R. M. Stroud (2022). "Helium-bearing "vesicular" nanophase metallic iron particles in lunar regolith grains". In: *Lunar and Planetary Science Conference*. Vol. 53. Lunar and Planetary Inst. Technical Report, p. 2023.
de León, J. et al. (2006). "Spectral analysis and mineralogical characterization of 11 olivine pyroxene rich NEAs". *Advances in Space Research* 37.1, pp. 178–183.
de Smith, M. J. (2018). *Statistical Analysis Handbook*. The Winchelsea Press, Drumlin Security Ltd, Edinburgh.
DeMeo, F. E. et al. (2009). "An extension of the Bus asteroid taxonomy into the near-infrared". *Icarus* 202, pp. 160–180.
Demyk, K. et al. (2004). "IR spectroscopic study of olivine, enstatite and diopside irradiated with low energy H^+ and He^+ ions". *Astronomy and Astrophysics* 420, pp. 233–243.
Dobrică, E. and R. C. Ogliore (2016). "Adhering grains and surface features on two Itokawa particles". *Earth, Planets and Space* 68, 21.
Fazio, A. et al. (2018). "Femtosecond laser irradiation of olivine single crystals: Experimental simulation of space weathering". *Icarus* 299, pp. 240–252.
Fiege, K. et al. (2019). "Space Weathering Induced

Via Microparticle Impacts: 2. Dust Impact Simulation and Meteorite Target Analysis". *Journal of Geophysical Research (Planets)* 124.4, pp. 1084–1099.

Fulvio, D. et al. (2012). "Space weathering of Vesta and V-type asteroids: new irradiation experiments on HED meteorites". *Astronomy and Astrophysics* 537, L11.

Fulvio, D. et al. (2021). "Micrometeorite bombardment simulated by ns-pulsed laser ablation: Morphological characterization of the impact craters". *Icarus* 366, 114532.

Gillis-Davis, J. J. et al. (2018). "Laser and Electron Weathering Experiments on Murchison (CM2) Meteorite". In: *Lunar and Planetary Science Conference*. Vol. 49. Lunar and Planetary Inst. Technical Report, p. 2051.

Glotch, T. D. et al. (2015). "Formation of lunar swirls by magnetic field standoff of the solar wind". *Nature Communications* 6, 6189.

Gold, T. (1955). "The lunar surface". *Monthly Notices of the Royal Astronomical Society* 115, p. 585.

Gradie, J., J. Veverka, and B. Buratti (1980). "The effects of scattering geometry on the spectro-photometric properties of powdered material." *Lunar and Planetary Science Conference Proceedings* 1, pp. 799–815.

Green, R. O. et al. (2011). "The Moon Mineralogy Mapper (M3) imaging spectrometer for lunar science: Instrument description, calibration, on-orbit measurements, science data calibration and on-orbit validation". J. *Geophys. Res. (Planets)* 116, E00G19.

Hapke, B. (1965). "Effects of a Simulated Solar Wind on the Photometric Properties of Rocks and Powders". *Annals of the New York Academy of Science*s 123, pp. 711–721.

Hapke, B. (1977). "Interpretations of optical observations of Mercury and the moon". *Physics of the Earth and Planetary Interiors* 15, pp. 264–274.

Hapke, B. (2001). "Space weathering from Mercury to the asteroid belt". *J. Geophys. Res.* 106, pp. 10039–10074.

Hapke, B. W. et al. (1970). "Solar radiation effects on the optical properties of Apollo 11 samples". *Geochimica et Cosmochimica Acta Supplement* 1, p. 2199.

Harries, D. et al. (2016). "Secondary submicrometer impact cratering on the surface of asteroid 25143 Itokawa". *Earth and Planetary Science Letters* 450, pp. 337–345.

Hiroi, T. et al. (2006). "Developing space weathering on the asteroid 25143 Itokawa". *Nature* 443, pp. 56–58.

Hood, L. L. and G. Schubert (1980). "Lunar magnetic anomalies and surface optical properties". *Science* 208, pp. 49–51.

Hood, L. L. and C. R. Williams (1989). "The lunar swirls - Distribution and possible origins". In: *Lunar and Planetary Science Conference Proceedings*. Ed. by G. Ryder and V. L. Sharpton. Vol. 19. Lunar and Planetary Science Conference Proceedings, pp. 99–113.

Isaacson, P. J. and C. M. Pieters (2010). "Deconvolution of lunar olivine reflectance spectra: Implications for remote compositional assessment". *Icarus* 210.1, pp. 8–13.

Kaňuchová, Z. et al. (2010). "Space weathering of asteroidal surfaces. Influence on the UV-Vis spectra". *Astronomy and Astrophysics* 517, A60.

Keller, L. P. and D. S. McKay (1993). "Discovery of Vapor Deposits in the Lunar Regolith". *Science* 261.5126, pp. 1305–1307.

Keller, L. P., S. J. Wentworth, and D. S. McKay (1998). "Space Weathering: Reflectance Spectroscopy and TEM Analysis of Individual Lunar Soil Grains". In: *Lunar and Planetary Science Conference*. Vol. 29. Lunar and Planetary Science Conference.

Kling, A. et al. (2021). "Coordinated analysis of space weathering characteristics in lunar samples to understand water distribution on the Moon". *Microscopy and Microanalysis* 27.S1, pp. 2260–2262.

Kohout, T. et al. (2014). "Space weathering simulations through controlled growth of iron nanoparticles on olivine". *Icarus* 237, pp. 75–83. arXiv: 1404.2956[astro-ph.EP].

Kramer, G. Y. et al. (2011). "M3 spectral analysis of lunar swirls and the link between optical maturation and surface hydroxyl formation at magnetic anomalies". *J. Geophys. Res. (Planets)* 116, E00G18.

Lantz, C. et al. (2017). "Ion irradiation of carbonaceous chondrites: A new view of space weathering on primitive asteroids". *Icarus* 285, pp. 43–57.

Loeffler, M. J., C. A. Dukes, and R. A. Baragiola (2009). "Irradiation of olivine by 4 keV He^+: Simulation of space weathering by the solar wind". *J. Geophys. Res. (Planets)* 114.E3, E03003.

Matsumoto, T. et al. (2015). "Surface and internal structures of a space-weathered rim of an Itokawa regolith particle". *Icarus* 257, pp. 230–238.

McCord, T. B. and T. V. Johnson (1970). "Lunar Spectral Reflectivity (0.30 to 2.50 Microns) and Implications for Remote Mineralogical Analysis". *Science* 169, pp. 855–858.

McCord, T. B. et al. (1981). "Moon - Near-infrared spectral reflectance, a first good look". *J. Geophys. Res.* 86, pp. 10883–10892.

Neugebauer, M. et al. (1972). "Solar wind observations on the lunar surface with the Apollo-12 ALSEP". *Planetary and Space Science* 20, pp. 1577–1591.

Noble, S. K., C. M. Pieters, and L. P. Keller (2007). "An experimental approach to understanding the optical effects of space weathering". *Icarus* 192, pp. 629–642.

Noble, S. K. et al. (2015). "The Microstructure of a

Micrometeorite Impact into Lunar Olivine". In: *Space Weathering of Airless Bodies: An Integration of Remote Sensing Data, Laboratory Experiments and Sample Analysis Workshop*. Vol. 1878. LPI Contributions, p. 2034.

Noguchi, T. et al. (2011). "Incipient Space Weathering Observed on the Surface of Itokawa Dust Particles". *Science* 333, p. 1121.

Noguchi, T. et al. (2014a). "Mineralogy of four Itokawa particles collected from the first touchdown site". *Earth, Planets and Space* 66, 124.

Noguchi, T. et al. (2014b). "Space weathered rims found on the surfaces of the Itokawa dust particles". *Meteorit. Planet. Sci.* 49.2, pp. 188–214.

Pieters, C. M. and S. K. Noble (2016). "Space weathering on airless bodies". *J. Geophys. Res. (Planets)* 121, pp. 1865–1884.

Pieters, C. M. et al. (2000). "Space weathering on airless bodies: Resolving a mystery with lunar samples". *Meteorit. Planet. Sci.* 35, pp. 1101–1107.

Pieters, C. M. et al. (2012). "Distinctive space weathering on Vesta from regolith mixing processes". *Nature* 491.7422, pp. 79–82.

Quadery, A. H. et al. (2015). "Atomic-scale simulation of space weathering in olivine and orthopyroxene". *J. Geophys. Res. (Planets)* 120.4, pp. 643–661.

Reddy, V. et al. (2015). "Mineralogy and Surface Composition of Asteroids". In: *Asteroids IV*. Ed. by P. Michel, F. E. DeMeo, and W. F. Bottke, pp. 43–63.

Rubincam, D. P. (2000). "Radiative Spin-up and Spin-down of Small Asteroids". *Icarus* 148, pp. 2–11.

Salisbury, J. W., D. M. D'Aria, and E. Jarosewich (1991). "Midinfrared (2.5-13.5 μm) reflectance spectra of powdered stony meteorites". *Icarus* 92.2, pp. 280–297.

Sanchez, J. A. et al. (2012). "Phase reddening on near-Earth asteroids: Implications for mineralogical analysis, space weathering and taxonomic classification". *Icarus* 220, pp. 36–50. arXiv: 1205.0248[astro-ph.EP].

Sasaki, S. et al. (2001). "Production of iron nanoparticles by laser irradiation in a simulation of lunar-like space weathering". *Nature* 410.6828, pp. 555–557.

Sasaki, S. et al. (2002). "Simulation of space weathering by nanosecond pulse laser heating: dependence on mineral composition, weathering trend of asteroids and discovery of nanophase iron particles". *Advances in Space Research* 29.5, pp. 783–788.

Schultz, P. H. and L. J. Srnka (1980). "Cometary collisions on the Moon and Mercury". *Nature* 284, pp. 22–26.

Stubbs, T. J., R. R. Vondrak, and W. M. Farrell (2006). "A dynamic fountain model for lunar dust". *Advances in Space Research* 37, pp. 59–66.

Sturges, H. A. (1926). "The Choice of a Class Interval". *Journal of the American Statistical Association* 21.153, pp. 65–66.

Sunshine, J. M., C. M. Pieters, and S. F. Pratt (1990). "Deconvolution of mineral absorption bands - An improved approach". *J. Geophys. Res.* 95, pp. 6955–6966.

Sunshine, J. M. et al. (1999). "Absorption Band Modeling in Reflectance Spectra: Availability of the Modified Gaussian Model". In: *Lunar and Planetary Science Conference*. Vol. 30. Lunar and Planetary Inst. Technical Report, p. 1306.

Trang, D. and P. G. Lucey (2019). "Improved space weathering maps of the lunar surface through radiative transfer modeling of Kaguya multiband imager data". *Icarus* 321, pp. 307–323.

Vernazza, P. et al. (2006). "Asteroid colors: a novel tool for magnetic field detection? The case of Vesta". *Astronomy and Astrophysics* 451.3, pp. L43–L46.

Vernazza, P. et al. (2013). "Paucity of Tagish Lake-like parent bodies in the Asteroid Belt and among Jupiter Trojans". *Icarus* 225.1, pp. 517–525.

Vokrouhlický, D. et al. (2015). "The Yarkovsky and YORP Effects". *ArXiv e-prints*. arXiv: 1502.01249[astro-ph.EP].

Weber, I. et al. (2020). "Space weathering by simulated micrometeorite bombardment on natural olivine and pyroxene: A coordinated IR and TEM study". *Earth and Planetary Science Letters* 530, 115884.

Wehner, G. K., C. E. Kenknight, and D. Rosenberg (1963). "Modification of the lunar surface by the solar-wind bombardment". *Planet. Space Sci.* 11, pp. 1257–1261.

Yamada, M. et al. (1999). "Simulation of space weathering of planet-forming materials: Nanosecond pulse laser irradiation and proton implantation on olivine and pyroxene samples". *Earth, Planets, and Space* 51, p. 1265.

Yang, Y. Z. et al. (2017). "Phase Reddening of Pure Minerals with Different Albedo". In: *Lunar and Planetary Science Conference*. Vol. 48. Lunar and Planetary Inst. Technical Report, p. 2240.

Zhang, P. et al. (2022). "Diverse space weathering effects on asteroid surfaces as inferred via laser irradiation of meteorites". *Astronomy and Astrophysics* 659, A78.

Ziegler, J. F. and J. P. Biersack (1985). "The Stopping and Range of Ions in Matter". In: *Treatise on Heavy-Ion Science*, p. 93.

Paper I

Chrbolková, K., Kohout, T., and Ďurech, J.

Reflectance spectra of seven lunar swirls examined by statistical methods: A space weathering study.

Icarus, 2019, 333, 516-527.

Icarus 333 (2019) 516–527

Contents lists available at ScienceDirect

Icarus

journal homepage: www.elsevier.com/locate/icarus

Reflectance spectra of seven lunar swirls examined by statistical methods: A space weathering study

Kateřina Chrbolková[a,b,*], Tomáš Kohout[a,c], Josef Ďurech[b]

[a] Department of Geosciences and Geography, Faculty of Science, University of Helsinki, Gustaf Hällströmin katu 2, 00560 Helsinki, Finland
[b] Astronomical Institute, Faculty of Mathematics and Physics, Charles University, V Holešovičkách 2, 18000 Prague, Czech Republic
[c] Institute of Geology, The Czech Academy of Sciences, Rozvojová 269, 16500 Prague, Czech Republic

ARTICLE INFO

Keywords:
Space weathering
Moon
Surface
Lunar swirls
Spectra
Principal component analysis

ABSTRACT

Higher magnetic field in lunar swirls is believed to deflect majority of incoming charged particles away from the lunar-swirl surfaces. As a result, space weathering inside and outside swirls should be different. We wanted to evaluate these differences, therefore we have examined seven swirl areas on the Moon (four mare and three highland swirls). We applied the Modified Gaussian Model to statistical sets of the Moon Mineralogy Mapper spectra. Using Principal Component Analysis (PCA), we were able to distinguish the old (weathered) material from both the fresh crater and swirl materials. The swirls did not follow the same behavior as the fresh material, nor were they fully separable. Additionally, we could distinguish between the mare and highland swirls (mare/highland dichotomy) based on the PCA and histogram plots of the albedo and strength of the 1000-nm absorption band. The mare/highland dichotomy can partially be caused by different FeO content in maria and highlands, which points to the existence of a threshold value that changes the spectral evolution due to space weathering. Slope behavior seemed to be dependent on whether the swirl was on the near- or far-side of the Moon, likely due to shielding of lunar nearside by Earth's magnetotail. Our results thus favor the solar wind stand-off hypothesis in combination with the fine dust transport hypothesis and point to the fact that micrometeoroid impacts generally do not reproduce the same weathering trends as all the space weathering effects together.

1. Introduction

1.1. Space weathering

Our knowledge of the mineralogy of most of the small Solar System bodies is in some cases based on meteorite falls (Shestopalov et al., 2010), and sample-return missions such as the Hayabusa (Mikouchi et al., 2014) and the Stardust mission (Simon et al., 2008), or currently operating Hayabusa 2 (Tsuda et al., 2013) and OSIRIS-REx missions (Lauretta et al., 2017). However, in most cases, we are still dependent on remotely measured reflectance spectra (Gaffey et al., 1993; Shuai et al., 2013). A spectrum of an airless planetary body is controlled by surface properties, which are influenced by so-called *space weathering* (i.e., Hapke, 2001). The term space weathering describes how a set of effects, including the solar wind, galactic radiation, and micrometeoroid impacts causes chemical and physical changes to the airless planetary surfaces. Among other changes such as formation of agglutinates and blistering, space weathering creates small particles of metallic iron (so-called nanophase iron, npFe^0) in thin rims of regolith grains, which diminish the albedo, spectral contrast (absorption band depth), and increase the spectral slope (Hapke, 2001; Matsumoto et al., 2015; Pieters and Noble, 2016; Pieters et al., 2000). These effects complicate our interpretation of mineralogy.

As Pieters et al. (2000) pointed out, space weathering is a complicated problem because the different effects causing the spectral changes vary with location in the Solar System. Another important factor is mineralogy, especially the amount of iron in silicates. The more iron present in the silicate material, the more efficiently is the nanophase iron produced. A relationship between the size of the npFe^0 particles and the spectral changes was reviewed for example by Blewett et al. (2011).

Several works described how the whole set of processes (solar wind and micrometeoroid impacts) influence the spectra of airless bodies (for example Hapke, 2001; Pieters et al., 2000). Noguchi et al. (2011) studied particles from the asteroid Itokawa and concluded that typical timescales of the solar wind weathering are 10^4 to 10^6 years, whereas in

* Corresponding author at: Gustaf Hällströmin katu 2 (Physicum), P.O. Box 64, FI-00014 University of Helsinki, Finland.
E-mail address: katerina.chrbolkova@helsinki.fi (K. Chrbolková).

https://doi.org/10.1016/j.icarus.2019.05.024
Received 1 November 2018; Received in revised form 16 May 2019; Accepted 20 May 2019
Available online 29 May 2019

the case of micrometeoroid impacts it is longer, 10^8 to 10^9 years. Also, Sim et al. (2017) reported a variation in crater-walls' weathering, which they prescribed to a differing solar wind flux due to passage of the Moon through the Earth's magnetotail. Similar conclusions were made by Hemingway et al. (2015) based on latitudinal variations of the spectra across the lunar maria. However, the exact description of these changes is still lacking, and we cannot assign a specific change in the spectra to a specific weathering process.

1.2. Lunar swirls

Very valuable natural laboratories for space weathering studies are the so-called *lunar swirls*. Lunar swirls are areas on the Moon that have brighter albedo, and are usually of a curved shape (Blewett et al., 2011; Hood et al., 1979a; (Hood and Williams, 1989). All known swirls lie in places of amplified magnetic field (Blewett et al., 2011; Hood et al., 1979a; Hood et al., 1979b) and many of them are antipodal to major impact basins (Hood and Artemieva, 2008). An example of a lunar swirl is the Gerasimovich anomaly – which is also an area of the strongest magnetic field on the Moon – or other well-known swirls such as Reiner Gamma or Mare Ingenii (Blewett et al., 2011).

Origin of lunar swirls

One of the main hypotheses for formation of lunar swirls is that amplified magnetic field shields surface of swirls from solar wind and so space weathering is diminished in them and they look fresh (herein referred to as the solar wind stand-off hypothesis; Deca et al., 2018; Glotch et al., 2015; Hemingway and Garrick-Bethell, 2012; Hood and Schubert, 1980). The idea of charged particles being deflected away from lunar swirl areas was described for example by Hood and Williams (1989). This hypothesis is often connected to the antipodal hypothesis, which prescribes the origin of a magnetic anomaly to a collision of ejecta from an impact creating an antipodal basin Hood et al. (2001). This hypothesis correlates with recent study done by Kelley and Garrick-Bethell (2019), who found that the magnetic anomalies in the Gerasimovich region are offset to the west with respect to the Crisium antipode, which in accordance with the slight rotation of the Moon during the ejecta's circulation around the Moon. Although, not all lunar swirls are in the positions antipodal to some impact basin. Magnetic-field measurements done by Lunar Prospector mission support the validity of the solar wind stand-off hypothesis in the Imbrium antipode (Lin et al., 1998).

Another option proposed at approximately same time as the solar wind stand-off hypothesis is a hypothesis of relatively recent impacts of a system of comets onto the surface of the Moon (Schultz and Srnka, 1980; Syal et al., 2015). In the place of the impact, turbulent flows of cometary coma should have (1) heated the material above the Curie temperature, which caused magnetization of the surface; (2) deposited or altered the top-most regolith layer. This alteration would result in distinct surface roughness in the swirl area (Pinet et al., 2000), but such option was mostly ruled out by the Diviner and Mini-RF data (Glotch et al., 2015; Jozwiak and Blewett, 2017; Kramer et al., 2011a) as the swirls have similar cm-scale roughness as their surroundings.

Garrick-Bethell et al. (2011) suggested that lunar swirls are bright thanks to an accumulation of fine feldspathic (bright) regolith in swirl areas. Based on the theory, the fine fraction of regolith should be electrostatically lofted during terminator crossings, and transported by weak electric potentials that are created in the vicinity of swirls. Alternatively, nearby impacts could have distributed fine material over large areas – even to swirls and they thus look fresh.

Despite the previous research, the origin of swirls is still unknown and it is possible that they were formed and still look fresh due to a combination of the above-mentioned effects.

1.3. Multispectral datasets

This work uses a multispectral dataset, as it has the potential to support us with valuable information concerning space weathering and lunar research. For example analysis of data from the Clementine probe by Blewett et al. (2005) showed that the Descartes swirl is probably an ejecta material from the two nearby craters, which has high albedo due to lower maturity. Later, Blewett et al., (2011) presented other results based on Clementine dataset, suggesting that swirls have spectral characteristics of immature material. Their findings contradict the cometary hypothesis, but are in accordance with the solar wind stand-off hypothesis and the dust-levitation hypothesis. Kramer et al. (2011b) showed, on spectra from small craters in lunar-swirls' areas, that swirls are not immature, even though they look fresh. Based on the Clementine data, latitudinal variation in spectral properties of lunar maria (that match the situation in lunar swirls) was shown by Hemingway et al. (2015). This result is in favor of the solar wind flux reduction in the swirls' areas as proposed by the stand-off hypothesis.

The Moon Mineralogy Mapper (M^3) spectra can be used to identify fresh craters, as shown by Nettles et al. (2011). They used the spectra to evaluate the maturity trends in fresh craters and their rays. Kramer et al. (2011a) also used the M^3 dataset, specially in areas of three lunar swirls (Reiner Gamma, Gerasimovich, and Mare Ingenii), to evaluate the characteristics of fresh craters and mature soils, and on- and off-swirl trends. They found that on-swirl craters have higher albedo and more intense absorption features than off-swirl craters. They also proposed that the maturation process is retarded inside swirls because the solar wind ions are deflected to adjacent areas, which are, on the other hand, more weathered.

Denevi et al. (2014), using data from the Lunar Reconnaissance Orbiter's Wide Angle Camera, pointed out that the spectral slope in the ultraviolet wavelength range is decreasing not increasing with maturation.

Very recent work by Trang and Lucey (2019) used data from the Kaguya Multiband Imager and mapped the abundance of different sizes of nanophase iron across the lunar swirl areas.

Not only the Moon was spectrally measured, the Itokawa asteroid's multispectral data showed that the darker areas have usually spectra with higher spectral slope (Hiroi et al., 2006) and that the albedo vary from the regions that are expected to be fresh (such as crater walls) to the mature regions (Ishiguro et al., 2007).

Our goal is to determine the spectral characteristics of the swirl material in comparison with fresh (crater) material and old (weathered, mature) material by deliberate targeted selection of statistical sets of spectral data, which is a different approach to previous works done for example by Kramer et al. (2011a) or Trang and Lucey (2019) who mapped whole areas of swirls at once or chose only few points to compare the spectral characteristics. This is how we want to evaluate how the swirl material behaves and to get some clue on which hypothesis explaining swirl immaturity is the more probable one. If the solar wind stand-off hypothesis is correct, soils inside the swirl are affected mainly by micrometeoroid impacts and we should be able to identify how micrometeoroids influence the spectral trends compared to the complete weathering in the surrounding material and fresh crater material. Thus, we propose our main hypothesis: the sequence of values of a given spectral parameter, should be as follows: **crater → swirl → mature material**. In other words, our central hypothesis is that swirl material should exhibit intermediate behavior with respect to fresh crater material and mature terrains due to smaller amount of effects causing the space weathering.

In this article, we analyze spectra of seven lunar swirl areas: Reiner Gamma, Rima Sirsalis, Mare Marginis, Mare Ingenii, Airy, Descartes, and Gerasimovich. The first four represent mare swirls, the remaining three are highland swirls. The Rima Sirsalis swirl was proposed to be a part of the Reiner Gamma formation by Hood et al. (2001). Lee et al. (2019) supported this idea as they found that the magnetizations of

these two swirls are aligned. However, their distance is larger than 200 km and Rima Sirsalis is nearer to the highland regions than Reiner Gamma, we thus analyze them separately.

2. Choice of the data and methods

For our work, we used lunar spectra (Section 2.1), which we processed with an adaptation of the Modified Gaussian Model (MGM) (Sunshine et al., 1990; Sunshine et al., 1999), see Section 2.2. With this model, we got three major spectral parameters: the spectral slope, albedo, and strength of the 1000-nm band. We applied three different approaches to analyze our data/spectral parameters (histogram plots, spectral stacking, and Principal Component Analysis, described in Section 2.3). Original data, files with results, and our MATLAB code are available at https://doi.org/10.5281/zenodo.1473816.

2.1. Datasets

A list of the swirls we used for this study is at the end of Section 1. We have chosen these seven swirls in order to cover different locations on the Moon (the near and far side, northern and southern hemisphere, etc.). The main constraints were: good-quality coverage of the swirl by spectral data, nearly homogeneous surface mineralogy, and not very diverse geological settings in the area of the given swirl and its close vicinity.

Spectra were recorded in the years 2008 to 2009 by the Moon Mineralogy Mapper (M^3) carried by the Chandrayaan-1 spacecraft (Green et al., 2011). M^3 captured 95% of the lunar surface in two mapping modes. We use data from the "Global Mode" (more precisely Level 2 reflectance data), as they covered a much larger area. This mode obtains 83 spectral channels ranging from 541 to 2976 nm. Each spectrum was thermally (Clark et al., 2011) and photometrically corrected (Besse et al., 2013).

We downloaded the spectral cubes from the Planetary Data System, Geosciences Node[1] (see the Online Supplementary Material, Table S1, for a list of spectral cubes and positions of the areas we used), and then chose spectra for our analysis with the ENVI software. Before further processing, we normalized the spectra at 750 nm.

In each swirl, we visually identified four distinct terrains: (1) fresh crater material outside the swirl formation (in this article marked as *fresh out*), (2) fresh crater material inside the swirl (*fresh in*), (3) swirl material that is distant from the fresh craters (*mature in*), and (4) old weathered material outside the swirl distant from any fresh crater (*mature out*). For each terrain of a given swirl, we chose several tens to hundreds of spectra. The number was dependent on the availability of spectral data for a given type of terrain. We have chosen spectra so that the given terrain is represented by several areas latitudinally and longitudinally spread over the swirl. The fresh craters were identified by the visual presence of the sharp rays, and we chose spectra that were outside the center of the crater but not too far from it to avoid possible mixing with the background mature material. Especially in the highland regions, the identification of the *fresh in* and *fresh out* terrains was more demanding because of the lower albedo contrast of the material, see Fig. 1. The total number of spectra for each swirl are as follows: Reiner Gamma (1324), Rima Sirsalis (179), Mare Ingenii (600), Mare Marginis (887), Airy (538), Descartes (1056), and Gerasimovich swirl (829).

2.2. Adaptation of MGM

The Modified Gaussian Model (MGM) for fitting olivine and pyroxene mineral absorption spectra was developed by Sunshine et al. (1990) and further distributed in several formats (Sunshine et al., 1999). We used the codes written in MATLAB. MGM generally fits an input spectrum as a sum of a polynomial-shaped continuum and a given number of absorption bands represented by modified[2] Gaussian distributions, see (Sunshine et al., 1990). The fit is done in the natural logarithm of reflectance, $\ln(R)$, and energy, $1/\lambda$, as this allows for a simple mathematical summation of the absorption bands and continuum. The main reason for the choice of these variables is the existence of the Lambert-Beer's law explaining relation between the reflectance and exponential of the absorption coefficient, thus natural logarithm of reflectance and sum of individual absorption features.

Sunshine et al. (1990) originally produced a code that works in an interactive way, enabling a user to fit one spectrum at a time. We wanted to treat several tens to hundreds of spectra in one run. Thus, we developed a simple routine that estimated input parameters to MGM for each individual spectrum:

1. We fitted the overall continuum (the wavelength range was from approximately 660 nm to 2936 nm) by a linear function to obtain the estimates of the offset and slope of the continuum.
2. We fitted the 1000- and 2000-nm absorption bands by second-order polynomials.
3. A difference between the reflectance value at a given wavelength in the 1000- and 2000-nm band and the corresponding reflectance of the continuum fitted in the area of the band (local continuum), gave estimates of the absorption bands' strengths.
4. A parallel line to the local continuum over the band in one half of the depth of the band, supplied us with the Full Width at Half Maximum (FWHM). Where the line intersected the band's fit from point 2, we marked two points. Their wavelength difference was FWHM.
5. We had a minimum of two[3] absorption bands (at 1000 and 2000 nm), the third band around 1200 nm was added when the angle between the continuum and a straight-line fit of the 1200-nm region was above a certain value (0.55 rad). We added the fourth band at 3000 nm based on its visual presence, which only happened when we used the stacking method (Section 2.3.2) and we did not evaluate the parameters of this band.
6. When we had the input parameters, we ran MGM to get the optimized spectral parameters.

For an illustration of these steps see Fig. 2. Our estimation routine significantly improved the ability of MGM to converge to physically realistic solutions.

The 1000-nm absorption band in our spectra is probably caused by electron excitations of Fe^{2+} ions in M_2 positions in pyroxenes (Burns, 1989). Partial contribution to this band can also have olivine, which creates a broad absorption around 1000 nm that is made of three bands due to electron excitations in Fe^{2+} ions in M_2 (strong central absorption) and M_1 (weaker absorptions and shoulders) sites (Burns, 1970). The M^3 data are not of good enough quality for us to have a unique solution with three bands, though. Therefore, we used only one band to have the model constrained. Klima et al. (2007) showed that the 1200-nm band is caused by Fe^{2+} ions in M_1 sites in pyroxenes and its intensity is higher the higher is the iron content of the pyroxene.

2.3. Methods

We followed three different approaches: statistical evaluation of our results using histogram plots (Section 2.3.1), spectral stacking (Section 2.3.2), and the Principal Component Analysis (Section 2.3.3).

[1] http://ode.rsl.wustl.edu/moon/index.aspx

[2] Modification allows for asymmetric appearance of the Gaussian curve.

[3] With the exception of the Descartes swirl, where we were unable to detect the 1000-nm band.

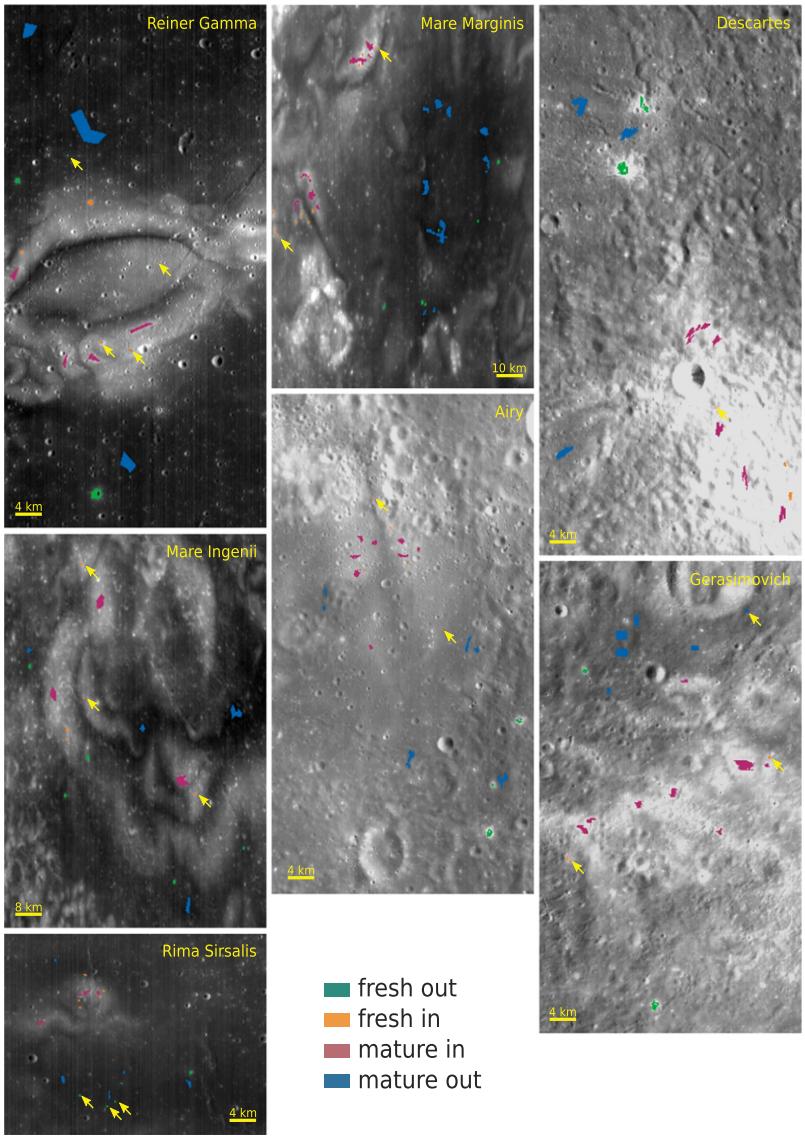

Fig. 1. Swirls from this study shown as 750-nm reflectance images with highlighted pixels of the Moon Mineralogy Mapper's spectra we used for our analysis. Each terrain has a different color (color-coding is consistent throughout the whole article). Groups of only few pixels that are difficult to be seen were additionally marked by yellow arrows to increase their visibility. All images have adjusted contrast and brightness to enable easier identification of locations of pixels we used. For coordinates of centers of individual images in the mosaic see the Online Supplementary Material, Table S1; for individual images, see Figs. S1 to S7. (For interpretation of the references to color in this figure legend, the reader is referred to the web version of this article.)

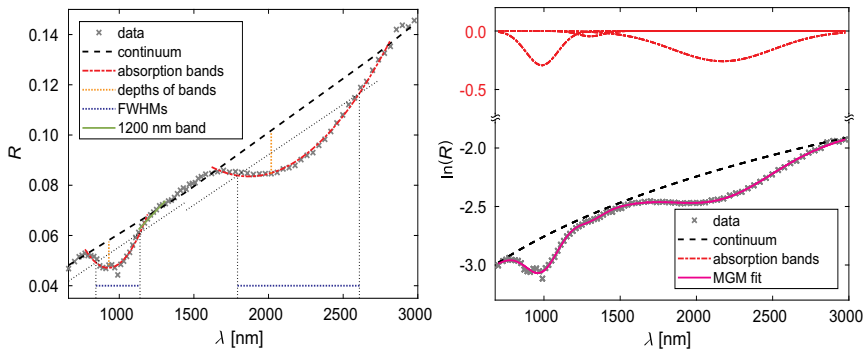

Fig. 2. (left) An output plot of our routine for estimation of input parameters to MGM. The wavelength is denoted λ, *R* stands for the reflectance. The spectrum belongs to fresh Reiner Gamma crater material outside the swirl (*fresh out*). (right) An optimized fit done in MGM based on the input parameters from our routine.

2.3.1. Histogram plots

In the first approach, we took all the spectra from a given terrain in a swirl and fitted them with MGM. This gave us four statistical sets (for four terrains in one swirl) of the spectral parameters important for our space weathering study (namely the spectral slope, albedo,[4] and strength of the 1000-nm band). Although we fitted the 2000-nm band, we did not evaluate its strength because of the lower quality of the data at longer wavelengths, caused by the imperfect thermal correction and higher relative noise influencing the depth estimate.

When we had all the fits, we created a histogram plot (using the Probability density function normalization and Sturges' binning algorithm, Sturges, 1926) of the four statistical sets/terrains of the given swirl, which we further evaluated using the terrains' mean values. To test our hypothesis about the intermediate behavior of swirl material (Section 1), we analyzed the sequence of the four means of the chosen spectral parameter. We had to assess if this sequence is statistically unambiguous (two means do not switch their positions with a slight change of the dataset). Thus, we proposed a null hypothesis: *The two tested mean values are the same*. To test the null hypothesis, we used the Two-sample t-test with a significance level of 5% (see also Section 3.1 for an illustration of our approach).

2.3.2. Spectral stacking

Another approach was to take all the spectra from a given terrain of one swirl and stack (sum) them. This created one representative spectrum of the terrain (an alternative to an average spectrum), which was of better quality than each of the previous spectra, as the noise was subdued.

We then fitted the four stacked spectra (of four terrains) for each swirl with MGM, and compared the output parameters.

2.3.3. Principal Component Analysis

The third approach was based on the Principal Component Analysis (PCA), which is a linear transformation that reduces the dimensionality of a problem (Connolly and VanderPlas, 2014). In our case, 83 reflectance values for several hundreds of spectra (n), created an 83 × n-dimensional space (cloud of points). PCA takes this cloud and rotates its axes to get the maximum variance in the data explained by a smaller number of variables than the original 83. These new variables are called the principal components. The first principal component (PC1) usually explains the maximum variance given by the overall shape of the data cloud. Orthogonal to the PC1 and in a direction of the biggest variance that remained in the data lies the second principal component (PC2). Higher order principal components explain finer structures in the data up to the residual noise. PCA therefore separates valuable information into the first few components.

We still have to bear in mind that PCA is a mathematical apparatus enabled mainly by matrix operations (for example see Jolliffe, 2002, for more details). The results we obtain by this method have therefore rather abstract meaning. It is not always[5] possible to assign a specific physical variable to the given principal component and vice versa. Nevertheless, PCA is useful to reveal significant trends in the data. An illustration can be a robust asteroid taxonomy, based on the relative positions in the principal-component space, see (DeMeo et al., 2009).

Before entering the data into the PCA, we divided the values from each spectral band by their variance (in accordance with Connolly and VanderPlas, 2014), to make sure that the variations in the data are comparable. For the PCA, we subtracted the mean from all the data in a given spectral band.

PCA on whole regions of lunar swirls, without distinction of the different terrains, had already been applied by Kramer et al. (2011a).

[4] Albedo was evaluated from non-normalized spectra at 1500 nm.

[5] In case of asteroid families, PC1 correlates significantly with the average spectral slope, and thus with the age of the family (Nesvorný et al., 2005).

3. Results

3.1. Results of histogram plots and spectral stacking

Applying the methods from Section 2.3.1, we got three histograms for each swirl (for distributions of the albedo A, slope s, and strength of the 1000-nm band S_{1000} in different terrains), see Fig. 3 for an example, and the Online Supplementary Material, Figs. S8 to S10 for the rest of the histograms.

Based on the procedure described in Section 2.3.2, we created the stacked spectra. See Fig. 4 for all the stacked spectra from all our swirls.

Based on histograms (Fig. 3 and S8 to S10), we noticed that for some swirls the *mature in* material had a mean value in between the fresh material and *mature out* material. This supported our hypothesis about the intermediate behavior of the *mature in* terrain (see end of Section 1). In other cases, the swirl material (*fresh in* and *mature in*) and the non-swirl material (*fresh out* and *mature out*) clustered together. We also observed these trends in the data from the stacking method. See Table 1 for an overview of the results of the null-hypothesis testing (Section 2.3.1) for both histograms and stacking methods. In the table, "✓" means that the null hypothesis was rejected and there was a clear sequence of mean values: *fresh in, fresh out* → *mature in* → *mature out*, agreeing with our central hypothesis. Usually, it was enough to test only one mean-value pair of distributions/terrains, as the rest of the pairs in the histogram were clearly and significantly ordered. This situation is depicted in Fig. 3 (left). The "×" symbol represents rejection of the null hypothesis in cases where the sequence of the mean values was unambiguous but did not follow our theory, such as the situation in Fig. 3 (right). When the null hypothesis could not be rejected, at the 5% significance level, the table shows "○". We notice several things based on the table:

Albedo: The highland swirls followed our theory of intermediate behavior for albedo, whereas in the mare swirls, the *mature in* terrain had higher albedo than the *fresh out* material.

Slope: We noticed that in case of slope, swirls that are found at the nearside of the Moon (Reiner Gamma, Rima Sirsalis, Airy, and Descartes) followed the null hypothesis, whereas the far-side swirls (Mare Ingenii and Gerasimovich) did not.

Strength: Based on the histogram results, the strength of the 1000-nm band had an inverse behavior to that described for albedo – the highland swirls did not follow the theory, but mare swirls did. The stacking results were rather insignificant in this parameter.

We also note that the Descartes swirl had an unreliably shallow 1000-nm band, if any (see Fig. 4). Therefore, we did not fit it.

Fig. 5 shows the output spectral parameters of stacked spectra with emphasis on their evolution (fresh to mature state). Based on this figure, we noticed that as material evolved from a fresh state to the weathered one, different swirls had distinct inclinations in the graph, but all were in accordance with an overall trend of decreasing albedo and depth[6] of the 1000-nm band, and increasing spectral slope. We could also see that the trend's inclination for materials inside the swirl was usually different from the trend's inclination of the materials outside it. Two observations against the usual behavior were small albedo change in the Rima Sirsalis' case and inverse behavior of the spectral slope of the Gerasimovich swirl.

3.2. Results of Principal Component Analysis

We performed the PCA (Section 2.3.3) separately for each swirl. The resulting plots, depicting the first and second principal component, can

[6] Numerical value of the strength is increasing, which means that the depth of the band is decreasing.

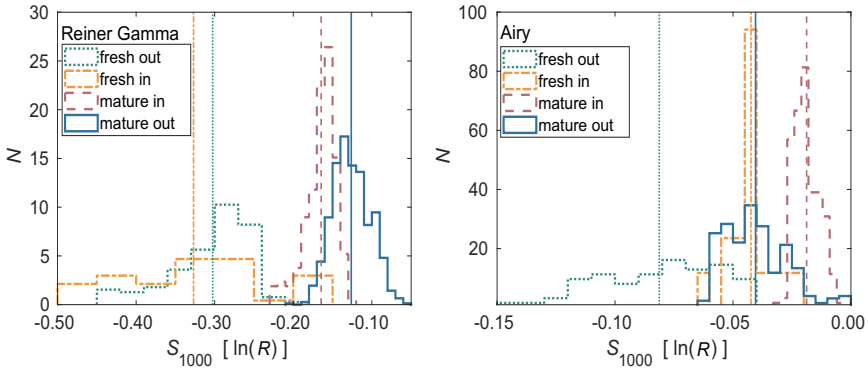

Fig. 3. An example of histograms. The left part of this figure shows a histogram of the strength of the 1000-nm band S_{1000} for the Reiner Gamma swirl. The right part is for the Airy swirl. *N* is the number of occurrences and vertical lines represent mean values. See the Online Supplementary Material, Figs. S8 to S10, for the rest of the histograms.

be found in Fig. 6. This figure also shows, for each swirl, four additional points, which represent the swirl's stacked spectra. We calculated their position in the principal-component space after the main PCA run.

Looking at Fig. 6, we noticed that the *mature out* material could always be distinguished from the other three terrains. Whereas the *mature in* material had variable positions with reference to the fresh materials. As we expected, the *fresh in* and *fresh out* terrains usually occupied the same region of the principal component space. Additional points from stacking usually lay in the middle of the statistical cloud corresponding to the same terrain.

We also computed the PCA for all the swirls together. Spectra belonging to one terrain were represented by the same marker. The final graph, Fig. 7, supported the previous result: the *mature out* terrain was distinct from the other terrains. This result is thus generally valid.

Fig. 8 is based on the PCA calculated only for: (a) mare swirls and (b) highland swirls. Similar figure comparing PCA for near- and far-side swirls is attached in the Online Supplementary Material (Fig. S11).

Further, we tried to evaluate correlations of individual principal components with spectral parameters, which we obtained from MGM. We found that each principal component is strongly correlated (correlation coefficient > 0.8) with more than two spectral parameters. Therefore, we did not present these results here, as they do not give any straightforward interpretation.

4. Discussion

4.1. Interpretation of space weathering trends based on PCA

The position of the *mature in* material in PC1 vs PC2 plots indicates that the swirl material is not fresh in the same way as the crater (*fresh in* and *fresh out*) material. This supports the hypothesis proposed by Pieters and Noble (2016) that the swirl material is distinct from bright soils in craters. One reason could be that the micrometeoroid impacts (presumably unaffected by the magnetic field) weather swirl material but it remains distinct from the *mature out* material, which is also intensively weathered by the solar wind that influences spectra on much shorter timescales (see Section 1.1).

We point out that lunar swirls are believed to be ≈3.8 Gyr old, thus micrometeoroid impacts should have already weathered their spectra even if they were the only agent influencing the space weathering state in the swirls (Blewett et al., 2011, and references therein), but they did not. This may point to some later alteration of the areas that would accompany the magnetic field shielding, for example deposition of fresh or bright material by electrostatic levitation or by nearby cratering events in later stages of swirls' evolution. Such idea has already been proposed for example by Hood et al. (1979b). Alternatively, the micrometeoroid impacts may influence the spectra in lunar swirls on longer timescales or differently than we have previously thought. As Trang and Lucey (2019) showed, lunar swirls are depleted in nanophase iron, but they obtain the same amount of microphase iron[7] as the rest of the area. Micrometeoroid impacts are expected to produce both, nano- and microphase iron particles (Trang and Lucey, 2019, and references therein). The relatively lower abundance of nanophase iron inside lunar swirls thus further points to the different behavior of micrometeoroid impacts in these areas. Another option – the cometary hypothesis is not very probable reason for the spectral dichotomy of the swirls because of the low probability of cometary impacts being distributed according to positions of maria and highlands and because of the near-/far-side dichotomy we discovered in the slope behavior (results of the histogram and stacking methods).

We are only showing PC1 vs PC2 plots in this article, because combinations of higher principal components did not give any significant results, due to their low variance. Still, our PCA results are very robust, because we verified that the conclusions are not sensitive to preprocessing of the spectra, or the data and quality reduction. The analysis had the same conclusions even when applied to:

- non-normalized spectra,
- spectra with subtracted continuum,
- smaller sample of spectra in each terrain,
- equivalent amounts of spectra in each terrain/swirl,
- spectra constrained to a smaller wavelength range (700–1500 nm) – see the Online Supplementary Material, Fig. S12, for an example plot,
- or output spectral parameters from our MGM routine; instead of directly inputting spectra to the PCA.

Points belonging to one terrain are sometimes divided into several clouds in principal component plots. This fact can be attributed to the selection of the data – spectra associated with one terrain originate from diverse areas over the swirl rather than from a continuous region. Also different albedo of individual swirls may play some role in case of PCAs on multiple swirls.

Some of the overlapping points that disturb the pure separation of the *mature out* material (for example in Fig. 6) can be caused by an incorrect classification of the terrains, but the overall clustering is evident even with these points.

[7] Trang and Lucey(2019) divided metallic iron particles into two groups: (1) those larger than 100 nm called microphase iron and (2) smaller than 100 nm called nanophase iron.

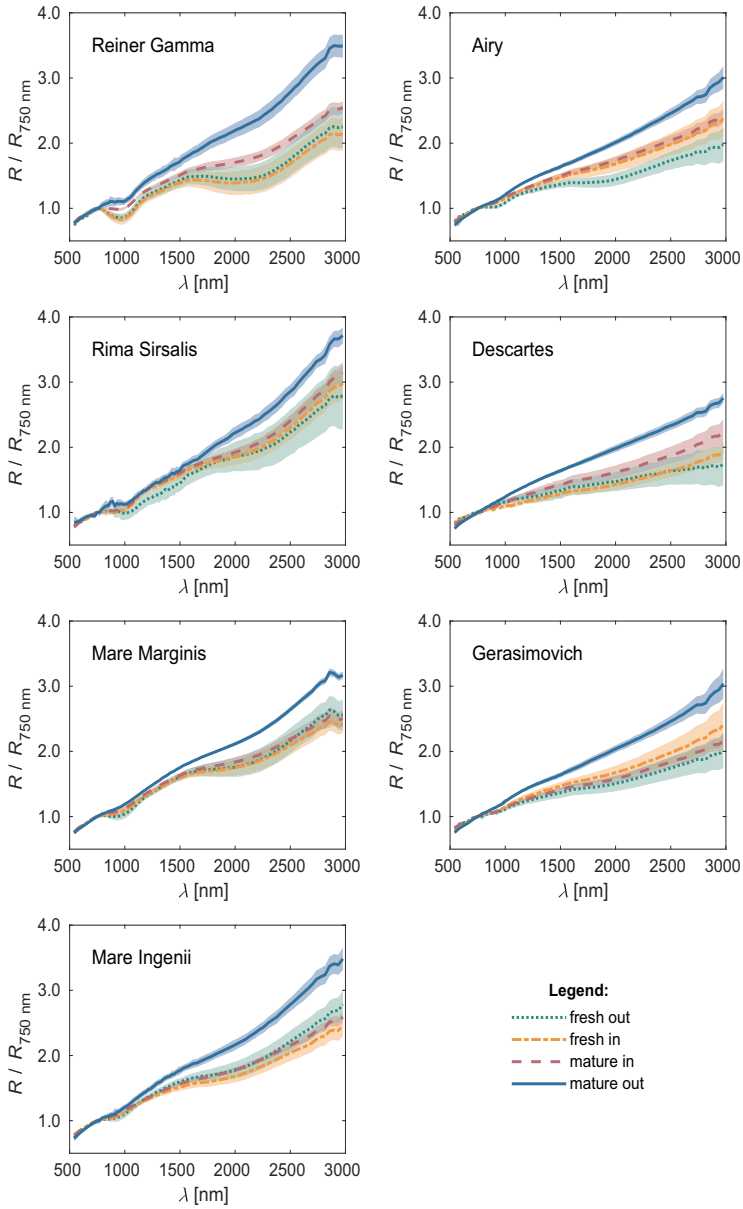

Fig. 4. Spectra of four distinct terrains in the swirls used in this work. Each line shows one representative stacked spectrum from the given terrain in the swirl. A lighter-coloured area around each line marks the one-sigma dispersion of the statistical data from which the stacked spectrum was created.

4.2. Interpretation of the mare/highland dichotomy

Table 1 shows that there is a mare/highland dichotomy in the behavior of the albedo and strength of the 1000-nm band (also Figs. S8 and S10). Mare swirls showed (Fig. S8) that the albedo when influenced predominantly by micrometeoroid impacts does not change in the same extent as if influenced by all the space weathering mechanisms. On the other hand, depth of the 1000-nm band was consistent with our null hypothesis, thus lunar swirls seemed to be in some intermediate state between fresh and mature. In highlands, the albedo behaved accordingly to our null hypothesis, but the 1000-nm band strength did not.

The principal-component plots in Fig. 6 also revealed a difference between the mare and highland swirls. The mare swirls exhibited the point-cloud's orientation dependent on both PC1 and PC2, whereas the highland-swirls' terrains did not seem to vary in PC2.

The Descartes swirl appeared intermediate, as it was also dependent on PC2, see Fig. 6. It is possible that this “non-highland” behavior is caused by the absence of the 1000-nm band, which we mentioned already in Section 2.2. Another possibility is that the Descartes swirl is not a proper type swirl, but rather crater material from two nearby craters, as previously suggested by Blewett et al. (2005). This idea could also be supported by the significant overlap of the *mature in* and *fresh in, fresh out* materials in the graph. On the other hand, Garrick-Bethell et al., (2011) showed that the spectral properties of the region are unlikely only due to craters but may be a result of the magnetic anomaly under the region. We again identified a difference in the

Table 1
Behavior of the three main spectral parameters (albedo *A*, spectral slope *s*, and strength of the 1000-nm band S_{1000}). When the mean of the swirl (*mature in*) material lies unambiguously between the *mature out* and *fresh in, fresh out* materials, "✓" (rejection of the null hypothesis) appears in the table, as in Fig. 3 (left); if the mean values' sequence is unambiguous but the swirl material does not behave intermediately, the situation is marked by "×", see Fig. 3 (right). When the null hypothesis could not be rejected, at the 5% significance level, "○" is shown in the table. Descartes did not show substantial 1000-nm band, the table thus shows "–" for this parameter. In each column, the left symbol represents the result of histogram method, the right one characterizes stacking method's results. The location column shows whether the swirl is at the near- (N) or far-side (F) or at the edge (E) of the Moon, for more precise positions of individual swirls, see the Online Supplementary Material, Table S1.

swirl	type	location	*A*	*s*	S_{1000}
Reiner Gamma	mare	N	× ×	✓ ✓	✓ ✓
Rima Sirsalis		N	× ×	✓ ✓	○ ○
Mare Marginis		E	× ×	○ ×	✓ ✓
Mare Ingenii		F	× ×	× ×	✓ ○
Airy	highland	N	✓ ✓	✓ ✓	× ○
Descartes		N	✓ ○	✓ ✓	– –
Gerasimovich		F	○ ○	× ×	× ○

the table we see that mare swirls have higher FeO content than highland swirls. One could thus say that the reason for mare/highland dichotomy is the different composition of the underlying material. Still, there is a bigger difference between individual mare swirls than between lowest mare swirl and highest highland swirl. Despite the big variation in FeO content in maria (11.5 wt%), the mare swirls behave consistently, e.g. in PCA plots, and there is a bigger difference between highlands and maria, with smaller contrast of FeO content (3.3 wt%). We thus think that there may be some additional effect influencing spectral characteristics of swirls or that there is some threshold value of FeO content that matches the dividing line between lowest mare and highest highland swirls and causes the dichotomy. Sim and Kim (2018) also observed different behavior of mare and highland craters during their analysis of Kaguya's data. Similarly, they associated trends in their dataset to varying iron content.

To find other possible causes of the mare/highland differences, we also briefly tried to compare our data to other parameters such as the altitudes of the swirls, homogeneity of the gravitational and magnetic field, magnetic field amplitude, etc., but we did not detect any correlations with them. The surface roughness distributions obtained from Mini-RF measurements of circular polarization ratio (Nozette et al., 2010) had a similar shape for all the swirls areas we used, see the Online Supplementary Material, Fig. S13. We noticed only a slight shift of the highland swirls towards higher circular polarization ratios, but not all the swirls were fully covered by the measurements. Our results of the surface roughness distributions agreed with those of Neish et al. (2011).

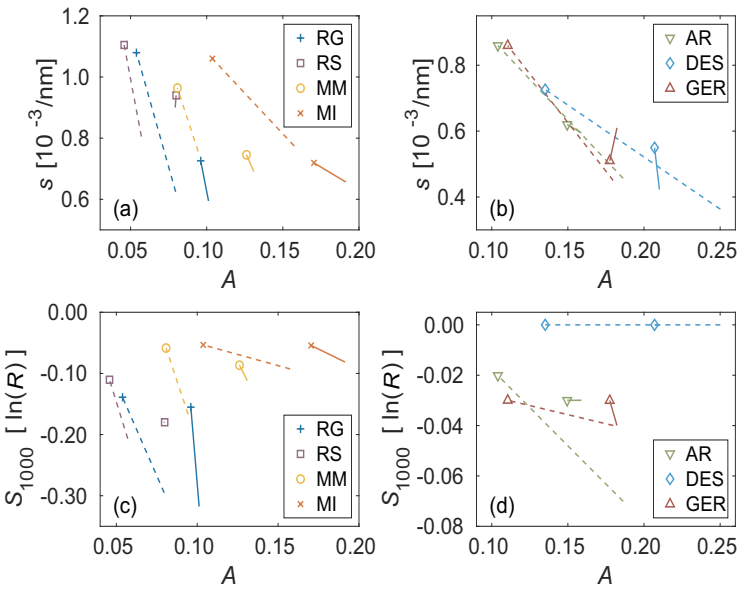

Fig. 5. The albedo *A* vs slope *s* of the (a) mare swirls, (b) highland swirls, and the albedo *A* vs strength of the 1000-nm band S_{1000} of the (c) mare swirls and (d) highland swirls. RG, RS, MM, MI, AR, DES, and GER stand for Reiner Gamma, Rima Sirsalis, Mare Marginis, Mare Ingenii, Airy, Descartes, and Gerasimovich respectively. For each swirl, there are two lines. The trend marked by a solid line represents in-swirl terrains (*fresh in, mature in*), the dashed line is for the trend outside the swirl (*fresh out, mature out* terrains). A symbol at one end of each line marks the more weathered state of that area (the dashed line goes from the fresh crater material outside the swirl (*fresh out*), to the old weathered material outside the swirl (*mature out*), marked by the symbol). The continuum was fitted in a wavelength space.

behavior of the mare and highland swirls in Fig. 8. The data from the Descartes swirl adapted to the highland-like behavior in this figure.

One reason for the difference between the mare and highland swirls can be different iron abundances in these areas (Lawrence et al., 2002), which influence the possibility of creating $npFe^0$ particles, thus the space-weathering final products. We used data from the Lunar Prospector Gamma Ray Spectrometer[8] (Prettyman et al., 2006) and estimated mean values of FeO content in the areas we used in this study, see Table 2. We divided the swirls into three groups based on their iron content: 0–7 wt% of FeO were swirls with low (L) FeO content, 7–14 wt % medium (M) FeO swirls, and > 14 wt% were swirls with high (H) content of FeO. We also verified that the distribution we obtained was in accordance with classification we would get based on the UVVIS FeO abundance from the Clementine probe data (Lucey et al., 2000). From

The mare/highland dichotomy also indicates that the origin of magnetization of the swirl area may be irrelevant to the rest of the evolution of the swirl. The Reiner Gamma swirl is not antipodal to any large impact basin, still it follows the same behavior as the Mare Ingenii and Marginis swirls, which are antipodal. Even if the mechanism creating swirls was different from the antipodal hypothesis, it would not explain the differences between maria and highlands.

Our results suggested that the albedo of the *mature in* material is higher than that of the *fresh out* terrains in mare regions, see the Online Supplementary Material, Fig. S8. A logical explanation would be that maria are usually darker than highlands. Therefore, the background

[8] http://pds-geosciences.wustl.edu/missions/lunarp/grs_elem_abundance.html

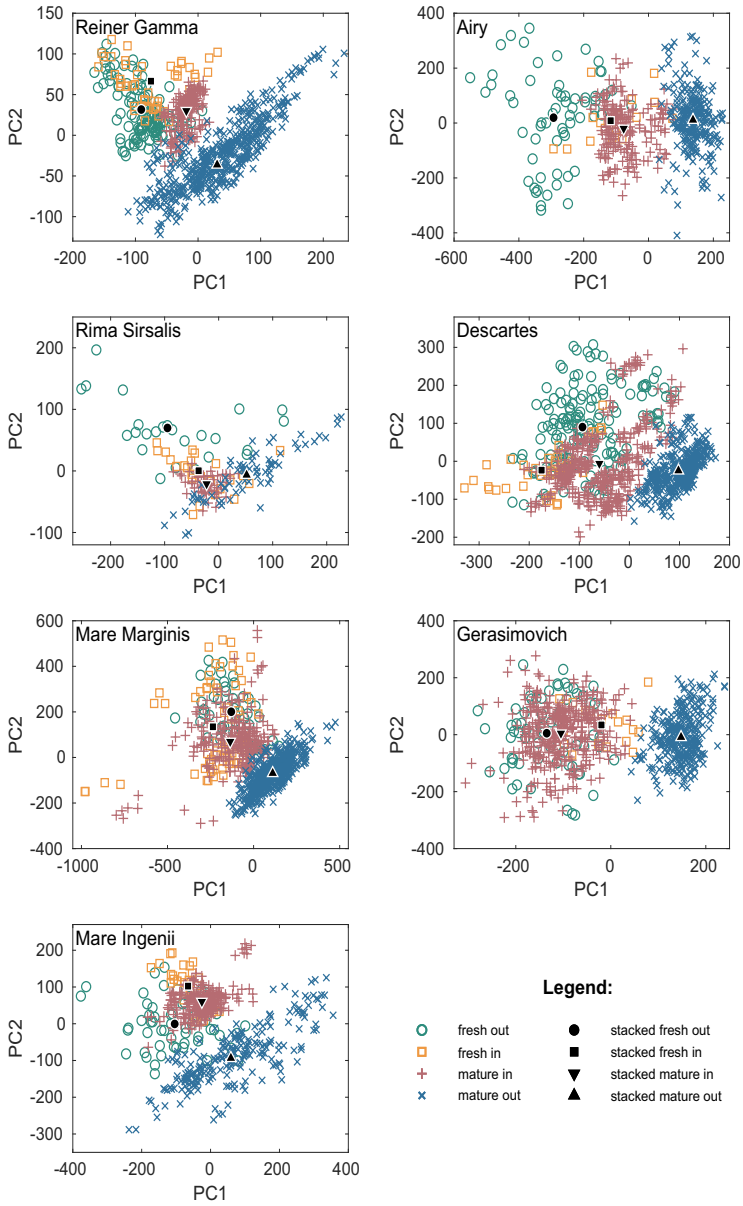

Fig. 6. A plot of the first (PC1) and second (PC2) principal component for different swirls. Black symbols represent the stacked spectra added to the statistical results.

material can diminish the non-swirl crater's albedo. Ono et al. (2009) showed, based on the Kaguya spacecraft's images, that lunar maria exhibit layered structure with depth, which can imply different mineralogies and thus different albedos of crater material compared to the surface material. Highlands are expected to be more homogeneous in this respect. Bright swirl material can also be thicker than crater material and thus support the brightness of the swirl's craters.

4.3. Interpretation of the near-/far-side dichotomy

Spectral slope did not show dichotomic behavior with respect to maria and highlands, but with respect to the near- and far-side. The Mare Marginis is on the very edge of the near side of the Moon, thus follows rather the far-side trend. The near-/far-side dichotomy can be due to the fact that near-side swirls are most exposed to the solar wind when the lunar orbit goes through the Earth's magnetotail. In contrast, far-side swirls are irradiated mainly when the Moon is outside the magnetotail. This result correlates with Trang and Lucey (2019), who claim that the magnetotail crossing is connected to a decreased production of nanophase iron particles due to lower solar wind flux.

The principal-component plots did not highlight the near-/far-side dichotomy as significantly as in the case of mare/highland dichotomy.

4.4. Comments on the statistical results

Inconclusive results appeared most often for the 1000-nm band strengths. We identified two possible reasons for this. The first may be that the results are based on a real physical phenomenon, where the

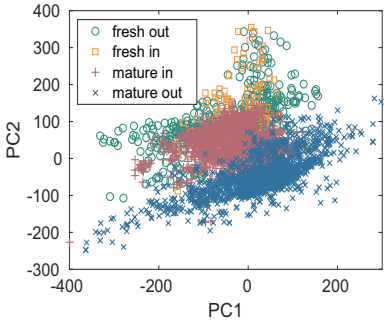

Fig. 7. A plot of the first (PC1) and second (PC2) principal component for all the swirls examined in this work. The terrains of one type have the same symbol for all the swirls.

Table 2
FeO content, in weight percent (wt%), for all seven areas of lunar swirls in this study. H = high FeO content (> 14 wt%), M = medium content (7–14 wt%), and L = low FeO content (< 7 wt%). Last column shows a rough estimate of the surface area of the swirl from which we estimated the FeO content.

swirl	FeO [wt%]	group	type	area [km^2]
Reiner Gamma	20.5	H	mare	3240
Rima Sirsalis	18.0	H	mare	680
Mare Marginis	11.5	M	mare	3660
Mare Ingenii	9.0	M	mare	4730
Airy	5.7	L	highland	4430
Descartes	5.3	L	highland	2520
Gerasimovich	2.8	L	highland	4540

mature in material really has very similar strengths of this band as either the *mature out* or fresh material. The second possibility is that the insignificance is caused by a poor description of the continuum that introduced low-order errors in the estimates of the strengths.

The Rima Sirsalis swirl's results were based on a much lower amount of data (see Section 2.1), as the swirl is small and it was difficult to find the *fresh in* and *fresh out* material in and around it. We are therefore a bit cautious about their significance, but they support our findings in the whole context.

4.5. Interpretation of stacking parameters' evolution

Similar trends to those observed in Fig. 5 had been observed earlier by Gaffey, (2010, Fig. 4). Hemingway et al. (2015) also studied the dependence of the band depth on albedo in three lunar swirls. Their results are in agreement with ours – there exists a trend from fresh impact material to darker background soils.

We saw one exception to the normal trend in our analysis: Gerasimovich's swirl material decreased the slope for the more mature material. This result is robust because we are able to see that the slope behaves in this manner even in the original data, see Fig. 4. Maybe, the *fresh out* spectra were incorrectly chosen due to the difficulties in recognizing the fresh terrains and the high variability of geology in highland regions, which is a limiting aspect of this study, as we mentioned already in Section 2.1. Furthermore, the M^3 data do not cover the whole Gerasimovich anomaly, which constrained our choice of the studied region.

The differences in the directions of inside- and outside-swirl weathering trends may be due to distinct weathering mechanisms or stages. Even Kramer et al. (2011a) saw differences between crater characteristics inside and outside swirls. More detailed spectral data from some of the upcoming missions, evaluated on more swirls, could help to uncover these trends.

We also tried to do a similar plot to Fig. 5, but with all the statistical points. This attitude did not uncover any new information, though, so we did not include the plots here.

4.6. The phase angle influence

Several authors have proposed that spectral characteristics are influenced by a viewing geometry (Carvano and Davalos, 2015). As the so-called phase angle (the Sun–target–probe orientation) increases, the albedo and slope increase as well. This phenomenon was observed for example on asteroids (Sanchez et al., 2012).

The M^3 data were subject to photometric correction, introduced by Besse et al. (2013), which corrected the Level 2 images to the standard phase angle of 30°. Although the authors admit that the correction has its simplifications and should be improved in the future, we still find the data appropriate for our research, because the trends we found are valid for each swirl separately (viewed under only one geometry). The same argument has been used by Nettles et al. (2011) for example. They suggested that spectral changes are not only a function of maturity, but local mineralogy also plays some role. Varying inclinations of trends in Fig. 5 can possibly be attributed to the different mineralogies among swirls. But specially in mare swirls, we expect the inside- and outside-swirl material to be the same (see Section 2.1), so the one-swirl data irregularities are probably caused by something else.

5. Conclusions

This work revealed differences between the mare and highland swirls. The mare/highland dichotomy was mainly observed in the plots of the first two principal components. We further noticed these trends

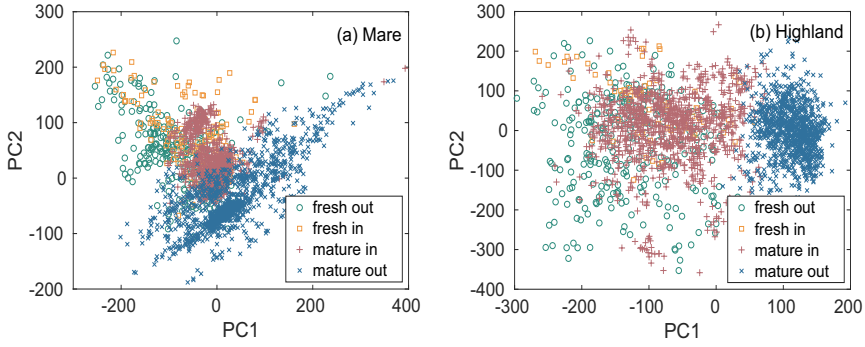

Fig. 8. A plot of the first (PC1) and second (PC2) principal component for (a) all mare swirls (Reiner Gamma, Rima Sirsalis, Mare Marginis, and Mare Ingenii), and (b) all highland swirls (Airy, Descartes, and Gerasimovich) examined in this work. The terrains of one type are plotted with the same symbol for all the swirls.

in the behavior of statistical means and stacked values of albedo and strength of the 1000-nm absorption band. We found that mare swirls have higher FeO content than highland swirls, but this is probably not the only reason for the dichotomy as there are bigger relative differences between individual mare swirls than between mare and highland swirls. The value of FeO content similar to that of lowest-FeO mare swirl or highest-FeO highland swirl used in our analysis may alternatively represent a threshold value causing the different spectral behavior of maria and highlands.

Based on the behavior of the albedo in lunar maria and strength of the 1000-nm band in lunar highlands, we see that the micrometeoroid impacts individually do not reproduce all-combined space weathering effects we observe in the unshielded regions on the Moon.

In addition, we saw the near-/far-side dichotomy in the behavior of the spectral slope, which we prescribed to the fact that the lunar orbit crosses the Earth's magnetotail, which decreases the solar wind income to the near-side swirls. This result strongly favors the solar wind stand-off hypothesis as the reason for the spectral properties of swirls.

Both, the stacking and PCA methods showed that there is a difference in the behavior of the material inside and outside the swirl. We demonstrated that the *mature in* material (swirl material distant from the fresh craters) is distinct from the fresh crater terrains, and that the *mature out* material (mature material outside the swirl formation) can always be distinguished from the other terrains in the principal component space. The behavior of the *mature in* terrain suggests that the solar wind stand-off hypothesis may be combined with a recent deposition of fresh material because micrometeoroid impacts would have weathered the surface of the swirl even without the influence of solar wind in billions years of their existence; or that the influence of micrometeoroids on the evolution of spectral parameters in lunar swirls is smaller or different than previously thought.

In future, we plan to apply our methods to asteroidal spectra, as those are thought to be influenced mainly by the solar wind (Marchi et al., 2006), which is a contrast to lunar swirls that are influenced mostly by micrometeoroid impacts. Therefore, we will be able to compare the two leading effects which cause space weathering.

Acknowledgements

We would like to thank Georgiana Kramer for her help with understanding the M^3 data and lunar spectra. We are also grateful for the comments of Ian Garrick-Bethell and an anonymous reviewer that helped to improve this manuscript.

This work was supported by the University of Helsinki Foundation, Finland and by Academy of Finland, Finland project no. 293975. The work was conducted within institutional support RVO 67985831 of the Institute of Geology of the Czech Academy of Sciences, Czech Republic.

Data availability

Datasets and source codes related to this article can be found at https://doi.org/10.5281/zenodo.1473816, hosted at zenodo.org (Chrbolková et al., 2019).

Appendix A. Online Supplementary Material

Supplementary materials to this article can be found online at https://doi.org/10.1016/j.icarus.2019.05.024.

References

Besse, S., Sunshine, J., Staid, M., Boardman, J., Pieters, C., Guasqui, P., Malaret, E., McLaughlin, S., Yokota, Y., Li, J.-Y., Jan. 2013. A visible and near-infrared photometric correction for Moon Mineralogy Mapper (M^3). Icarus 222, 229–242.

Blewett, D.T., Hawke, B.R., Lucey, P.G., Apr. 2005. Lunar optical maturity investigations: a possible recent impact crater and a magnetic anomaly. J. Geophys. Res. (Planets) 110, E04015.

Blewett, D.T., Coman, E.I., Hawke, B.R., Gillis-Davis, J.J., Purucker, M.E., Hughes, C.G., Feb. 2011. Lunar swirls: examining crustal magnetic anomalies and space weathering trends. J. Geophys. Res. (Planets) 116, E02002.

Burns, R.G., 1970. Mineralogical applications of crystal field theory. In: Electronic Spectra of Transition Metal Ions in Silicate Minerals. Cambridge University Press, Ch, pp. 83.

Burns, R.G., 1989. Spectral mineralogy of terrestrial planets: scanning their surfaces remotely. Mineral. Mag. 53.

Carvano, J.M., Davalos, J.A.G., 2015. Shape and solar phase angle effects on the taxonomic classification of asteroids. Astron. Astrophys. 580, A98.

Chrbolková, K., Kohout, T., Ďurech, J., 2019. Dataset for "Reflectance spectra of seven lunar swirls examined by statistical methods: A space weathering study". Zenodo. https://doi.org/10.5281/zenodo.1473816.

Clark, R.N., Pieters, C.M., Green, R.O., Boardman, J.W., Petro, N.E., Jun. 2011. Thermal removal from near-infrared imaging spectroscopy data of the Moon. J. Geophys. Res. (Planets) 116, E00G16.

Connolly, A.J., VanderPlas, J.T., 2014. Statistics, data mining, and machine learning in astronomy: A practical Python guide for the analysis of survey data. In: Dimensionality and its Reduction. Princeton University Press, Ch, pp. 289–302.

Deca, J., Divin, A., Lue, C., Ahmadi, T., Hornyi, M., 2018. Reiner Gamma albedo features reproduced by modeling solar wind standoff. Communications Physics 1 (1), 12.

DeMeo, F.E., Binzel, R.P., Slivan, S.M., Bus, S.J., Jul. 2009. An extension of the Bus asteroid taxonomy into the near-infrared. Icarus 202, 160–180.

Denevi, B.W., Robinson, M.S., Boyd, A.K., Sato, H., Hapke, B.W., Hawke, B.R., 2014. Characterization of space weathering from Lunar Reconnaissance Orbiter Camera ultraviolet observations of the Moon. J. Geophys. Res. (Planets) 119, 976–997.

Gaffey, M.J., 2010. Space weathering and the interpretation of asteroid reflectance spectra. Icarus 209, 564–574.

Gaffey, M.J., Burbine, T.H., Binzel, R.P., 1993. Asteroid spectroscopy - progress and perspectives. Meteoritics 28, 161–187.

Garrick-Bethell, I., Head, J.W., Pieters, C.M., 2011. Spectral properties, magnetic fields, and dust transport at lunar swirls. Icarus 212, 480–492.

Glotch, T.D., Bandfield, J.L., Lucey, P.G., Hayne, P.O., Greenhagen, B.T., Arnold, J.A., Ghent, R.R., Paige, D.A., Feb. 2015. Formation of lunar swirls by magnetic field standoff of the solar wind. Nat. Commun. 6, 6189.

Green, R.O., Pieters, C., Mouroulis, P., Eastwood, M., Boardman, J., Glavich, T., Isaacson, P., Annadurai, M., Besse, S., Barr, D., Buratti, B., Cate, D., Chatterjee, A., Clark, R., Cheek, L., Combe, J., Dhingra, D., Essandoh, V., Geier, S., Goswami, J.N., Green, R., Haemmerle, V., Head, J., Hovland, L., Hyman, S., Klima, R., Koch, T., Kramer, G., Kumar, A.S.K., Lee, K., Lundeen, S., Malaret, E., McCord, T., McLaughlin, S., Mustard, J., Nettles, J., Petro, N., Plourde, K., Racho, C., Rodriquez, J., Runyon, C., Sellar, G., Smith, C., Sobel, H., Staid, M., Sunshine, J., Taylor, L., Thaisen, K., Tompkins, S., Tseng, H., Vane, G., Varanasi, P., White, M., Wilson, D., Oct. 2011. The Moon Mineralogy Mapper (M^3) imaging spectrometer for lunar science: instrument description, calibration, on-orbit measurements, science data calibration and on-orbit validation. J. Geophys. Res. (Planets) 116, E00G19.

Hapke, B., 2001. Space weathering from Mercury to the asteroid belt. J. Geophys. Res. 106, 10039–10074.

Hemingway, D., Garrick-Bethell, I., 2012. Magnetic field direction and lunar swirl morphology: insights from Airy and Reiner Gamma. J. Geophys. Res. (Planets) 117 (E16), E10012.

Hemingway, D.J., Garrick-Bethell, I., Kreslavsky, M.A., 2015. Latitudinal variation in spectral properties of the lunar maria and implications for space weathering. Icarus 261, 66–79.

Hiroi, T., Abe, M., Kitazato, K., Abe, S., Clark, B.E., Sasaki, S., Ishiguro, M., Barnouin-Jha, O.S., 2006. Developing space weathering on the asteroid 25143 Itokawa. Nature 443, 56–58.

Hood, L.L., Artemieva, N.A., 2008. Antipodal effects of lunar basin-forming impacts: initial 3D simulations and comparisons with observations. Icarus 193, 485–502.

Hood, L.L., Schubert, G., 1980. Lunar magnetic anomalies and surface optical properties. Science 208, 49–51.

Hood, L.L., Williams, C.R., 1989. The lunar swirls - distribution and possible origins. In: Ryder, G., Sharpton, V.L. (Eds.), Lunar and Planetary Science Conference Proceedings. Vol. 19 of Lunar and Planetary Science Conference Proceedings, pp. 99–113.

Hood, L., Coleman, P.J., Wilhelms, D.E., 1979a. The moon - sources of the crustal magnetic anomalies. Science 204, 53–57.

Hood, L.L., Coleman Jr., P.J., Wilhelms, D.E., 1979b. Lunar nearside magnetic anomalies. In: Hinners, N.W. (Ed.), Lunar and Planetary Science Conference Proceedings. Vol. 10 of Lunar and Planetary Science Conference Proceedings, pp. 2235–2257.

Hood, L.L., Zakharian, A., Halekas, J., Mitchell, D.L., Lin, R.P., Acuña, M.H., Binder, A.B., 2001. Initial mapping and interpretation of lunar crustal magnetic anomalies using Lunar Prospector magnetometer data. J. Geophys. Res. 106, 27825–27840.

Ishiguro, M., Hiroi, T., Tholen, D.J., Sasaki, S., Ueda, Y., Nimura, T., Abe, M., Clark, B.E., Yamamoto, A., Yoshida, F., Nakamura, R., Hirata, N., Miyamoto, H., Yokota, Y., Hashimoto, T., Kubota, T., Nakamura, A.M., Gaskell, R.W., Saito, J., 2007. Global mapping of the degree of space weathering on asteroid 25143 Itokawa by Hayabusa/AMICA observations. Meteorit. Planet. Sci. 42, 1791–1800.

Jolliffe, I.T., 2002. Ch. Principal component analysis and factor analysis. In: Principal Component Analysis. Springer-Verlag, New York, pp. 150–166.

Jozwiak, L.M., Blewett, D.T., 2017. Geomorphological Analysis of Lunar Swirls: Insights From LROC-NAC. AGU Fall Meeting Abstracts.

Kelley, M.R., Garrick-Bethell, I., Mar. 2019. Testing the antipodal ejecta magnetization hypothesis: a closer look at the geologic setting of the lunar Gerasimovich magnetic anomalies. In: Lunar and Planetary Science Conference. Vol. 50 of Lunar and Planetary Inst. Technical Report, pp. 2071.

Klima, R.L., Pieters, C.M., Dyar, M.D., 2007. Spectroscopy of synthetic Mg-Fe pyroxenes I:

spin-allowed and spin-forbidden crystal field bands in the visible and near-infrared. Meteorit. Planet. Sci. 42, 235–253.
Kramer, G. Y., Besse, S., Dhingra, D., Nettles, J., Klima, R., Garrick-Bethell, I., Clark, R. N., Combe, J.-P., Head, III, J. W., Taylor, L. A., Pieters, C. M., Boardman, J., McCord, T. B., 2011a. M^3 spectral analysis of lunar swirls and the link between optical maturation and surface hydroxyl formation at magnetic anomalies. J. Geophys. Res. (Planets) 116, E00G18.
Kramer, G.Y., Combe, J.-P., Harnett, E.M., Hawke, B.R., Noble, S.K., Blewett, D.T., McCord, T.B., Giguere, T.A., 2011b. Characterization of lunar swirls at Mare Ingenii: a model for space weathering at magnetic anomalies. J. Geophys. Res. (Planets) 116 (E04008).
Lauretta, D.S., Balram-Knutson, S.S., Beshore, E., Boynton, W.V., Drouet d'Aubigny, C., DellaGiustina, D.N., Enos, H.L., Golish, D.R., Hergenrother, C.W., Howell, E.S., Bennett, C.A., Morton, E.T., Nolan, M.C., Rizk, B., Roper, H.L., Bartels, A.E., Bos, B.J., Dworkin, J.P., Highsmith, D.E., Lorenz, D.A., Lim, L.F., Mink, R., Moreau, M.C., Nuth, J.A., Reuter, D.C., Simon, A.A., Bierhaus, E.B., Bryan, B.H., Ballouz, R., Barnouin, O.S., Binzel, R.P., Bottke, W.F., Hamilton, V.E., Walsh, K.J., Chesley, S.R., Christensen, P.R., Clark, B.E., Connolly, H.C., Crombie, M.K., Daly, M.G., Emery, J.P., McCoy, T.J., McMahon, J.W., Scheeres, D.J., Messenger, S., Nakamura-Messenger, K., Righter, K., Sandford, S.A., 2017. OSIRIS-REx: sample return from asteroid (101955) Bennu. Space Sci. Rev. 212, 925–984.
Lawrence, D.J., Feldman, W.C., Elphic, R.C., Little, R.C., Prettyman, T.H., Maurice, S., Lucey, P.G., Binder, A.B., 2002. Iron abundances on the lunar surface as measured by the Lunar Prospector gamma-ray and neutron spectrometers. J. Geophys. Res. (Planets) 107, 5130.
Lee, J.-K., Maxwell, R., Jin, H., Baek, S.-M., Ghassemi, O., Kelley, M., Lee, H., Kim, K.-H., Lee, S., Garrick-Bethell, I., 2019. A small lunar swirl and its implications for the formation of the Reiner Gamma magnetic anomaly. Icarus 319, 869–884.
Lin, R.P., Mitchell, D.L., Curtis, D.W., Anderson, K.A., Carlson, C.W., McFadden, J., Acuna, M.H., Hood, L.L., Binder, A., Sep. 1998. Lunar surface magnetic fields and their interaction with the solar wind: results from Lunar Prospector. Science 281, 1480.
Lucey, P.G., Blewett, D.T., Jolliff, B.L., 2000. Lunar iron and titanium abundance algorithms based on final processing of Clementine ultraviolet-visible images. J. Geophys. Res. 105, 20297–20306.
Marchi, S., Paolicchi, P., Lazzarin, M., Magrin, S., 2006. A general spectral slope-exposure relation for S-type main belt and near-earth asteroids. Astron. J. 131, 1138–1141.
Matsumoto, T., Tsuchiyama, A., Miyake, A., Noguchi, T., Nakamura, M., Uesugi, K., Takeuchi, A., Suzuki, Y., Nakano, T., 2015. Surface and internal structures of a space-weathered rim of an Itokawa regolith particle. Icarus 257, 230–238.
Mikouchi, T., Komatsu, M., Hagiya, K., Ohsumi, K., Zolensky, M.E., Hoffmann, V., Martinez, J., Hochleitner, R., Kaliwoda, M., Terada, Y., Yagi, N., Takata, M., Satake, W., Aoyagi, Y., Takenouchi, A., Karouji, Y., Uesugi, M., Yada, T., 2014. Mineralogy and crystallography of some Itokawa particles returned by the Hayabusa asteroidal sample return mission. Earth, Planets, and Space 66 (82).
Neish, C.D., Blewett, D.T., Bussey, D.B.J., Lawrence, S.J., Mechtley, M., Thomson, B.J., Mini-RF Team, 2011. The surficial nature of lunar swirls as revealed by the Mini-RF instrument. Icarus 215, 186–196.
Nesvorný, D., Jedicke, R., Whiteley, R.J., Ivezić, Ž., Jan. 2005. Evidence for asteroid space weathering from the Sloan Digital Sky Survey. Icarus 173, 132–152.
Nettles, J.W., Staid, M., Besse, S., Boardman, J., Clark, R.N., Dhingra, D., Isaacson, P., Klima, R., Kramer, G., Pieters, C.M., Taylor, L.A., Jul. 2011. Optical maturity variation in lunar spectra as measured by Moon Mineralogy Mapper data. J. Geophys. Res. (Planets) 116, E00G17.
Noguchi, T., Nakamura, T., Kimura, M., Zolensky, M.E., Tanaka, M., Hashimoto, T., Konno, M., Nakato, A., Ogami, T., Fujimura, A., Abe, M., Yada, T., Mukai, T., Ueno, M., Okada, T., Shirai, K., Ishibashi, Y., Okazaki, R., 2011. Incipient space weathering observed on the surface of Itokawa dust particles. Science 333, 1121.
Nozette, S., Spudis, P., Bussey, B., Jensen, R., Raney, K., Winters, H., Lichtenberg, C.L., Marinelli, W., Crusan, J., Gates, M., Robinson, M., 2010. The Lunar Reconnaissance Orbiter Miniature Radio Frequency (mini-RF) technology demonstration. Space Sci. Rev. 150, 285–302.
Ono, T., Kumamoto, A., Nakagawa, H., Yamaguchi, Y., Oshigami, S., Yamaji, A., Kobayashi, T., Kasahara, Y., Oya, H., 2009. Lunar radar sounder observations of subsurface layers under the nearside Maria of the moon. Science 323, 909.
Pieters, C.M., Noble, S.K., 2016. Space weathering on airless bodies. J. Geophys. Res. (Planets) 121, 1865–1884.
Pieters, C.M., Taylor, L.A., Noble, S.K., Keller, L.P., Hapke, B., Morris, R.V., Allen, C.C., McKay, D.S., Wentworth, S., Sep. 2000. Space weathering on airless bodies: resolving a mystery with lunar samples. Meteorit. Planet. Sci. 35, 1101–1107.
Pinet, P.C., Shevchenko, V.V., Chevrel, S.D., Daydou, Y., Rosemberg, C., 2000. Local and regional lunar regolith characteristics at Reiner Gamma formation: optical and spectroscopic properties from Clementine and Earth-based data. J. Geophys. Res. 105, 9457–9476.
Prettyman, T.H., Hagerty, J.J., Elphic, R.C., Feldman, W.C., Lawrence, D.J., McKinney, G.W., Vaniman, D.T., 2006. Elemental composition of the lunar surface: analysis of gamma ray spectroscopy data from Lunar Prospector. J. Geophys. Res. (Planets) 111 (E10) (E12007).
Sanchez, J.A., Reddy, V., Nathues, A., Cloutis, E.A., Mann, P., Hiesinger, H., 2012. Phase reddening on near-earth asteroids: implications for mineralogical analysis, space weathering and taxonomic classification. Icarus 220, 36–50.
Schultz, P.H., Srnka, L.J., 1980. Cometary collisions on the Moon and Mercury. Nature 284, 22–26.
Shestopalov, D.I., McFadden, L.A., Golubeva, L.F., Orujova, L.O., 2010. About mineral composition of geologic units in the northern hemisphere of Vesta. Icarus 209, 575–585.
Shuai, T., Zhang, X., Zhang, L., Wang, J., 2013. Mapping global lunar abundance of plagioclase, clinopyroxene and olivine with interference imaging spectrometer hyperspectral data considering space weathering effect. Icarus 222, 401–410.
Sim, C.K., Kim, S.S., 2018. Spectral trends of the surface regolith in lunar craters. Journal of Geophysical Research (Planets) 123 (8), 2065–2075.
Sim, C.K., Kim, S.S., Lucey, P.G., Garrick-Bethell, I., Choi, Y.-J., 2017. Asymmetric space weathering on lunar crater walls. Geophys. Res. Lett. 44, 11.
Simon, S.B., Joswiak, D.J., Ishii, H.A., Bradley, J.P., Chi, M., Grossman, L., Aléon, J., Brownlee, D.E., Fallon, S., Hutcheon, I.D., Matrajt, G., McKeegan, K.D., 2008. A refractory inclusion returned by stardust from comet 81P/Wild 2. Meteorit. Planet. Sci. 43, 1861–1877.
Sturges, H.A., 1926. The choice of a class interval. J. Am. Stat. Assoc. 21 (153), 65–66.
Sunshine, J.M., Pieters, C.M., Pratt, S.F., 1990. Deconvolution of mineral absorption bands - an improved approach. J. Geophys. Res. 95, 6955–6966.
Sunshine, J.M., Pieters, C.M., Pratt, S.F., McNaron-Brown, K.S., Mar. 1999. Absorption band modeling in reflectance spectra: availability of the Modified Gaussian Model. In: Lunar and Planetary Science Conference. Lunar and Planetary Inst. Technical Report, vol. 30. pp. 1306.
Syal, M.B., Schultz, P.H., Riner, M.A., 2015. Darkening of Mercury's surface by cometary carbon. Nat. Geosci. 8, 352–356.
Trang, D., Lucey, P.G., 2019. Improved space weathering maps of the lunar surface through radiative transfer modeling of Kaguya multiband imager data. Icarus 321, 307–323.
Tsuda, Y., Yoshikawa, M., Abe, M., Minamino, H., Nakazawa, S., Oct. 2013. System design of the Hayabusa 2–asteroid sample return mission to 1999 JU3. Acta Astronautica 91, 356–362.

Online Supplementary Material

Reflectance Spectra of Seven Lunar Swirls Examined by Statistical Methods: A Space Weathering Study

Kateřina Chrbolková, Tomáš Kohout, Josef Ďurech

Contents

swirl name	input spectral cube	latitude	longitude
Reiner Gamma	m3g20090210t033052	+7.48	-58.91
Rima Sirsalis	m3g20090419t144815	-1.13	-61.06
Mare Marginis	m3g20090602t074711	+14.18	+83.54
Mare Ingenii	m3g20090623t182551	-35.79	-161.80
Airy	m3g20090205t094623	-18.99	+3.56
Descartes	m3g20090204t113444	-10.08	+15.49
Gerasimovich	m3g20090424t085330	-22.99	-123.72

Table S1: A list of input spectral cubes for our analysis. The Moon Mineralogy Mapper's cubes were downloaded from the Planetary Data System, Geosciences Node, `http://ode.rsl.wustl.edu/moon/index.aspx`. Latitude (-90 to +90) and longitude (-180 to +180) mark the position of the center of the swirls' area we used.

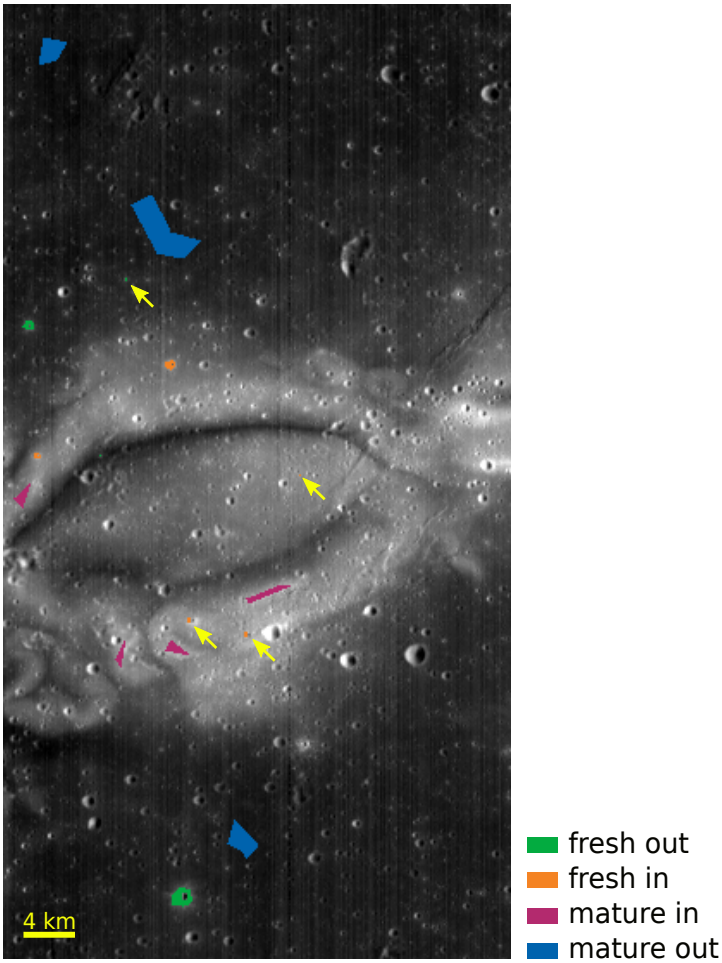

Figure S1: Reiner Gamma swirl (750-nm reflectance image) with highlighted pixels of the Moon Mineralogy Mapper's spectra we used for our analysis. Each terrain has different color (color-coding is consistent throughout the whole article). Groups of only few pixels that are difficult to see were additionally marked by yellow arrows to increase their visibility. All images have adjusted contrast and brightness to enable easier identification of locations of pixels we used. For coordinates of centers of individual images in the mosaic, see Table S1.

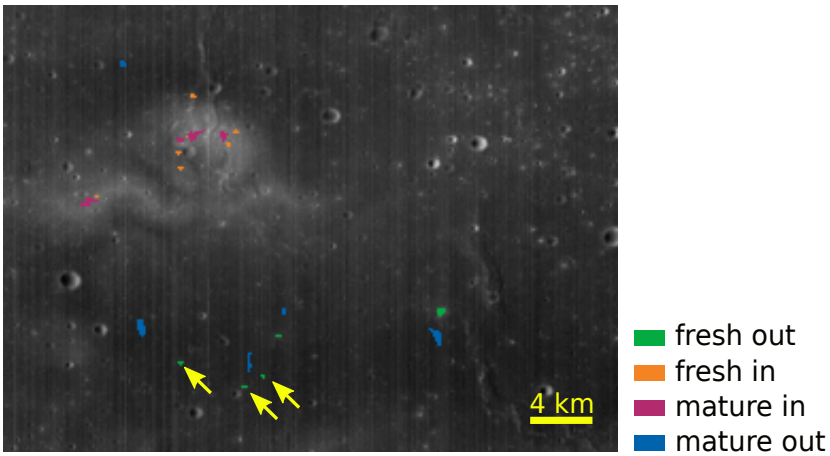

Figure S2: The same as in Figure S1, but for the Rima Sirsalis swirl.

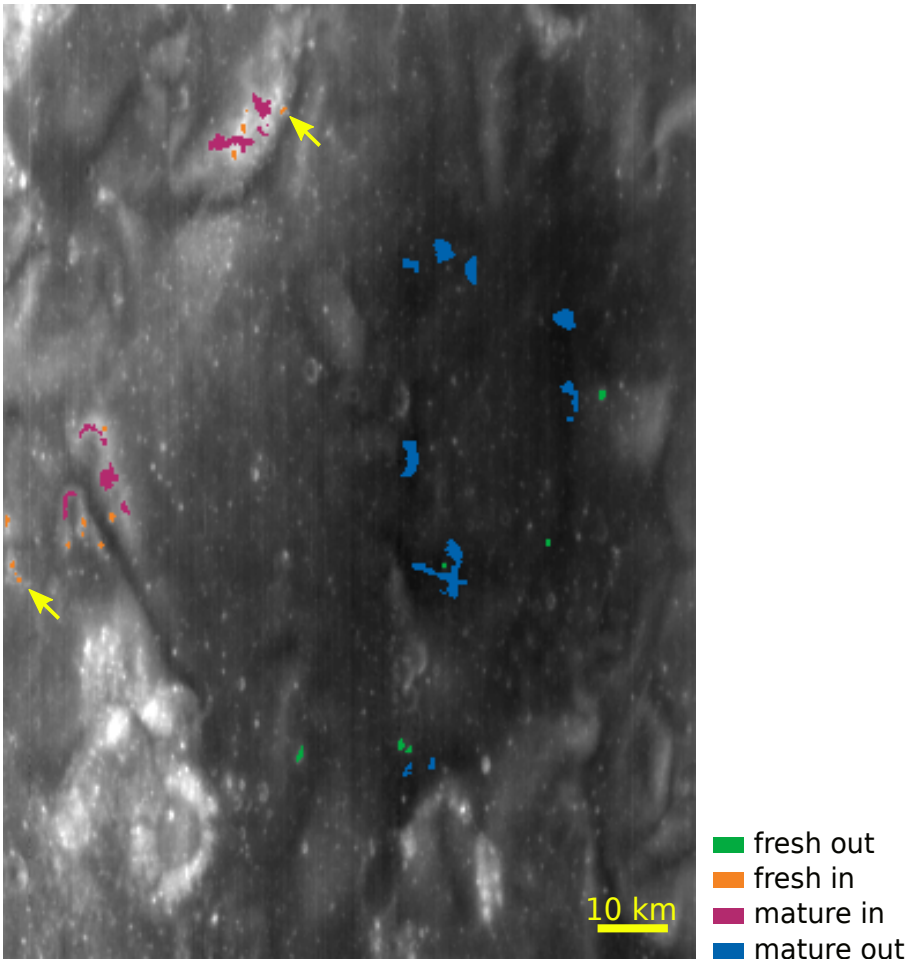

Figure S3: The same as in Figure S1, but for the Mare Marginis swirl.

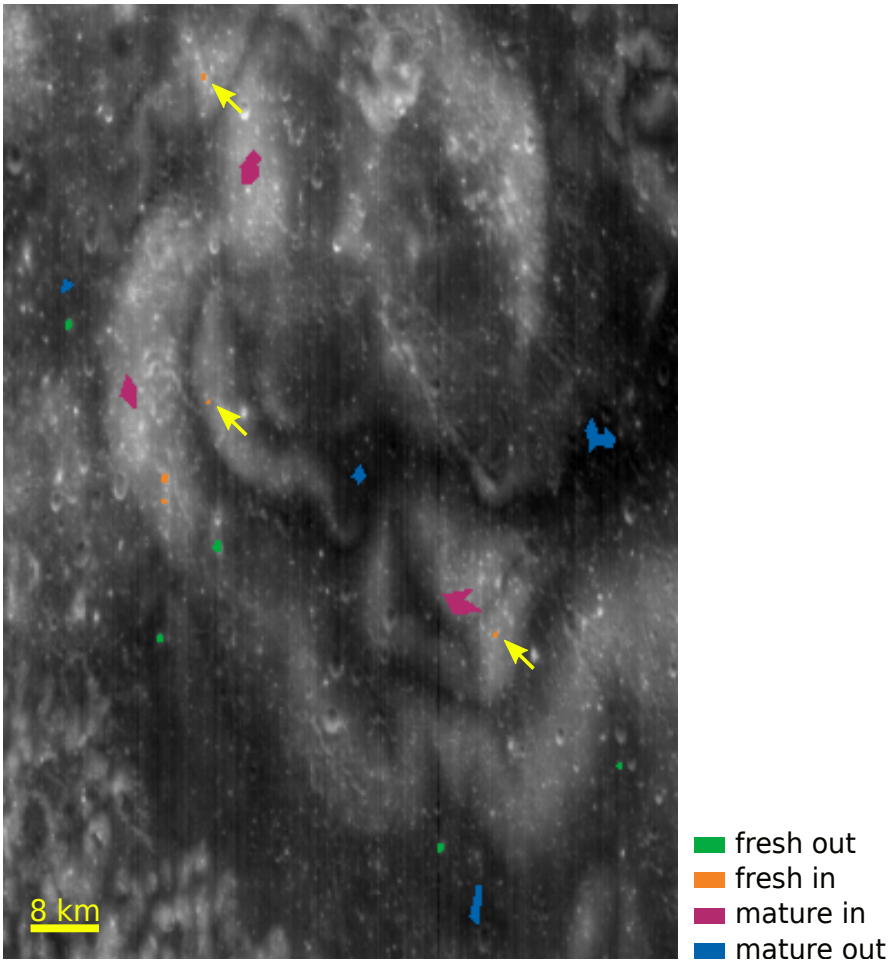

Figure S4: The same as in Figure S1, but for the Mare Ingenii swirl.

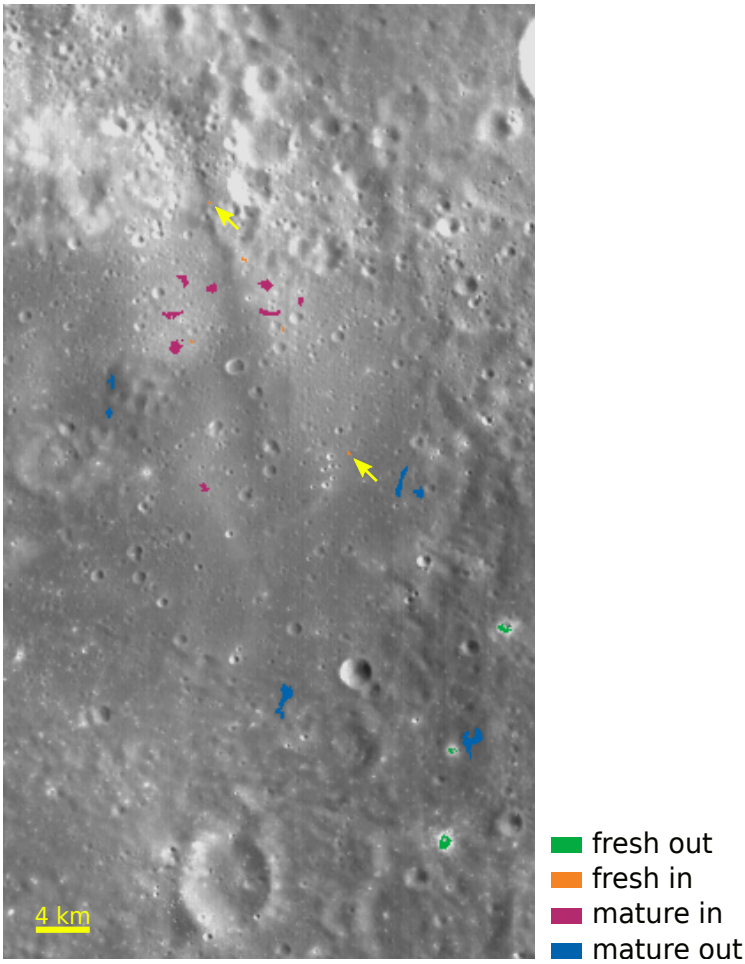

Figure S5: The same as in Figure S1, but for the Airy swirl.

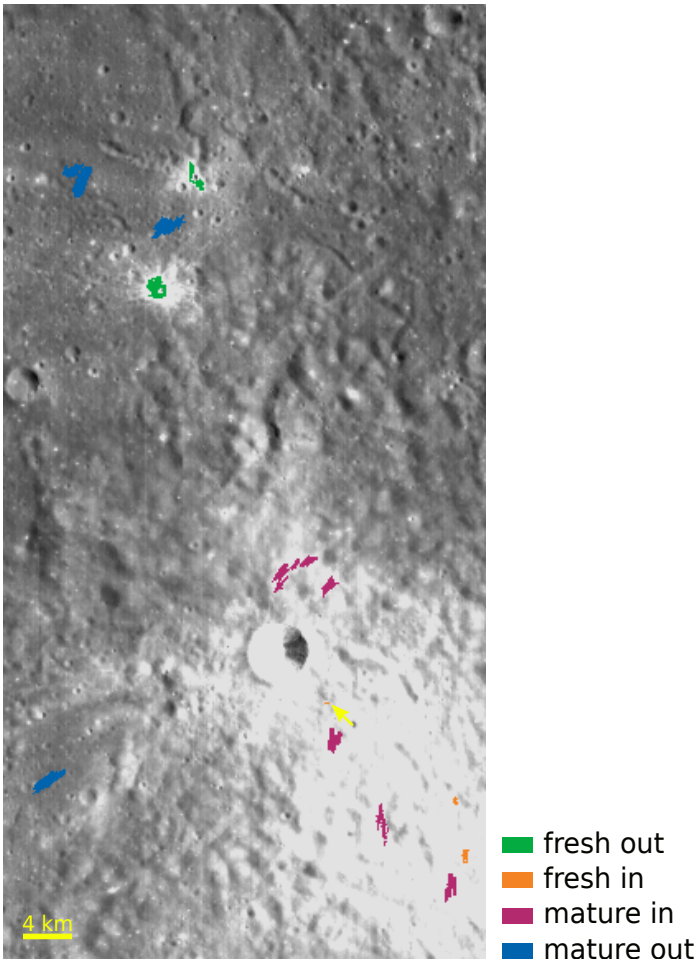

Figure S6: The same as in Figure S1, but for the Descartes swirl.

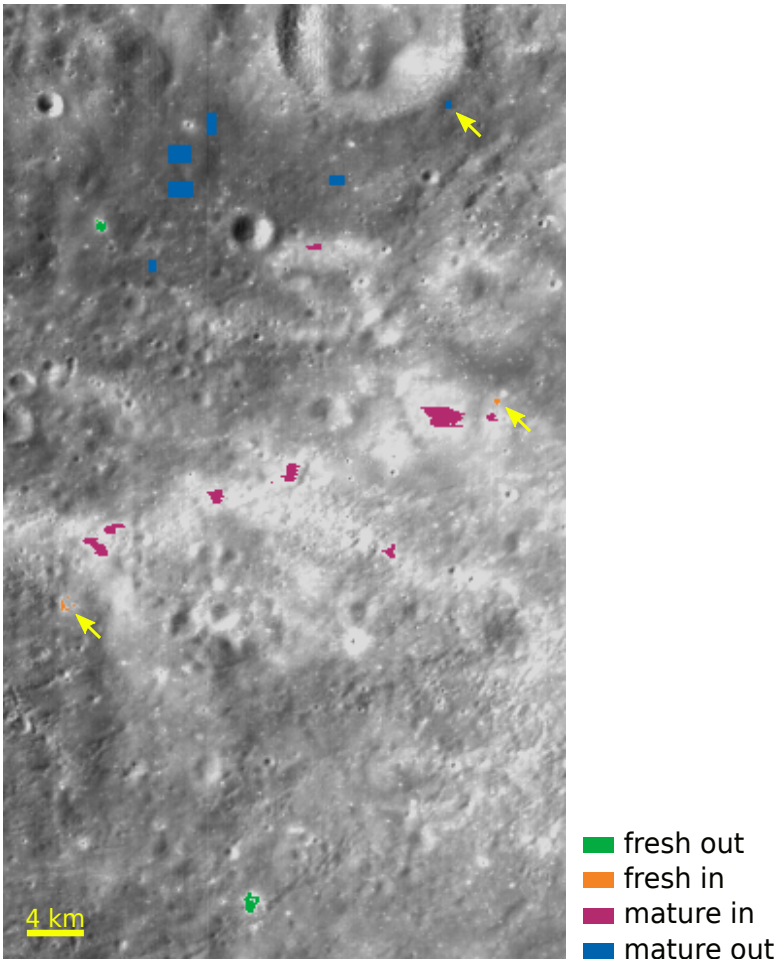

Figure S7: The same as in Figure S1, but for the Gerasimovich swirl.

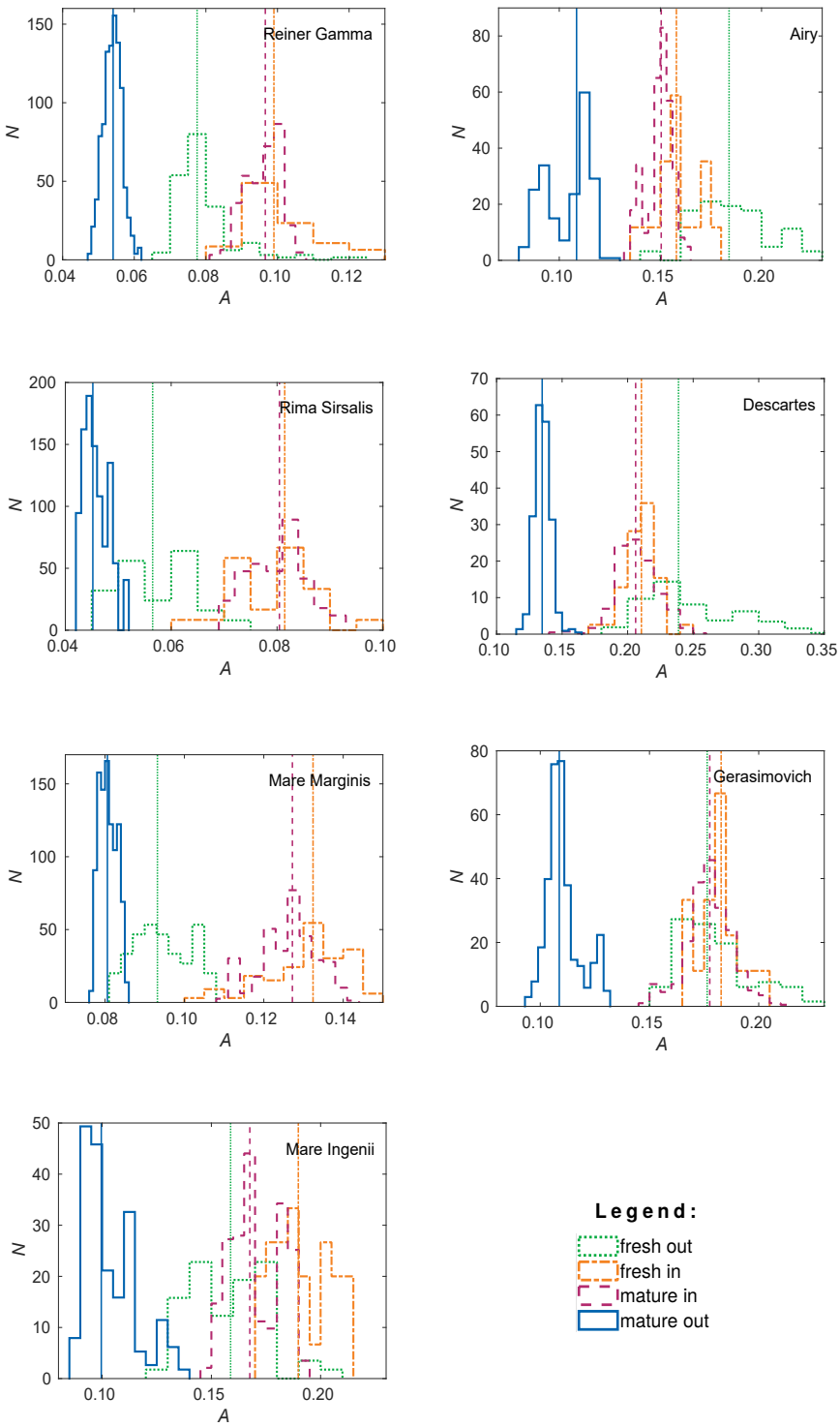

Figure S8: Histogram plots of the albedo, A, at 1500 nm in different terrains of our swirls. N is the number of occurrences, vertical lines represent mean values.

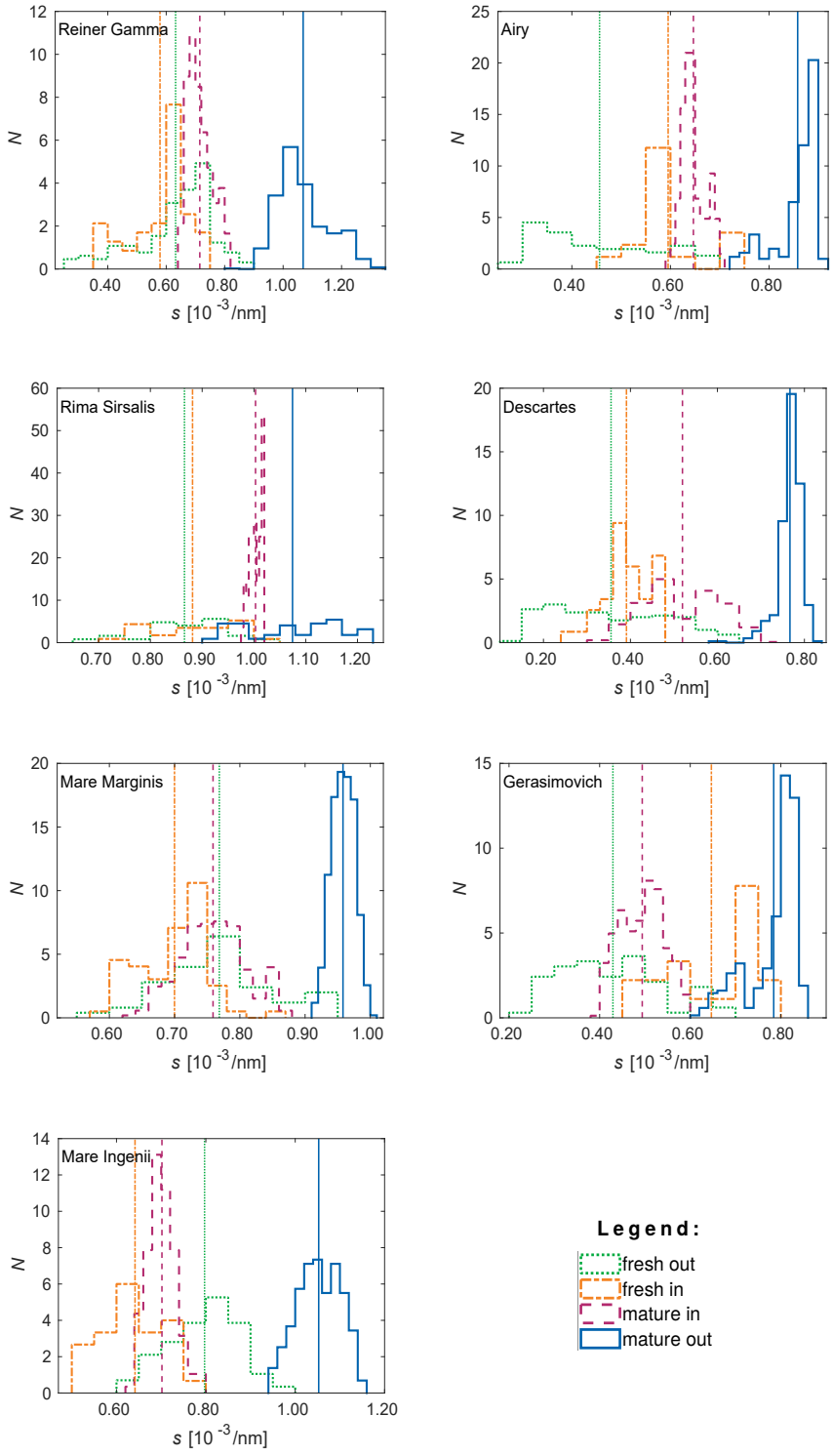

Figure S9: Histogram plots of the spectral slope, s, in different terrains of our swirls. N is the number of occurrences, vertical lines represent mean values.

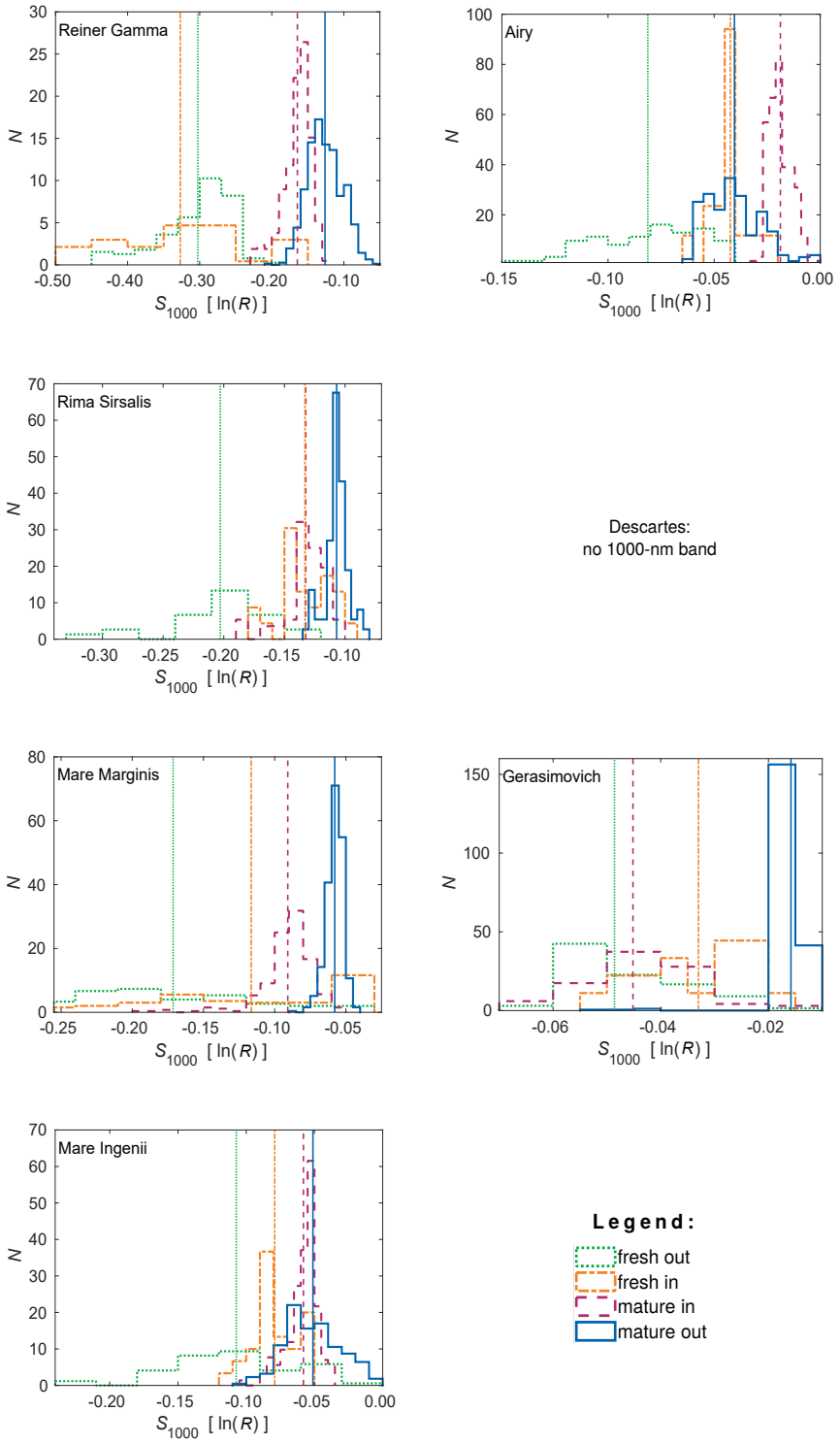

Figure S10: Histogram plots of the strength of the 1000-nm band, S_{1000}, in different terrains of our swirls. N is the number of occurrences, vertical lines represent mean values. The Descartes swirl did not show the 1000-nm band.

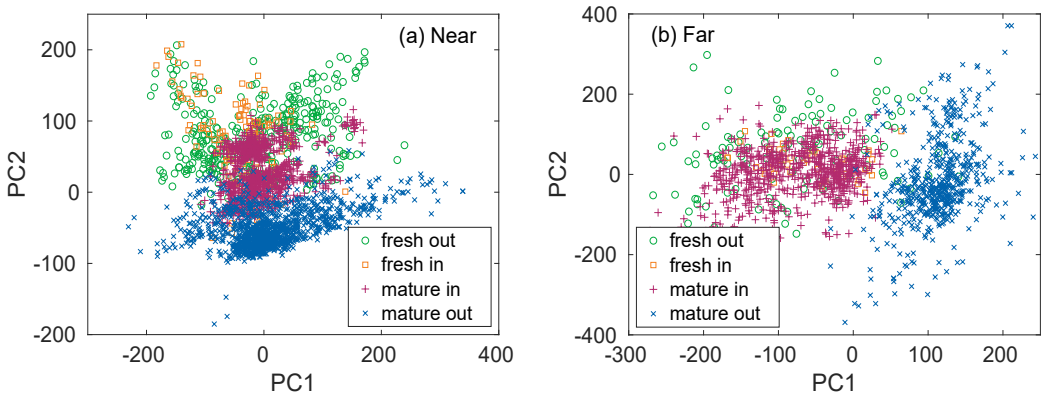

Figure S11: A plot of the first (PC1) and second (PC2) principal component for (a) nearside swirls (Reiner Gamma, Rima Sirsalis, Airy, and Descartes), and (b) far-side swirls (Mare Ingenii and Gerasimovich) examined in this work. The terrains of one type are plotted with the same symbol for all the swirls.

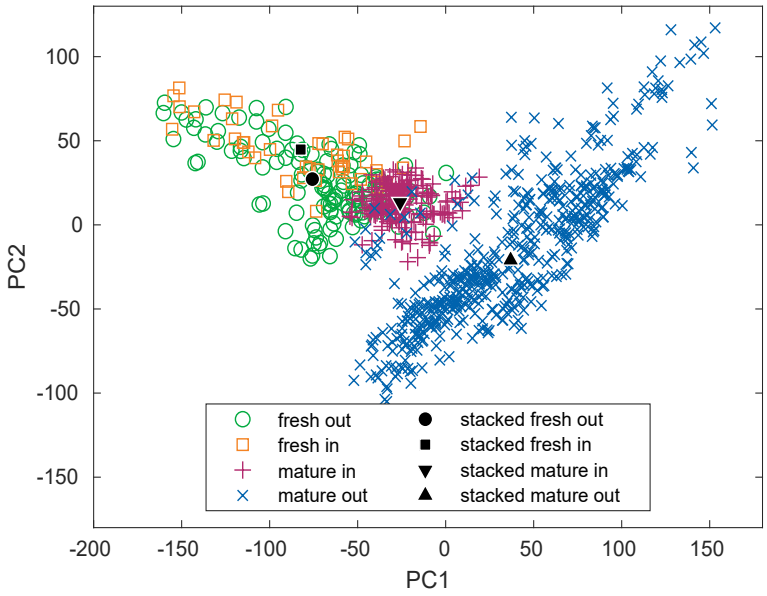

Figure S12: A plot of the first (PC1) and second (PC2) principal component for the spectra of the Reiner Gamma swirl. The spectral wavelength range was constrained to 700 – 1500 nm compared to the analyses in the main article.

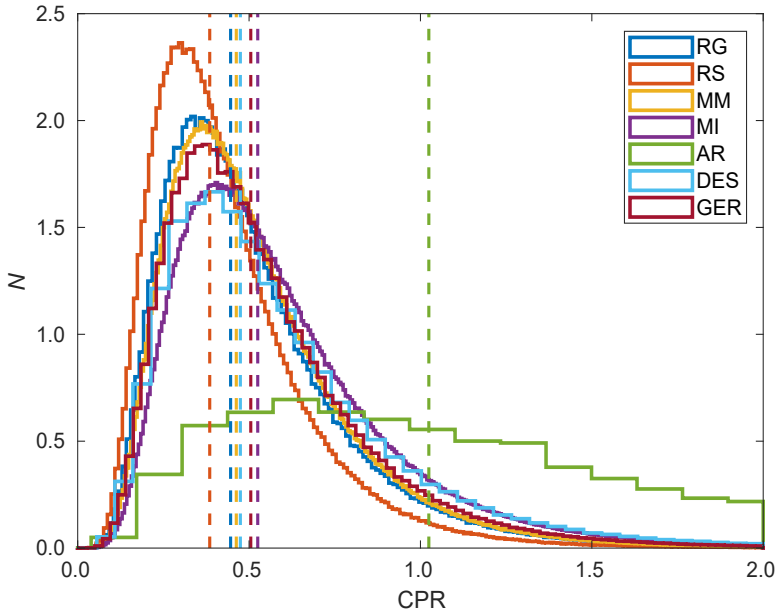

Figure S13: Histogram plot of the circular polarization ratio (CPR) of our seven swirls. Abbreviations RG, RS, MM, MI, AR, DES, and GER stand for the Reiner Gamma, Rima Sirsalis, Mare Marginis, Mare Ingenii, Airy, Descartes, and Gerasimovich swirls respectively. N is the number of counts. Histograms follow the Probability density function normalization. Vertical lines represent medians of the histograms.

Paper II

Chrbolková, K., Brunetto, R., Ďurech, J., Kohout, T., Mizohata, K., Malý, P., Dědič, V., Lantz, C., Penttilä, A., Trojánek, F., and Maturilli, A.

Comparison of space weathering spectral changes induced by solar wind and micrometeoroid impacts using ion- and femtosecond-laser-irradiated olivine and pyroxene.

Astronomy & Astrophysics, 2021, 654, A143.

A&A 654, A143 (2021)
https://doi.org/10.1051/0004-6361/202140372

Astronomy & Astrophysics

Comparison of space weathering spectral changes induced by solar wind and micrometeoroid impacts using ion- and femtosecond-laser-irradiated olivine and pyroxene*

Kateřina Chrbolková[1,2,3], Rosario Brunetto[4], Josef Ďurech[1], Tomáš Kohout[2,3], Kenichiro Mizohata[5], Petr Malý[6], Václav Dědič[7], Cateline Lantz[4], Antti Penttilä[8], František Trojánek[6], and Alessandro Maturilli[9]

[1] Astronomical Institute, Faculty of Mathematics and Physics, Charles University, V Holešovičkách 2, 18000, Prague, Czech Republic
[2] Department of Geosciences and Geography, PO box 64, 00014 University of Helsinki, Finland
e-mail: katerina.chrbolkova@helsinki.fi
[3] Czech Academy of Sciences, Institute of Geology, Rozvojová 269, 16500 Prague, Czech Republic
[4] Université Paris-Saclay, CNRS, Institut d'Astrophysique Spatiale, 91405 Orsay, France
[5] Department of Physics, PO box 43, 00014 University of Helsinki, Finland
[6] Department of Chemical Physics and Optics, Faculty of Mathematics and Physics, Charles University, Ke Karlovu 3, 12116 Prague, Czech Republic
[7] Institute of Physics, Faculty of Mathematics and Physics, Charles University, Ke Karlovu 5, 12116 Prague, Czech Republic
[8] Department of Physics, PO box 64, 00014 University of Helsinki, Finland
[9] Institute of Planetary Research, DLR German Aerospace Centre, Rutherfordstrasse 2, 12489 Berlin, Germany

Received 18 January 2021 / Accepted 7 July 2021

ABSTRACT

Context. Space weathering is a process that changes the surface of airless planetary bodies. Prime space weathering agents are solar wind irradiation and micrometeoroid bombardment. These processes alter planetary reflectance spectra and often modify their compositional diagnostic features.
Aims. In this work we focused on simulating and comparing the spectral changes caused by solar wind irradiation and by micrometeoroid bombardment to gain a better understanding of these individual space weathering processes.
Methods. We used olivine and pyroxene pellets as proxies for planetary materials. To simulate solar wind irradiation we used hydrogen, helium, and argon ions with energies from 5 to 40 keV and fluences of up to 10^{18} particles cm^{-2}. To simulate micrometeoroid bombardment we used individual femtosecond laser pulses. We analysed the corresponding evolution of different spectral parameters, which we determined by applying the Modified Gaussian Model, and we also conducted principal component analysis.
Results. The original mineralogy of the surface influences the spectral evolution more than the weathering agent, as seen from the diverse evolution of the spectral slope of olivine and pyroxene upon irradiation. The spectral slope changes seen in olivine are consistent with observations of A-type asteroids, while the moderate to no slope changes observed in pyroxene are consistent with asteroid (4) Vesta. We also observed some differences in the spectral effects induced by the two weathering agents. Ions simulating solar wind have a smaller influence on longer wavelengths of the spectra than laser irradiation simulating micrometeoroid impacts. This is most likely due to the different penetration depths of ions and laser pulses. Our results suggest that in some instances it might be possible to distinguish between the contributions of the two agents on a weathered surface.

Key words. planets and satellites: surfaces – solar wind – meteorites, meteors, meteoroids – methods: data analysis – techniques: spectroscopic

1. Introduction

The surfaces of airless planetary bodies in the solar system are permanently exposed to the space environment, which consists mainly of solar wind irradiation and micrometeoroid bombardment. These processes cause changes to the topmost surface layers of the bodies, resulting in an alteration of their spectroscopic features (Hapke 1965, 2001; Wehner et al. 1963). The exact understanding of the individual contribution of these two processes to the alteration of reflectance s pectra i s o f utmost importance, and is the focus of our work.

Among the most prominent visible (VIS) and near-infrared (NIR) spectral changes observed on dry silicate bodies, such as the Moon or S-type asteroids, are spectral slope reddening (a decrease in reflectance towards shorter wavelengths), reduction of the diagnostic 1 and 2 μm absorption bands (Burns 1989), and an overall darkening of spectra (see e.g. Hapke 2001; Pieters et al. 2000; Pieters & Noble 2016).

Several silicate diagnostic features are also located in the mid-infrared (MIR) wavelength range, such as the Christiansen feature (around 8.5 μm) or the fundamental molecular vibration bands, the reststrahlen bands (Salisbury et al. 1991). Space weathering does not influence these in the same manner as those at VIS and NIR wavelengths. The most prominent MIR changes are the alteration of the shape, position, and relative intensities of

*All measured spectra in raw format are only available at the CDS via anonymous ftp to cdsarc.u-strasbg.fr (130.79.128.5) or via http://cdsarc.u-strasbg.fr/viz-bin/cat/J/A+A/654/A143

the reststrahlen bands (see e.g. Lucey et al. 2017; Brunetto et al. 2020).

The spectra of minerals are influenced by many effects related to space weathering, such as melting, vaporization and associated vapour redeposition, sputtering, particle size segregation, blistering, and amorphization. Many of the spectral changes are attributed to the creation of nanophase iron particles (Hapke 2001; Noguchi et al. 2014; Matsumoto et al. 2015; Pieters et al. 2000). These particles are created when an iron (Fe) ion is freed from the silicate crystalline structure during solar wind or micrometeoroid bombardment.

To evaluate and understand the spectral changes induced by space weathering, previous studies compared asteroid spectra with those of fresh compositionally identical meteorites. Additionally, many studies subjected meteorite and planetary analogue materials to laboratory simulations that mimic space weathering processes. Widely used techniques include ion irradiation, which simulates solar wind, and laser irradiation, which simulates micrometeoroid impacts.

Ion irradiation experiments have mostly verified the general trends of spectral darkening and reddening at VIS and NIR wavelengths. Several works related to silicate materials have given insights into space weathering, including Brunetto et al. (2006). By irradiating olivine and pyroxene samples and comparing their spectra with the spectrum of asteroid (832) Karin, they estimated its surface exposure age, which is in accordance with Karin's collisional history. Another example is the work of Fulvio et al. (2012), who simulated weathering on asteroid (4) Vesta by irradiation of eucrite meteorites. They found that different parts of the meteorite weather slightly differently. Based on their work, the diversity of V-type asteroids can be explained by distinct space weathering stages (for more examples of ion irradiation experimental work, see Lantz & Brunetto 2014; Lantz et al. 2017; Loeffler et al. 2009; Paillet et al. 2003; Vernazza et al. 2013).

Among the most prominent results based on laser experiments is the observation that the degree of weathering depends on the starting mineralogy of the processed sample (Yamada et al. 1999). Olivine shows much greater changes than pyroxene, and these changes are not linear with respect to time (Sasaki et al. 2002). Laser-irradiated ordinary chondrites can reproduce spectra of real asteroids, as shown by Sasaki et al. (2002), among others, for asteroids (349) Dembowska and (446) Aeternitas. After comparing laser-irradiated pyroxene samples with asteroid (4) Vesta, Yamada et al. (1999) concluded that Vesta is more weathered than their samples (for additional examples, see Gillis-Davis et al. 2018; Matsuoka et al. 2020; Moroz et al. 1996; Jiang et al. 2019; Sasaki et al. 2001a).

These laser irradiation experiments were mostly based on the irradiation effects induced by employing nanosecond pulsed lasers. The main argumentation in favour of this setting is that a duration of several nanoseconds approximately matches the duration of micrometeoroid impacts (Sasaki et al. 2002; Yamada et al. 1999). In addition, the ion yield created by irradiation is similar to the real situation in the case of high enough irradiation fluences (Kissel & Krueger 1987). Recent work of Fulvio et al. (2021) shows that morphology of the craters formed by nanosecond pulses resembles that induced by natural micrometeorite impacts. On the other hand, this set-up causes mainly heating and melting with subsonic and sonic evaporation from the surface (Gusarov & Smurov 2005). In contrast, a femtosecond laser pulse with high peak irradiance allows the propagation of a shock wave of several tens of GPa and confined melting (Berthe et al. 2011; Boustie et al. 2008). During such short pulses the laser beam does not interact with the created vapour plume. As a consequence of this set-up, ablation of the material proceeds through spallation, fragmentation, homogeneous nucleation, and vaporization (Perez & Lewis 2003), resulting in a subsurface structure of the craters that is remarkably similar to that of the Moon and of asteroid (25143) Itokawa (Fazio et al. 2018); the results are in accordance with the findings of Fiege et al. (2019) regarding the destruction of material by micrometeoroid impacts. Shirk (1999) also pointed out that the ablation depth is larger in the case of femtosecond (compared to nanosecond) regime due to increased absorption coefficient.

Despite these experimental efforts, the difference between the spectral effects of the solar wind and micrometeorite impacts is not well understood. Most of the laboratory work conducted to date has only focused on one specific space weathering process, either ion or laser bombardment. One of the exceptions is the work of Gillis-Davis et al. (2018), who showed that laser and electron irradiation of the Murchison meteorite separately yield small changes, but when combined the changes become significant. Another example is the comparison of ion and laser irradiation of olivine done by Loeffler et al. (2009). They found that different weathering mechanisms can lead to similar effects on the spectral curves of olivine-rich asteroids.

To analyse the differences induced by solar wind and micrometeoroid bombardment on planetary surfaces, we performed ion and laser irradiation experiments on the typical silicate minerals olivine and pyroxene. These minerals can be found not only in the S- and Q-type asteroids but also in V- and A-types and across the lunar surface (see Binzel et al. 2004; DeMeo et al. 2009; de León et al. 2006; de Sanctis et al. 2011; Gaffey et al. 1993; Keller & Berger 2014; Sanchez et al. 2014; Sunshine et al. 2007; Burns et al. 1972 and Isaacson & Pieters 2010 for the occurrence of these minerals on asteroid bodies and the Moon).

2. Methods

We performed two different types of irradiation experiments on terrestrial silicates also found on planetary surfaces: ion and femtosecond laser irradiation. For ion irradiation we used three different types of ions: hydrogen (H^+), helium (He^+), and argon (Ar^+). Laser irradiation was done using individual femtosecond laser pulses. Our experiments were conducted at three different institutes, but all of them were done using the same sample material (see Sect. 2.1), which gives a great opportunity for comparison of spectral signatures under different irradiation conditions. The experimental conditions are described in detail in Sects. 2.2 and 2.3. For an overview of the experimental set-up, see Table 1. For additional notes on experimental set-up, see Appendix A.

2.1. Samples

We acquired a bulk sample of aluminium-rich enstatite (pyroxene), including ≈7% pargasite, collected in Mäntyharju, Finland. Samples obtained from it are denoted OPX (OrthoPyroXene). We also used olivine pebbles from Hebei Province, China, as in Yang et al. (2017). Samples from the olivine pebbles are denoted OL. Based on electron probe microanalysis using CAMECA SX-100, the enstatite content[1] of the OPX sample was 67.1 ± 1.6 and

[1] Calculated as a ratio of Fe to magnesium (Mg) content: Fe/(Fe+Mg)*100.

Table 1. Overview of the experimental set-up.

Irradiation type		Irradiation (ions cm^{-2})	p (mbar)	Spectroscopy	Spectrometer set-up	Place
H^+	OL	10^{14}, 10^{15}, 10^{16}, 10^{17}, 2×10^{17}, 5×10^{17}, 10^{18}	10^{-7}	ex situ	Integrating sphere, $i = 10°$	HEL
H^+	OPX	10^{16}, 10^{17}, 2×10^{17}, 5×10^{17}, 10^{18}	10^{-7}	ex situ	Integrating sphere, $i = 10°$	HEL
He^+	OL, OPX	10^{16}, 3×10^{16}, 6×10^{16}, 10^{17}	10^{-7}	in situ	$i_V = c_V = 15°$, $\phi_V = 20°$ $i_N = 20°$, $c_N = \phi_N = 15°$	PAR
Ar^+	OL, OPX	10^{15}, 3×10^{15}, 6×10^{15}, 10^{16}, 2×10^{16}, 6×10^{16}, 10^{17}	10^{-7}	in situ	$i_V = c_V = 15°$, $\phi_V = 20°$ $i_N = 20°$, $c_N = \phi_N = 15°$	PAR
		Irradiation (J cm^{-2})				
Laser	OL	1.7, 2.4, 3.8, 4.6, 6.7, 10.4, 15, 23.4, 30.6, 60, 93.8, 375	10^{-4}	ex situ	$i = 0°$, $c = 30°$	PRG
Laser	OPX	4.5, 5.6, 12.5, 18, 28.1, 36.7, 50, 72, 112.5, 200, 450, 1800	10^{-4}	ex situ	$i = 0°$, $c = 30°$	PRG

Notes. OL and OPX stand for olivine and pyroxene, respectively; H^+, He^+, and Ar^+ correspond to hydrogen, helium, and argon ions, respectively; p is the pressure in the vacuum chamber during the irradiation; i is the incidence, c the collection, and ϕ the phase angle of the spectral measurements; the subscripts stand for different wavelength ranges: V is the visible and N is the near-infrared. HEL indicates the University of Helsinki laboratories, PAR indicates the INGMAR set-up at IAS-CSNSM in Orsay, and PRG indicates the laboratories at Charles University in Prague.

the forsterite content of the OL sample was 90.1 ± 0.8, evaluated from seven and nine measurements, respectively. These values are similar to H chondrite meteorites and diogenites (Norton 2002). For a discussion of possible contamination of our samples and its influence on the final results, see Appendix B.

Each of the materials was ground using a mortar and pestle, and consequently dry-sieved to <106 µm, which can be considered a suitable analogue of the regolith of planetary surfaces. The mean size of lunar regolith is around 60 µm (McKay 1978; Pieters et al. 2000), and its optical properties are, according to Pieters et al. (2000), dominated by regolith grains <45 µm. Our choice of sizes thus covers the most relevant size fraction for spectroscopic studies. Additionally, the sample also includes particles larger than the already mentioned 45 µm to give us a more relevant picture of a planetary surface. Particles larger than 100 µm are more than 100 times larger than the average wavelength of our VIS-NIR measurements. This means that they are already outside the so-called resonance size range regarding their light scattering behaviour and are within the geometric optics regime. At these sizes the light reacts with particle surfaces and subsurface volumes rather than with the particle as a whole, and the changes in particle size does not influence the distribution of the reflected light much. Including larger particles in our samples is thus not needed.

Using the Specac manual hydraulic press, we prepared two sets of pellets (OL and OPX) with a diameter of 13 mm. Each pellet was made of 100 mg of the mineral on top of 700 mg of potassium bromide (KBr) substrate. Using a KBr substrate ensures greater durability of the pellet. Still, the mineral layer on top is optically thick enough to enable analysis of only the mineral material. The approximate thickness of the mineral layer was 200 µm. The pellets were created using a pressure of 6 t for 6 min (≈450 MPa), which guarantees compactness of the material, while the mineral surface stays in a loose form that can be blown away or wiped off with a finger. This approach has already been used in the work of Brunetto et al. (2014) and Lantz et al. (2017), who also discuss the suitability of using the pellets for solar system studies. Some of the pellets are shown in Fig. 1.

2.2. Ion irradiation

He^+ and Ar^+ irradiation was conducted using the INGMAR set-up (IAS-CSNSM, Orsay) interfaced to the SIDONIE implanter (CSNSM, Orsay; see Chauvin et al. 2004; Brunetto et al. 2014). The pellets were placed into a vacuum chamber (pressure ≈10^{-7} mbar) for the whole experiment, that is the irradiation and spectral measurements. He^+ irradiation was done with 20 keV ions, simulating ions from solar active regions and solar energetic particles in the low-energy range. The energy of the ions is approximately five times greater than that of the standard solar wind. Nevertheless, by using argumentation similar to that of Brunetto et al. (2014), we can conclude that timescales corresponding to our irradiation fluences are correct within an order of magnitude to the standard solar wind situation. We used four fluences: 10^{16}, 3×10^{16}, 6×10^{16}, and 10^{17} ions cm^{-2}. In the case of Ar^+, we used 40 keV ions to simulate the effects of heavy ions in the slow solar wind, using seven different fluences: 10^{15}, 3×10^{15}, 6×10^{15}, 10^{16}, 2×10^{16}, 6×10^{16}, and 10^{17} ions cm^{-2}. The ion beam was scanned vertically and horizontally across the surface to produce homogeneous irradiation (Chauvin et al. 2004). Spectral measurements were performed in situ in the VIS wavelength range using a Maya2000 Pro (OceanOptics) and in the NIR range with a Tensor 37 (Bruker). The illumination angle for VIS measurements was 15° and the collection angle 15°. The phase angle was, due to the three-dimensional geometry, 20°. In the NIR wavelength range the illumination angle was 20°, the collection angle was the same as for VIS measurements, and the phase angle thus equalled 15°. The collection spot for VIS-NIR measurements was ≈4 mm on the surface of the sample pellet and the Spectralon, which was used as a calibration standard.

To simulate irradiation by the slow solar wind, we conducted the H^+ irradiation at the Helsinki Accelerator Laboratory, Finland, where we used 5 keV protons. As in the above-mentioned case of He^+ irradiation, our results can be applied to the standard solar wind situation. We irradiated using seven different fluences: 10^{14}, 10^{15}, 10^{16}, 10^{17}, 2×10^{17}, 5×10^{17}, and 10^{18} ions cm^{-2} in the case of OL samples and five different

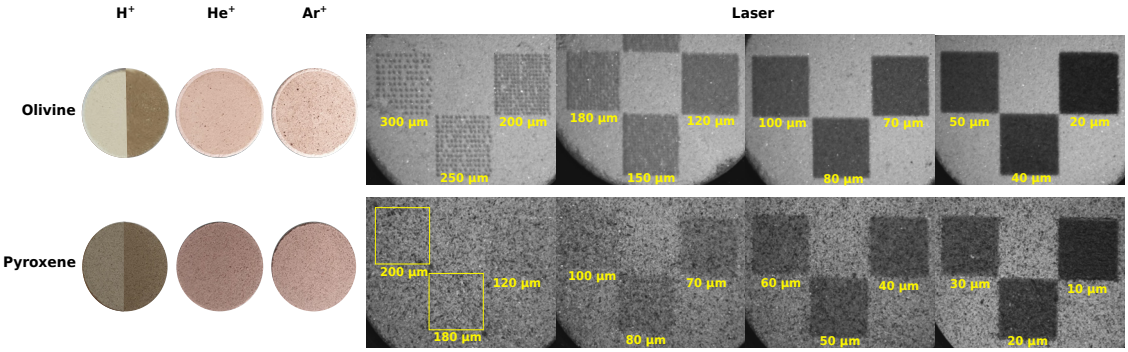

Fig. 1. Evolution of olivine and pyroxene pellets due to ion and laser irradiation. Pellets irradiated with hydrogen (H^+) are photocomposites of the fresh surface in the left part and the 10^{18} ions cm^{-2} irradiation in the right part. Pellets irradiated with helium (He^+) and argon (Ar^+) display the surface after 10^{17} ions cm^{-2} irradiation; only the outermost annulus represents the fresh surface and was created by using a mask during irradiation. Yellow squares (3×3 mm in size) in the photograph of a pyroxene pellet irradiated by laser indicate the regions of the least dense irradiation that are not visible by eye. The yellow numbers in the figure represent the spacing between two consecutive laser shots; for equivalent values of energy densities, see Table 1: the sequence of the distances relevant to one material in this figure (from left to right) corresponds exactly to the list in the table.

fluences: 10^{16}, 10^{17}, 2×10^{17}, 5×10^{17}, and 10^{18} ions cm^{-2} in the case of OPX samples. During irradiation the samples were placed in a vacuum chamber ($\approx 10^{-7}$ mbar), but the spectral measurements were performed ex situ. As was noted, for example, by Loeffler et al. (2009), after the sample is taken out of the vacuum chamber in which the irradiation was taking place, reoxidation of the created metallic Fe nanoparticles takes place within minutes. This may erase part of the spectral changes. Before extraction from the vacuum chamber, we thus filled the chamber with a mixture of nitrogen and 2% oxygen gas, which guaranteed that only a thin surface layer of the sample oxidized protecting the underlying nanophase Fe particles (for more details on surface passivation, see Kohout et al. 2014, and their scanning transmission electron microscopy analysis of nanophase Fe particles). The hemispherical reflectance spectra were measured in the shortest possible time after the irradiation using an OL-750 automated spectroradiometric measurement system by Gooch & Housego located at the Department of Physics, University of Helsinki (Penttilä et al. 2018). The OL-750 instrument is equipped with polytetrafluoroethylene (PTFE) and golden integrating spheres and with a specular reflection trap. The spectra were measured relative to PTFE (VIS) and golden (NIR) standards. The spectral resolution of the instrument varied between 5 and 10 nm. The spectrometer had an identical viewing geometry for all the segments of the spectra and an incidence angle of 10° to the surface normal. The size of the collection spot on the sample surface was ≈6 mm for both the segments.

2.3. Femtosecond laser irradiation

We conducted the femtosecond laser irradiation at the Department of Chemical Physics and Optics, Charles University, the Czech Republic. Our set-up was inspired by the work of Fazio et al. (2018). We used a titanium sapphire Tsunami laser and Spitfire amplifier, Spectra-Physics, Newport. The laser wavelength was 800 nm and it shot individual 1.5 mJ (for OL) and 1.8 mJ (for OPX) 100 fs pulses into a square grid (3×3 mm). The spot size on the surface of the pellet was ≈50 µm, as estimated by the razor blade method (see e.g. Khosrofian & Garetz 1983). The final energy surface density (further noted as energy density) of one pulse was then ≈80 J cm^{-2}. Considering a dust particle with a diameter of 1 µm and typical velocity of 10 km s^{-1}, the energy density of our experiments is comparable to that of a micrometeoroid impact (≈32 J cm^{-2}). By varying the spatial distance between the adjacent pulses we simulated different levels of space weathering; the higher the density of the pulses, the higher the simulated space weathering level. The lowest coverage corresponds to one shot every 300 µm, that is 100 pulses in our 3 mm square, and the highest to one shot every 10 µm, resulting in 9 000 pulses in a square. In the case of OL we used the following irradiations (recalculated to the energy density, calculated as a number of pulses in cm^2 times energy of one pulse): 1.7, 2.4, 3.8, 4.6, 6.7, 10.4, 15.0, 23.4, 30.6, 60.0, 93.8, and 375.0 J cm^{-2}, and in the case of OPX: 4.5, 5.6, 12.5, 18.0, 28.1, 36.7, 50.0, 72.0, 112.5, 200.0, 450.0, and 1800.0 J cm^{-2}. We accommodated four such squares onto a pellet, with one of them always left unirradiated as a reference of the fresh state. The irradiation was conducted in a vacuum chamber ($\approx 10^{-4}$ mbar). Samples then had to be taken out of the chamber as the spectral measurements were done in a different laboratory, for which we surface passivated them as in the case of the H^+ irradiation (see Sect. 2.2).

The VIS and NIR spectral measurements were made using a Vertex 80v, Bruker, with an A513/Q variable angle reflection accessory using the Spectralon standard. The incidence angle was set to 0° and the collection angle to 30° to comply with Reflectance Experiment Laboratory (RELAB) database spectra. The vacuum in the spectrometer chamber was of the order of several mbar.

With this spectrometer, we measured not only the VIS and NIR spectra but also the MIR spectra of all the samples (even those irradiated by ions) up to 13 µm. The collection spot on the sample's surface was ≈1.5 mm for all the segments of the spectra, which ensured that only the irradiated part of the sample (3×3 mm square) was measured but that it still contained at least (in the case of the least dense irradiation) 16 laser-induced craters. We did not have the commonly used calibration standard for these measurements; we thus used a silver-coated diffuse reflector from Thorlabs, which has a relatively uniform and high reflectance (>95%) in the MIR wavelength range. Consequently,

we measured the diffuse reflector against the golden standard using the same observation geometry and the same set-up at the German Aerospace Centre to get the absolute calibration. The absolute values may thus in the case of MIR measurements be slightly offset; we therefore use only relative values to make conclusions in this case.

All segments of all the measured spectra in absolute values are available at the Centre de Données astronomiques de Strasbourg (CDS).

2.4. Spectral fits

To obtain spectral parameters from the measured VIS–NIR spectra, we used the Modified Gaussian Model (MGM) by Sunshine et al. (1990, 1999). The MGM takes a spectrum and an input file with user-estimated spectral parameters, and iteratively searches for the best fit of the spectrum, in our case realized by a second-order polynomial continuum and a set of absorption bands, represented by modified Gaussian curves, all in the natural logarithm of reflectance. The choice of second-order polynomial is supported, for example, by the research of Clénet et al. (2011) or Han et al. (2020). The depth of individual absorption bands is expressed by the band strength parameter, which corresponds to the amplitude of the modified Gaussian curve.

Pyroxene exhibits two characteristic absorption bands at around 1 and 2 μm (Burns 1989). Pargasite inclusions show a weak absorption at 0.9 μm, and another set of absorptions mainly between 2.2 and 2.4 μm (Bhatt et al. 2017; Rommel et al. 2017). These are minor compared with the strong OPX absorptions, but we still fitted them, so the root-mean-square error decreases (see arrow in Fig. 2 for the only visible pargasite band).

In OL we observe three deep absorptions around 1 μm (Burns 1970). These absorptions are so close to each other that they overlap in the resulting spectrum.

2.5. Principal component analysis

To compare the results of ion- and laser-irradiated spectra, we also applied principal component analysis (PCA) to them. This dimensionality reduction technique takes an m-dimensional cloud of points, where m is the number of wavelengths in the spectral data, and transforms it so that in the new orthogonal coordinate space the first coordinate (first principal component, PC1) corresponds to the direction in which the original cloud showed the greatest variance, the second coordinate (PC2) represents the direction with the second greatest variance, and so on. The new coordinate system usually does not have an exact physical meaning, but its usefulness has been proven in previous research: for example, for asteroid taxonomy based on PCA, see DeMeo et al. (2009); for analysis of meteorite spectra, see Penttilä et al. (2018); for research on the lunar magnetic anomalies, see Chrbolková et al. (2019) and Kramer et al. (2011); and for PCA applied to the spectra of galaxies, see Connolly & VanderPlas (2014).

We applied PCA to our measured spectra to obtain more information on spectral differences. Furthermore, DeMeo et al. (2009) published an article based on a dataset of the spectra of 371 asteroids measured from 450 to 2500 nm. These asteroids were assigned spectral types. For our analysis (based on silicate minerals) we extracted S-, Q-, V-, and A-type asteroids from this dataset. The principal component space defined by the measured irradiated pellets can be used as a basis for the asteroid spectra. The only constraint is that the asteroid spectra have the same format (wavelength sampling and range) as the original measured spectra. We thus obtained the principal component transformation of the asteroid spectral curves and could compare them with the irradiation evolutions.

3. Results

We conducted the irradiation as described in Sects. 2.2 and 2.3. Examples of the visual changes of the pellets' surfaces are shown in Fig. 1. The spectra resulting from the irradiation are displayed in Fig. 2.

3.1. Time and energy evolution

We fitted all of the measured spectra using the MGM, as described in Sect. 2.4, and plotted the spectral parameters as a function of astrophysical timescale, which we calculated from irradiation fluences and crater densities in accordance with the solar wind and dust fluxes at 1 au (see Appendix C). The evolutions of albedos, spectral slopes, and band strengths for each of the materials can be found in Fig. 3. We observe that even though the changes in albedo are of a similar order for olivine and pyroxene, pyroxene's spectral slope does not change much compared with that of olivine.

We also note that the central olivine band does not change its strength significantly compared with the two outer bands (at ≈850 and 1250 nm). The band at ≈850 nm changed more (by ≈55% for maximum irradiation) than the band at ≈1250 nm (30%) (see Fig. 3).

An example of how spectral parameters evolve with respect to the energy density delivered to the surface can be found in Fig. 4, where the evolution of the spectral slope is shown. For olivine we can see that samples irradiated by all ions follow a similar evolution up to a threshold energy density. Above this the H^+-irradiated sample undergoes a rapid change in the value of the spectral slope. This happens even for other studied parameters (albedo, band strengths, area of bands), but only in the case of olivine. Pyroxene does not show this behaviour in any of the parameters. See Appendix D for more information and discussion.

We also find that laser influences the spectral slope of olivine at low densities of energy more than ions. However, comparing the evolution of the spectral slope from Fig. 4 to that in Fig. 3, we see that the time needed to accumulate equivalent spectral change by laser or micrometeoroid impacts is several orders of magnitude greater than that needed in the case of H^+ irradiation at 1 au.

3.2. Short versus long wavelengths

In Fig. 5 we demonstrate the spectral differences related to the effects induced by laser and ion irradiation. Four different types of bars corresponding to different types of irradiation are plotted. The upper end of each bar indicates the reflectance of the fresh spectrum at the given wavelength. The lower end of the bar shows the reflectance of the spectrum irradiated by the fluence written in the legend. The longer the bar, the more the material changed due to ion or laser irradiation; in other words, the greater the absolute change of the spectrum at that wavelength.

We intentionally selected the spectral curves of the laser and H^+ ion irradiation that have similar reflectance variation at VIS wavelengths, and studied how the reflectance at NIR wavelengths behaves. We can see that the laser irradiation causes variations at long wavelengths greater than the H^+ ions, as seen, for example, from the ratio of the laser to the H^+ bar lengths at

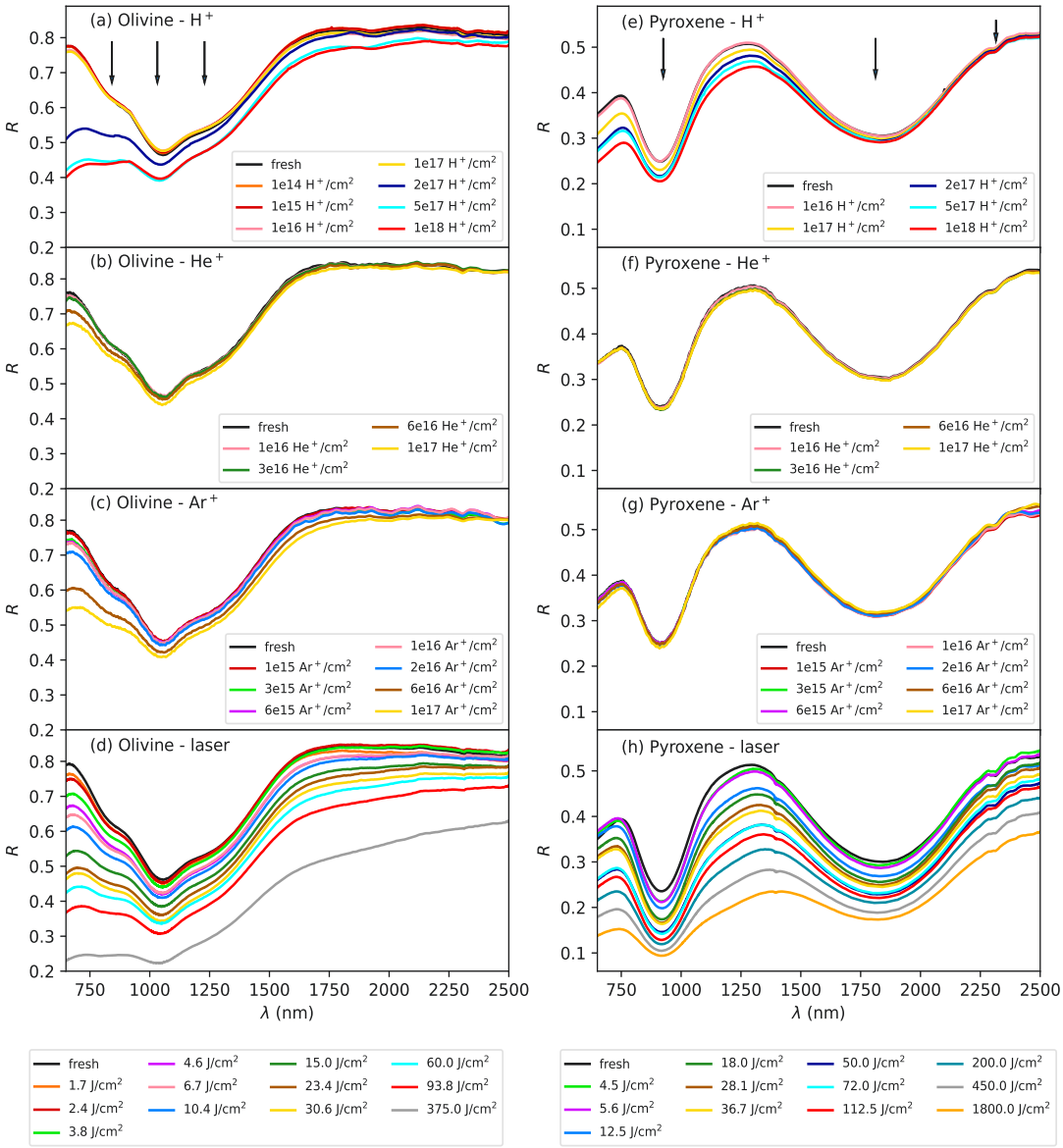

Fig. 2. Evolution of spectra due to different irradiation methods. *Left*: olivine irradiated by (*a*) hydrogen (H^+), (*b*) helium (He^+), and (*c*) argon (Ar^+) ions, and (*d*) femtosecond pulsed laser with various ion fluences (ions cm^{-2}) or energy densities ($J\,cm^{-2}$) (see Sect. 2.3 for more details). *Right*: (*e–h*) pyroxene undergoing the same processing described for olivine in the left panel. In the graphs *R* stands for reflectance and λ is the wavelength. The arrows in (*a*) and (*e*) indicate the position of the diagnostic mineral bands; the smallest arrow in (*e*) refers to the position of the only visible pargasite band.

short and long wavelengths, which drops by 50% in the case of olivine and by 70% in the case of pyroxene. He^+ and Ar^+ ions do not show variations at the VIS wavelengths that are as prominent as those for H^+ ions because we did not reach high enough irradiation fluences. Nevertheless, the trend of decreasing reflectance variation towards longer NIR wavelengths is visible even for these two types of ions. Relative to laser bars, He^+ and Ar^+ bars drop by 23 and 43% at longer wavelengths in olivine. In pyroxene Ar^+ shows a 24% drop, and the change in He^+ is insignificant.

In contrast to Fig. 5, Fig. 6 shows relative changes in the spectra. It displays ratios of fresh to irradiated spectra. In this figure we plot spectra that represent similar energy density irradiation. There is a clear difference between olivine and pyroxene irradiated by laser. Olivine shows a major slope change in the VIS wavelengths, whereas in the case of pyroxene the

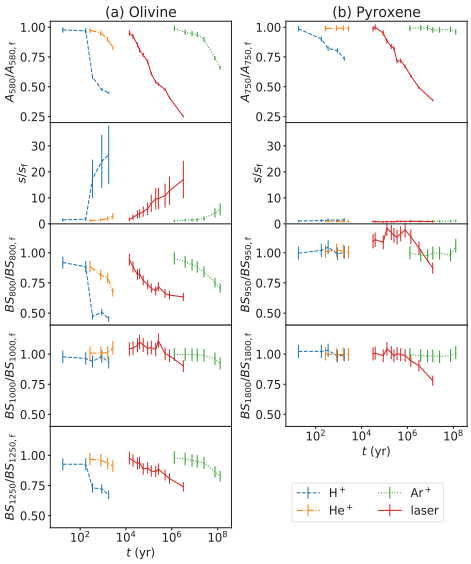

Fig. 3. Time evolution of spectral parameters of (*a*) olivine and (*b*) pyroxene. Each curve corresponds to one type of irradiation and connects points denoting individual irradiation steps. H^+ stands for hydrogen, He^+ for helium, and Ar^+ for argon ions. Time, *t*, was estimated for 1 au (see Appendix C for more detail), A_λ denotes albedo at a given wavelength, *s* stands for the spectral slope, and BS_λ stands for the strength of a band centred at a given wavelength λ. All parameters are divided by the corresponding spectral parameter of the fresh (f) material and include error bars. For details of pyroxene spectral slope changes, see Fig. 4.

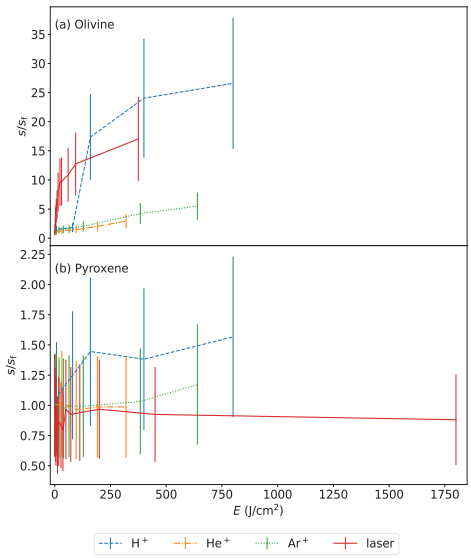

Fig. 4. Evolution of spectral slopes, *s*, of (*a*) olivine and (*b*) pyroxene with respect to the energy density, *E*. Each curve corresponds to one type of irradiation and connects points with increasing irradiation. H^+ stands for hydrogen, He^+ for helium, and Ar^+ for argon ions. Spectral slopes are divided by the corresponding spectral slope of the fresh material, s_f, and include error bars.

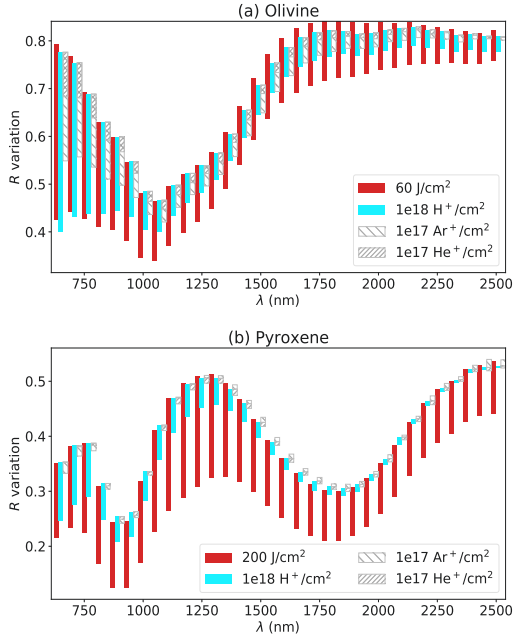

Fig. 5. Bar plot showing reflectance, *R*, variation induced by laser and ion irradiation experiments. Each bar connects at the upper end the reflectance of the fresh material and at the lower end the reflectance of the material weathered to the level stated in the legend. The length of the bar thus shows the variation in the reflectance at the given wavelength, λ. Instead of showing bars at all measured wavelengths, we down-sampled the spectra to 50 nm intervals to enhance readability. H^+ stands for hydrogen, He^+ for helium, and Ar^+ for argon ions.

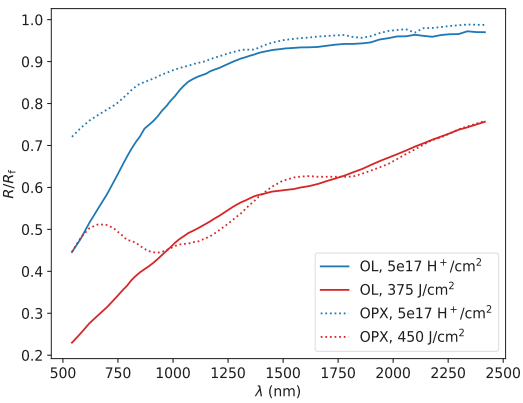

Fig. 6. Ratios of reflectance, *R*, of irradiated and fresh (f) spectra of olivine (OL) and pyroxene (OPX), irradiated by hydrogen (H^+) ions and laser. λ stands for wavelength. A similar plot for mid-infrared measurements is in Fig. E.1.

slope change is not as pronounced, and we see that for the laser-irradiated pyroxene the absorption bands are altered. Furthermore, in the case of olivine, both types of irradiation cause much steeper changes at shorter than at longer wavelengths. The wavelength at which the behaviour changes is around 1 µm.

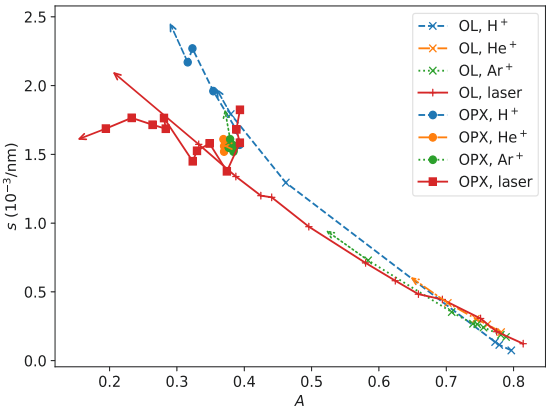

Fig. 7. Correlation of the albedo (A) and spectral slope (s) for olivine (OL) and pyroxene (OPX), subject to different irradiation set-ups. Each line connects the individual irradiated steps due to one type of irradiation. H^+ stands for hydrogen, He^+ for helium, and Ar^+ for argon ions. The highest irradiation states are indicated by the arrows' tips.

3.3. Albedo–slope correlation and principal component analysis

Similarly to Gaffey (2010), we plotted a correlation of albedo (reflectance at a given wavelength) and spectral slope for our measurements (see Fig. 7). Each line corresponds to the evolution due to a different type of irradiation and markers on it highlight the individual irradiation steps. We see a clear trend of decreasing albedo and increasing spectral slope in all cases, except for the pyroxene irradiated by laser, for which mainly the albedo changes, but the spectral slope varies only slightly.

Additionally, the inclination of the curves is ordered $H^+ \rightarrow He^+ \rightarrow Ar^+ \rightarrow$laser, thus from the lighter to the heavier ions, and then to micrometeoroid impacts. A similar sequence is seen in the principal component space (see Fig. 8). We can clearly see that all the irradiation types follow approximately the same direction in the PC1 versus PC2 plot. The direction of the trends thus represents the space weathering evolution. From the first three, mainly the second principal component distinguishes between the different minerals. The separation of individual irradiation types is even more pronounced in the third principal component.

As described in Sect. 2.5, we also compared the asteroid spectra with our dataset (see Fig. 9). Even though the asteroids occupy a different part of the principal component space than our laboratory spectra, presumably due to the different origins, their distribution is significantly ordered. We find that the direction of weathering indicated by our experiments is parallel to the cloud of the Q- and S-type asteroids, with the Q-type asteroids at one end (in the less weathered direction) and the S-type asteroids at the other end. A- and V-type asteroids, as representatives of nearly pure olivine- and pyroxene-rich bodies, respectively, clustered into the separate clouds, and their orientation in the principal component space matches that of our laboratory spectra.

3.4. Mid-infrared spectra

Figure 10 shows selected olivine and pyroxene MIR spectra. We observe slight shifts in the positions of the reststrahlen bands

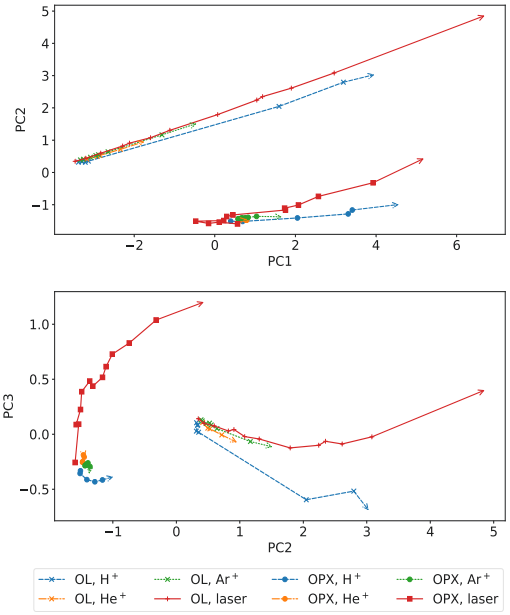

Fig. 8. Principal component (PC) plots for olivine (OL) and pyroxene (OPX) subject to different irradiation set-ups. Each point in the graph represents one irradiation state. H^+ stands for hydrogen, He^+ for helium, and Ar^+ for argon ions. The highest irradiation states are indicated by the arrows' tips.

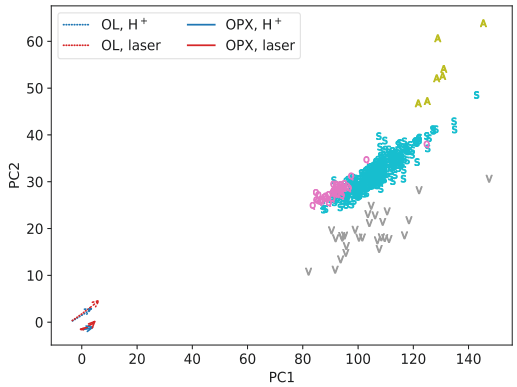

Fig. 9. Principal component (PC) plot for olivine (OL) and pyroxene (OPX) subject to different irradiation set-ups and including S-, Q-, V-, and A-type asteroids. Each letter (spectral type) in the graph represents the position of one asteroid in the principal component space. The spectra of irradiated pellets have the same positions as in Fig. 8 (top); for better readability, only hydrogen (H^+) and laser irradiation are shown. The most irradiated spectra are indicated by the arrows' tips (the maturation thus goes from the lower left to the top right corner).

(between ≈9.5 and 12 μm) and also alterations in the band's shapes, as also demonstrated in Fig. E.1 (MIR wavelength range alternative to Fig. 6). We studied the evolution of the position of the Christiansen feature and found that the change is only several percentage points in our set-up. The most prominent change happened in both cases, for olivine and pyroxene, for

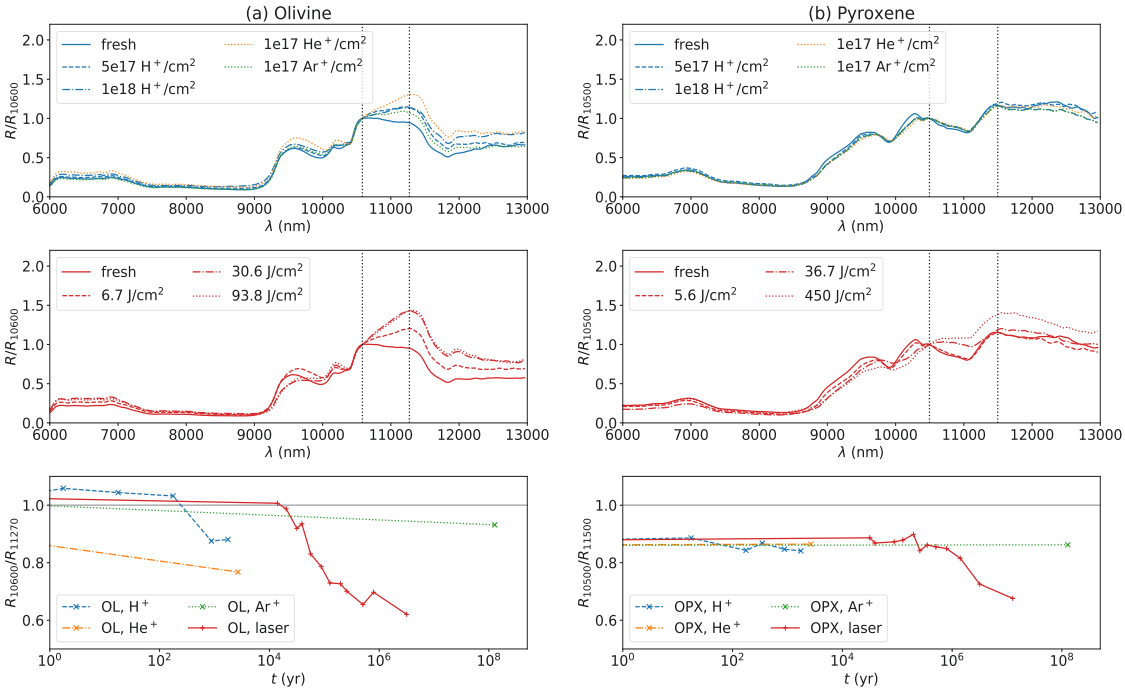

Fig. 10. *Top and middle*: mid-infrared part of some of the spectra of (*a*) olivine (OL) and (*b*) pyroxene (OPX) irradiated by ions and by laser. The two dotted lines show the approximate positions of the reflectance values (R), based on which the ratio of the peaks was evaluated. The spectra were normalized at the wavelength (λ) of the first peak used for the ratio calculation to highlight the spectral alteration. *Bottom*: evolution of the reflectance ratio due to different irradiation set-ups. Time, t, was evaluated for the situation at 1 au (see Appendix C). A grey horizontal line indicates the situation of the flattened peaks. H^+ stands for hydrogen, He^+ for helium, and Ar^+ for argon ions.

the laser-irradiated samples. In the case of olivine, the Christiansen feature shifted to the longer wavelengths (from 8803.4 to 8986.5 nm), and for pyroxene to the shorter ones (from 8472.6 to 8191.5 nm for the maximum laser irradiation).

In Fig. 10 (bottom) it is also apparent that the two major olivine reststrahlen bands at around 11 μm changed their relative intensities with increasing irradiation. All fresh olivine spectra have a shorter-wavelength peak that is more intense than the longer-wavelength peak, and as the irradiation continues, the shorter-wavelength peak becomes less intense than the longer-wavelength one. This happens for ion- and for laser-irradiated olivine. A similar conclusion can be made for pyroxene irradiated by laser. In the case of ion-irradiated pyroxene, the ratio did not change very much.

4. Discussion

4.1. Comparison with previous visible and near-infrared works

As seen in the time and energy density evolution plots, Figs. 3 and 4, spectral changes induced by different types of ions within one type of material are, in general, similar but they differ in their details. The reason for this is the different interaction of the incoming ion with the target material. The way an ion loses its energy in the material depends on the size of the ion, on its energy, and also on the target material (Brunetto & Strazzulla 2005). We used three different types of ions, with two different materials. All of the experiments thus simulated different energy loss regimes. When an ion loses energy through inelastic (i.e. electronic) processes, the target material is subject to ionization. If the interaction is elastic (i.e. nuclear), the material is subject to the creation of vacancies, phonons, and recoils.

We calculated numerical simulations of our experiments using the SRIM software (Ziegler & Biersack 1985) to obtain information on the different regimes of elastic and inelastic energy losses in the material. An overview can be found in Table 2. We can see that the energy loss proceeds through inelastic collisions in the case of our H^+ and He^+ irradiation, as the electronic stopping power is larger than the nuclear stopping power. Ar^+ irradiation, on the other hand, is mostly subject to elastic collisions and produces the most vacancies per incoming ion of all the irradiation set-ups. We also calculated the SRIM simulations for some earlier published works to be able to compare their results with ours (see Table 2).

Loeffler et al. (2009), who used olivine with similar forsterite content, obtained albedo changes very similar to those we see in our He^+ irradiation. As we can see from Table 2, Loeffler's set-up caused half the number of vacancies per ion, but the nuclear stopping power, which is, according to Brunetto et al. (2014), correlated with the spectral change, was twice as large. A larger albedo variation in samples irradiated by Lantz et al. (2017) is probably connected to the higher energy of impacting ions, which caused a penetration depth of the ions that was two times greater (see the next section for more details on the connection of the penetration depth of ions to the spectral response). Comparing our Ar^+ irradiation with that of Kaňuchová et al. (2010),

Table 2. Results of the SRIM simulations of the individual ion irradiation.

	Mineral	Ion	E (keV)	d (nm)	S_e (MeV/(mg cm^{-2}))	S_n (MeV/(mg cm^{-2}))	Vacancies/ion
This work	OL	H^+	5	58 ± 29	0.204	0.007	3.4
		He^+	20	132 ± 51	0.380	0.035	52.2
		Ar^+	40	31 ± 10	0.929	2.731	393.1
This work	OPX	H^+	5	61 ± 32	0.193	0.007	3.7
		He^+	20	142 ± 57	0.352	0.034	56.8
		Ar^+	40	33 ± 11	0.850	2.644	414.8
Loeffler et al. (2009)	OL	He^+	4	29 ± 19	0.017	0.073	21.1
Lantz et al. (2017)		He^+	40	241 ± 70	0.530	0.022	66.1
Kaňuchová et al. (2010)		Ar^+	400	97 ± 62	2.544	1.214	2146.5
Marchi et al. (2005)	OPX	Ar^+	200	152 ± 29	1.916	1.740	1441.2
Lantz et al. (2017)	CPX	He^+	40	252 ± 77	0.499	0.022	74.8

Notes. Results of olivine (OL) and pyroxene (OPX) simulations. E stands for the energy of the incoming ion; d is the penetration depth; S_e and S_n are the electronic and nuclear stopping powers; H^+, He^+, and Ar^+ denote hydrogen, helium, and argon ions, respectively. In the model we used the following densities: 3.2 g cm^{-3} for OPX and 3.3 g cm^{-3} for OL. We also calculated SRIM simulations for some of the previous experimental work available in the literature, using compositions and densities relevant to the given experiment. CPX represents clinopyroxene.

we obtained albedo changes that were twice as large, but applied twice the energy per cm^2. This also corresponds to the values of the stopping powers in the table.

In the case of He^+ and Ar^+ irradiation, the pyroxene spectra did not alter much. In contrast to our results, other work using pyroxene of a different composition achieved noticeable spectral change. For example, Marchi et al. (2005) irradiated Bamble orthopyroxene using Ar^+ ions. Bamble orthopyroxene has an ≈20% higher enstatite number than our samples (Bowey et al. 2020; Cloutis et al. 1986), which could have influenced the inclination of the sample to the space weathering related changes. Based on the SRIM simulation of Marchi's experiment the electronic and nuclear stopping powers are comparable, whereas in our case the nuclear stopping power was greater than the electronic stopping power (see Table 2). In addition, our configuration caused several times fewer vacancies per ion, which may have resulted in the different spectral evolutions as the material was less affected in our experiment.

If we compare the spectral changes of our laser irradiation experiments with those in the literature, we find alterations of a similar level, even though these were done mostly using nanosecond laser pulses that induce different post-irradiation processes in the sample. The olivine albedo changes are comparable for instance to those in the work of Yang et al. (2017), who used the same olivine material, and the pyroxene changes are similar to the work of Sasaki et al. (2002).

No matter what irradiation type we used, the central olivine band (at ≈1000 nm) changed its strength less than the two outer olivine bands (at ≈800 and 1250 nm). The same behaviour has already been described by Han et al. (2020), among others. There is a theoretical explanation of this given in Penttilä et al. (2020). The absorption in material follows approximately the Beer–Lambert exponential law. The same amount of darkening agent from space weathering in an initially brighter material will decrease the reflectance more compared with an initially darker material. The central olivine band (at 1000 nm) is the deepest in the fresh material, and thus will have the smallest absolute decrease. Additionally, the 800 nm band changed more significantly than the 1250 nm band, which correlates with the asymmetry of the imaginary part of the refractive index of olivine observed by Brunetto et al. (2007b).

4.2. Wavelength-dependent changes and penetration depth

In Fig. 5 we see that all of the ions influence the longer NIR wavelengths less than laser irradiation, while the impact of the laser and H^+ irradiation on shorter wavelengths was comparable. This results in more significant reddening of the H^+-irradiated compared with the laser-irradiated spectra in the time evolution plots (Fig. 3).

An explanation for this difference can be found in the different penetration depths of the ions and laser (different mechanisms of the radiation damage). We used the SRIM software to evaluate the penetration depths of H^+, He^+, and Ar^+ ions in olivine and pyroxene. We obtained penetration depths ranging from 31 to 142 nm (see Table 2). Ion irradiation creates in situ damage of the surface layer, which happens over a relatively long timescale of the irradiation experiment and presumably causes in situ amorphization, crystalline lattice dislocations, and occurrence of nanophase Fe particles (Laczniak et al. 2021).

Based on simple light scattering simulations using olivine and pyroxene slabs of different widths and using the extinction coefficients from the Database of Optical Constant for Cosmic Dust[2], we estimated the penetration depth of the laser beam as ≈100 µm. The timescale of the energy delivery is comparable to the timescale of the laser pulse (≈100 fs) causing instant ablation of the irradiated volume. The ablated material is subsequently redeposited on top of the in situ damaged zone creating amorphous redeposition layer with possible presence of nanophase Fe particles (Weber et al. 2020). Thus, the resulting pattern of the affected surface grains is expected to be more complex than in the case of ion irradiation.

Based on the above-mentioned estimates, we can thus conclude that the laser penetrated much deeper into the sample than the ions. We can make a similar estimate for the penetration depths of the spectral beam. For olivine the penetration depth in the wavelength range of 0.7–2.5 µm (VIS-NIR) is of the order of 100 µm, while at 10 µm (MIR region) it drops to <1 µm. For pyroxene, the extinction coefficients are larger, and the penetration depths would thus be even smaller. The VIS and NIR

[2] https://www.astro.uni-jena.de/Laboratory/OCDB/crsilicates.html#E (Zeidler et al. 2011; Huffman & Stapp 1971).

spectral beams therefore work in the volume scattering regime, as commented also by Brunetto et al. (2020). Based on these numbers, the NIR spectral beam probes far deeper into the material (≈100 μm) than the depth of the material altered by ions (<200 nm). The spectra thus represent a mixture of the fresh and irradiated material, and the spectral change is small. On the other hand, reflectance from the laser-irradiated pellet is influenced mainly by the altered material (because the penetration depth of the laser pulse is slightly greater than or similar to the penetration depth of the spectral beam); laser irradiation thus creates a greater variation in the NIR wavelength range.

Additionally, as Brunetto et al. (2007b) showed, after laser ablation the extinction coefficients of both olivine and pyroxene increase throughout the VIS and NIR wavelengths, which results in a decreased penetration depth of the light. The change in the coefficient is orders of magnitude larger for the VIS wavelengths than for the NIR. Penttilä et al. (2020) modelled evolution of olivine extinction coefficients and found that inclusions of nanophase iron alter the VIS extinction coefficients ≈20 times more than the extinction coefficients in the NIR wavelength range. The reason for this is the different size of nanophase iron particles relative to the wavelengths of the VIS and NIR light. Assuming that changes such as Brunetto et al. (2007b) and Penttilä et al. (2020) found are similar for our ion irradiations, we can explain why in the VIS wavelengths the reflectance variation in H^+- and laser-irradiated samples is comparable: the relative contribution of the H^+-irradiated layer is probably larger in the VIS than in the NIR range. The MIR region is subject to the surface scattering regime, where all the four types of irradiation caused damage, and thus would be indiscernible.

Another way to visualize the different behaviour at the short and long wavelengths of our spectra is shown in Fig. 6. Especially in the case of olivine, a significant change in the slope alteration at around 1000 nm is visible. This figure also shows that even though the ions mainly modify the spectral slope, pyroxene irradiated by laser displays very little slope change, and we observe mainly the band depth changes.

Supporting our findings, Weber et al. (2020) pointed out that depending on the space weathering agent, the micro-structure of the minerals in space is influenced significantly differently.

4.3. Space weathering versus mineralogy

Even though we observed a difference in the effect of ions and laser pulses at the NIR wavelengths, generally we observed that the initial mineralogy of the pellet has a more significant effect on the final evolution of the spectral features than the type of irradiation.

In Fig. 3 we see that even though the albedo changes of olivine and pyroxene are of a similar order, they differ significantly when considering the evolution of other spectral parameters, especially the spectral slope. Olivine shows major changes in the values of the spectral slope, but pyroxene changes only mildly. We can also see this trend in Fig. 7, where especially pyroxene irradiated by laser shows major changes in albedo but nearly no change in spectral slope.

Such inconsistency of behaviour was studied on an atomic scale by Quadery et al. (2015). When OPX is irradiated by ions, its crystalline structure suffers defects. Quadery et al. (2015) showed that such defects are easily healed by ions from the bulk (subsurface layers) of the sample, which ensures that this material stays stable longer. On the other hand, olivine does not have such an ability, and thus weathers more quickly as there are no species that would renew the topmost layers.

A similar difference in susceptibility to the laser irradiation was reported by Weber et al. (2020). Based on their transmission electron microscopy analysis of olivine and pyroxene (both of similar composition to our samples), they found that the thickness and also the nanostratigraphy of the layer altered by the irradiation differs for these two minerals, which is consistent with the different penetration depths of light in olivine and pyroxene that we noted in Sect. 4.2.

The PCA pointed to the space weathering trend in the measured data. All the irradiated steps, due to one type of irradiation, lie on approximately straight lines in the plot of the first two components in Fig. 8 (top). Remarkably, in each of the compositions, the H^+-irradiated evolution lies at the lowest values of PC2 and the laser-irradiated case at the highest PC2 (the same holds for Fig. 8, bottom). More significantly, the PCA divides the measured spectra into two main clouds based on the composition. The PCA thus identifies the different mineralogies. Furthermore, the asteroid spectra also cluster based on the mineralogy in the principal component space (Fig. 9) and their orientation matches that of our laboratory spectra. This means that our spectra are a suitable analogue to the asteroid data. The plot of the first two principal components shows the trends due to the influence of the micrometeoroid impacts and solar wind only as second-order information. Only the third principal component is capable of distinguishing some differences in various irradiation types.

4.4. Consequences for asteroid studies

4.4.1. Pyroxene-rich asteroids

As we discuss above, pyroxene experiences only minor changes in spectral slope, and the strengths of the absorption bands are also quite stable when compared to the amplitude of changes in olivine. On the other hand, H^+ ion and laser irradiation induces major changes in pyroxene albedo.

We see such inconsistency in the amplitude of changes of different spectral parameters even in some asteroids, for example (4) Vesta. As Pieters et al. (2012) pointed out, Vesta's surface shows a range of pyroxene compositions. From observations of the Dawn mission, very strong absorption bands and nearly no continuum changes are seen, even though there are various dark and bright regions. The albedo changes, although the absorption bands are strong and thus look fresh. Pieters et al. (2012) claim that Vesta does not show the typical (lunar-type) space weathering caused by an accumulation of the nanophase Fe particles, but rather a small-scale mixing of diverse surface components. Vernazza et al. (2006) tried to simulate space weathering on Vesta through ion irradiation of a eucrite meteorite (presumable analogue) and, unlike us, they found that the spectrum should change even in terms of the spectral slope. As the slope changes are not observed on Vesta, Vernazza et al. (2006) concluded that Vesta's surface is shielded from the solar wind by a magnetic field. Instead, our pyroxene did not show significant reddening of the spectral slope; the weathering at Vesta thus may proceed even without the presence of contamination by carbonaceous material or a magnetic field. In addition, as Fulvio et al. (2012) showed, there is variation in the slope behaviour of individual eucrite meteorites upon ion irradiation.

4.4.2. Olivine-rich asteroids

As shown in Fig. 3a, the spectral slope of H^+-irradiated olivine pellets increased considerably over only several hundred years (at 1 au, for the main asteroid belt, the value would be approximately 10 times longer). This means that the solar wind component

of the space weathering has a significant and rapid effect on olivine-rich asteroids, explaining the observed high slopes of A-type asteroids (see e.g. Cruikshank & Hartmann 1984 and DeMeo et al. 2009). For example, asteroid (1951) Lick shows a 10^7–10^8 yr old surface, as Brunetto et al. (2007a) showed using their laser-ablated olivine samples together with a scattering model.

4.4.3. Q- and S-type asteroids

Q-type asteroids show spectra that are very similar to ordinary chondrite meteorites, thus fresh. Their spectra also show remarkable similarity to those of S-type asteroids. The difference is that the spectra of Q-type asteroids are brighter and have less steep slopes and deeper absorption bands than those of S-type asteroids. From earlier observations, Q-type asteroids are small and are mostly located in the near-Earth region. A transition between Q- and S-type asteroids has been observed for asteroid sizes between 0.1 and 5 km (Binzel et al. 2004). The accepted theory is that the surfaces of Q-type asteroids look fresh because they rejuvenate more easily than those of S-type asteroids. The main reasons may be that as they are smaller, their collisional lifetimes are shorter, and also their presence in the near-Earth region makes the tidal effects, including seismic shaking, more significant (Vernazza et al. 2009).

In Fig. 9 we can see that the Q-S distribution within the asteroid cloud is the same as the orientation of the fresh-irradiated distribution within both olivine and pyroxene samples. It is important to note that the positions of the asteroids in the principal component space are based on information regarding our measured spectra (not on information from the whole asteroid dataset) and still they cluster in a manner that agrees with the Q- to S-type transition.

Our PCA simulation thus verifies that there is not a large compositional difference in the S- and Q-type asteroids, and the variation in their spectral features can be associated with the different weathering stages. On the other hand, the PCA did not give any clue to whether there is a difference in the dominant space weathering agent between the Q- and S-type asteroids, as the directions of the different simulations are nearly parallel to the Q–S cloud. Based on this technique we are therefore unable to judge the history of the space environment of the individual bodies; in other words, we cannot say whether the body was subject to an environment with increased micrometeoroid flux or whether the weathering stage was caused mainly by solar wind ions.

S-type asteroid (433) Eros shows high albedo contrast (≈36%), but the slope variations are not as significant as we would expect during typical weathering circumstances (Clark et al. 2001; Murchie et al. 2002). An explanation may be that on the old surface of asteroid Eros, the spectral parameters of olivine are already saturated and the only variation present in the spectra is due to the changes in pyroxene, which take longer to propagate and are minor with respect to the spectral slope. Asteroid Itokawa, on the other hand, shows large spatial variation in the spectral slope. The spectra of Itokawa can in some parts of the surface be classified as Q-type and in other parts as S-type. The changes in the spectral slope on this asteroid suggest that the olivine spectral signatures are not yet saturated, as in the case of Eros, and that Itokawa may represent a younger surface. Slopes of Itokawa's spectra, however, are evaluated based on information relying on the incompletely captured 1 μm band (Abe et al. 2006; Hiroi et al. 2006; Koga et al. 2018).

4.5. Mid-infrared spectra

As mentioned in Sect. 3.4, the position of the Christiansen feature behaves inconsistently, shifting to the opposite direction, for olivine and pyroxene irradiated by laser. Lucey et al. (2017) evaluated the variation in the position of the Christiansen feature on the Moon and concluded that the feature shifts to longer wavelengths as the maturation process continues, which is in agreement with what we see in olivine and with what Weber et al. (2020) observed, and is in contrast to the previous work by Salisbury et al. (1997), who found that the Christiansen feature is not much affected by changes induced by space weathering.

Shifts in the position of the Christiansen feature are probably correlated with the visual albedo of the material, as noted by Lucey et al. (2017) and references therein. In a vacuum, the albedo influences the thermal gradient of the surface layer (Henderson & Jakosky 1997), which determines the depth from which the thermal emission originates and affects the Christiansen feature wavelength position (see also recent article by Lucey et al. 2021 for more details). However, albedo is probably not the only factor influencing the position of the Christiansen feature. For example, Lantz et al. (2017) pointed out that preferential loss of magnesium to Fe during the maturation process shifts the positions of the bands to longer wavelengths.

The possible reason for the inconsistency of the Christiansen feature shift between olivine and pyroxene may be the inappropriate spectral resolution. Different sampling of the spectral curves has an influence on the estimation of the Christiansen feature's position, as mentioned by Salisbury et al. (1991). Alternatively, a change in the position of the Christiansen feature is too small (of the order of a few per cent) to make a general conclusion based on it.

In Fig. 10 (bottom), we show that the relative intensities of the olivine reststrahlen bands at around 11 μm change as the irradiation proceeds because the shorter-wavelength band is altered more significantly than the longer-wavelength band. The same holds for pyroxene irradiated by laser. Similar changes in the relative intensities of the reststrahlen bands have already been observed, for example, by Brunetto et al. (2020). This evolution may be attributed to changes in the structure of the material or to changes in the preferred orientation of the crystals (see e.g. Weber et al. 2020).

We observed that the time needed to flatten the peaks of the restsrahlen bands differs for the different irradiation types. We should note that there is a dependence of the position of the reststrahlen bands on the observation geometry, as was reported by Rubino et al. (2020). In order to compare the asteroid observations to the laboratory data, one thus needs to make sure that the observational set-ups are the same.

4.6. Timescales

As already mentioned, if we compare the total energy density input of various irradiation techniques with the spectral change (see Fig. 4), at low energy densities laser causes greater changes than any of the ions. However, we did not evaluate the energy budget of individual processes that happen after irradiation and have the final effect on the spectra, so this result is only tentative.

If we consider the time needed to accumulate the same energy density through micrometeoroid impacts and through solar wind irradiation at 1 au, it is significantly longer for micrometeoroids (see Fig. 3). Looking, for example, at the changes in olivine, a 50% drop in albedo takes 1000 times longer by means of micrometeoroid impacts than by solar wind ions.

This result is consistent with previous laboratory work, which showed that the typical timescales of the significant spectral change are different: for the solar wind irradiation 10^4–10^6 yr, and for micrometeoroid bombardment 10^8–10^9 yr (Sasaki et al. 2001b; Noguchi et al. 2011; Blewett et al. 2011).

5. Conclusions

Our experiments revealed that the H^+ irradiation, simulating solar wind, and the laser pulses, simulating micrometeoroid impacts, induce spectral changes that are comparable in the VIS wavelength range, but there is a significant difference in their ability to influence longer NIR wavelengths. Laser pulses cause greater variation in the reflectance at longer wavelengths than any of the ions we used. This may be due to the greater penetration depth of the laser pulses when compared to the that of ions. For this reason, in the case of ions the material probed by the spectrometer is a mixture of a thin altered layer and the underlying unaltered layers, and the spectrum is thus less modified.

From the comparison of the total energy input of various irradiation techniques with the spectral change, the H^+ ions of the solar wind affect the surface on timescales three orders of magnitude shorter than the micrometeoroid impacts. We can thus make the following prediction: the spectrum of a fresh planetary surface will probably be altered in the first 10^5 yr mainly by the solar wind. It will therefore darken and significantly change its spectral slope (due to relatively smaller spectral change at longer NIR wavelengths). As the contribution of the micrometeoroid impacts increases for the older surfaces, the material will continue to darken, and as the long wavelengths are also altered, the spectral slope will not be modified to such an extent. By studying the NIR wavelength range, we can thus draw conclusions on the surface exposure ages of various different geomorphological features in the solar system bodies.

Except for the above-mentioned difference between ion and laser irradiation timescales and slope behaviour, we did not find any major dissimilarities in their effect on spectral evolution. It seems that the initial mineralogy is the leading factor influencing how the spectra will be affected regardless of the space weathering agent. In other words, all types of irradiation cause similar changes to the spectra of the given mineral, but for olivine, the evolution of the spectral curves is different to that of pyroxene.

While olivine shows prominent rapid changes in all spectral parameters in the VIS–NIR range, in the case of our pyroxene samples, we observed a slower response with only minor changes of the spectral slope compared with the magnitude of change in olivine. This may further contribute to the different slope behaviour of olivine-pyroxene mixtures (for instance Q- and S-type asteroids) on different timescales. In early phases, weathering of olivine shows rapid and significant slope change together with darkening or 1 μm band depth change. Once olivine matures, the continuation of space weathering affects mainly pyroxene with related change in the albedo rather than in the spectral slope.

In the MIR region the shifts in the Christiansen feature minimum were opposite for olivine and pyroxene. We have seen that the relative intensities of the olivine reststrahlen bands change irrespective of the space weathering agent. In pyroxene the changes in relative intensities were caused mainly by laser irradiation; ion irradiation caused only a minor alteration.

Our results have significant implications for asteroid studies. For instance, the rapid changes of olivine's spectral slope observed during the H^+ irradiation explain the absence of A-type asteroids with flat or low spectral slopes. Our PCA results agree with the Q- to S-type asteroid transition.

Acknowledgements. We thank the following for their help with preparing the experiments: Arto Luttinen for supporting us with the pyroxene material, Yazhou Yang for the olivine material, Janko Trišić Ponce for helping with pellet preparations, Romain Maupin, Radoslaw Michallik, Joonas Wasiljeff, Anna Vymazalová, Roman Skála, Petr Mikysek, and Zuzana Korbelová for analyses leading to revelation of the contamination in olivine, and Jiří Pavlů and Viktor Johánek for the loan of equipment from their laboratories. We are also grateful to Jessica Sunshine for the discussion of MGM fits. The authors are grateful to the anonymous referee for careful reading of the paper and valuable suggestions and comments. This work was supported by the University of Helsinki Foundation and the Academy of Finland project nos 325805, 1335595 and 293975, and it was conducted with institutional support RVO 67985831 from the Institute of Geology of the Czech Academy of Sciences. The authors acknowledge funding from Charles University (Project Progres Q47). Part of the irradiation was performed using the INGMAR set-up, a joint IAS-CSNSM (Orsay, France) facility funded by the French Programme National de Planétologie (PNP), by the Faculté des Sciences d'Orsay, Université Paris-Sud (Attractivité 2012), by the French National Research Agency ANR (contract ANR-11-BS56-0026, OGRESSE), and by the P2IO LabEx (ANR-10-LABX-0038) in the framework Investissements d'Avenir (ANR-11-IDEX-0003-01).

References

Abe, M., Takagi, Y., Kitazato, K., et al. 2006, Science, 312, 1334
Beck, P., Pommerol, A., Thomas, N., et al. 2012, Icarus, 218, 364
Berthe, L., Bezaeva, N. S., Gattaceca, J., et al. 2011, J. Laser Appl., 23, 012006
Bhatt, M., Reddy, V., Schindler, K., et al. 2017, A&A, 608, A67
Binzel, R. P., Rivkin, A. S., Stuart, J. S., et al. 2004, Icarus, 170, 259
Blewett, D. T., Coman, E. I., Hawke, B. R., et al. 2011, J. Geophys. Res. Planets, 116, E02002
Boustie, M., Berthe, T., de Resseguier, T., & Arrigoni, M. 2008, 1st international symposium on Laser Ultrasonics (Montreal, France)
Bowey, J. E., Hofmeister, A. M., & Keppel, E. 2020, MNRAS, 497, 3658
Brucato, J. R., Strazzulla, G., Baratta, G., & Colangeli, L. 2004, A&A, 413, 395
Brunetto, R., & Strazzulla, G. 2005, Icarus, 179, 265
Brunetto, R., Vernazza, P., Marchi, S., et al. 2006, Icarus, 184, 327
Brunetto, R., de León, J., & Licandro, J. 2007a, A&A, 472, 653
Brunetto, R., Roush, T. L., Marra, A. C., & Orofino, V. 2007b, Icarus, 191, 381
Brunetto, R., Lantz, C., Ledu, D., et al. 2014, Icarus, 237, 278
Brunetto, R., Lantz, C., Nakamura, T., et al. 2020, Icarus, 345, 113722
Burns, R. G. 1970, Mineralogical Applications of Crystal Field Theory (Cambridge: Cambridge University Press), 83
Burns, R. G. 1989, Mineralogical Magazine, 53, 135
Burns, R. G., Huggins, F. E., & Abu-Eid, R. M. 1972, Moon, 4, 93
Chauvin, N., Dayras, F., Le Du, D., & Meunier, R. 2004, Nucl. Instrum. Methods Phys. Res. A, 521, 149
Chrbolková, K., Kohout, T., & Ďurech, J. 2019, Icarus, 333, 516
Clark, B. E., Lucey, P., Helfenstein, P., et al. 2001, Meteorit. Planet. Sci., 36, 1617
Clénet, H., Pinet, P., Daydou, Y., et al. 2011, Icarus, 213, 404
Cloutis, E. A., Gaffey, M. J., Jackowski, T. L., & Reed, K. L. 1986, J. Geophys. Res., 91, 11, 641
Cloutis, E. A., Sunshine, J. M., & Morris, R. V. 2004, Meteorit. Planet. Sci., 39, 545
Connolly, A. J., & VanderPlas, J. T. 2014, Statistics, Data Mining, and Machine Learning in Astronomy: a Practical Python Guide for the Analysis of Survey Data (Princeton: Princeton University Press), 289
Cruikshank, D. P., & Hartmann, W. K. 1984, Science, 223, 281
de León, J., Licandro, J., Duffard, R., & Serra-Ricart, M. 2006, Adv. Space Res., 37, 178
DeMeo, F. E., Binzel, R. P., Slivan, S. M., & Bus, S. J. 2009, Icarus, 202, 160
Demyk, K., Carrez, P., Leroux, H., et al. 2001, A&A, 368, L38
Demyk, K., d'Hendecourt, L., Leroux, H., Jones, A. P., & Borg, J. 2004, A&A, 420, 233
de Sanctis, M. C., Migliorini, A., Luzia Jasmin, F., et al. 2011, A&A, 533, A77
Fazio, A., Harries, D., Matthäus, G., et al. 2018, Icarus, 299, 240
Fiege, K., Guglielmino, M., Altobelli, N., et al. 2019, J. Geophys. Res. Planets, 124, 1084
Fulvio, D., Brunetto, R., Vernazza, P., & Strazzulla, G. 2012, A&A, 537, L11
Fulvio, D., Fuks Maron, L., Cires Perez, Y., Tahir, & Del Rosso, T. 2021, Icarus, 366, 114532
Gaffey, M. J. 2010, Icarus, 209, 564
Gaffey, M. J., Bell, J. F., Brown, R. H., et al. 1993, Icarus, 106, 573
Gillis-Davis, J. J., Gobi, S., Bradley, J. P., et al. 2018, Lunar Planet. Sci. Conf., 49 2051

Grün, E., Gustafson, B. A. S., Dermott, S., & Fechtig, H. 2001, Interplanetary Dust (Berlin: Springer)
Gusarov, A. V., & Smurov, I. 2005, J. Appl. Phys., 97, 014307
Han, H.-J., Lu, X.-P., Yang, Y.-Z., Zhang, H., & Mutelo, A. M. 2020, Res. Astron. Astrophys., 20, 129
Hapke, B. 1965, Ann. New York Acad. Sci., 123, 711
Hapke, B. 2001, J. Geophys. Res., 106, 10039
Henderson, B. G., & Jakosky, B. M. 1997, J. Geophys. Res., 102, 6567
Hiroi, T., Abe, M., Kitazato, K., et al. 2006, Nature, 443, 56
Huffman, D. R., & Stapp, J. L. 1971, Nat. Phys. Sci., 229, 45
Isaacson, P. J., & Pieters, C. M. 2010, Icarus, 210, 8
Jiang, T., Zhang, H., Yang, Y., et al. 2019, Icarus, 331, 127
Kaňuchová, Z., Baratta, G. A., Garozzo, M., & Strazzulla, G. 2010, A&A, 517, A60
Keller, L. P., & Berger, E. L. 2014, Ann. Meeting Meteor. Soc., 77, 5088
Khosrofian, J. M., & Garetz, B. A. 1983, Appl. Opt., 22, 3406
Kissel, J., & Krueger, F. R. 1987, Appl. Phys. Materials Sci. Processing, 42, 69
Koga, S. C., Sugita, S., Kamata, S., et al. 2018, Icarus, 299, 386
Kohout, T., Čuda, J., Filip, J., et al. 2014, Icarus, 237, 75
Kramer, G. Y., Besse, S., Dhingra, D., et al. 2011, J. Geophys. Res. Planets, 116, E00G18
Laczniak, D. L., Thompson, M. S., Christoffersen, R., et al. 2021, Icarus, 364, 114479
Lantz, C., & Brunetto, R. 2014, in Asteroids, Comets, Meteors, eds. K. Muinonen, A. Penttilä, M. Granvik, A. Virkki, G. Fedorets, O. Wilkman, & T. Kohout (USA: NASA), 305
Lantz, C., Brunetto, R., Barucci, M. A., et al. 2017, Icarus, 285, 43
Lazzarin, M., Marchi, S., Moroz, L. V., et al. 2006, ApJ, 647, L179
Loeffler, M. J., Dukes, C. A., & Baragiola, R. A. 2009, J. Geophys. Res. Planets, 114, E03003
Lucey, P. G., Greenhagen, B. T., Song, E., et al. 2017, Icarus, 283, 343
Lucey, P. G., Greenhagen, B., Donaldson Hanna, K., et al. 2021, J. Geophys. Res. Planets, 126, 2020JE006777
Marchi, S., Brunetto, R., Magrin, S., Lazzarin, M., & Gandolfi, D. 2005, A&A, 443, 769
Matsumoto, T., Tsuchiyama, A., Miyake, A., et al. 2015, Icarus, 257, 230
Matsuoka, M., Nakamura, T., Hiroi, T., Okumura, S., & Sasaki, S. 2020, ApJ, 890, L23
McKay, D. S. 1978, Lunar Planet. Sci. Conf., 2, 723
Moroz, L. V., Fisenko, A. V., Semjonova, L. F., Pieters, C. M., & Korotaeva, N. N. 1996, Icarus, 122, 366
Murchie, S., Robinson, M., Clark, B., et al. 2002, Icarus, 155, 145
Noguchi, T., Nakamura, T., Kimura, M., et al. 2011, Science, 333, 1121
Noguchi, T., Kimura, M., Hashimoto, T., et al. 2014, Meteor. Planet. Sci., 49, 188
Norton, O. R. 2002, The Cambridge Encyclopedia of Meteorites (Cambridge: Cambridge University Press)
Paillet, J., Brunetto, R., Barucci, M. A., Dotto, E., & Strazulla, G. 2003, AAS/Div. Planet. Sci. Meeting Abs., 35, 39.14
Penttilä, A., Martikainen, J., Gritsevich, M., & Muinonen, K. 2018, J. Quant. Spectr. Rad. Transf., 206, 189
Penttilä, A., Väisänen, T., Markkanen, J., et al. 2020, Icarus, 345, 113727
Perez, D., & Lewis, L. J. 2003, Phys. Rev. B, 67, 184102
Pieters, C. M., & Noble, S. K. 2016, J. Geophys. Res. Planets, 121, 1865
Pieters, C. M., Taylor, L. A., Noble, S. K., et al. 2000, Meteorit. Planet. Sci., 35, 1101
Pieters, C. M., Ammannito, E., Blewett, D. T., et al. 2012, Nature, 491, 79
Quadery, A. H., Pacheco, S., Au, A., et al. 2015, J. Geophys. Res. Planets, 120, 643
Rommel, D., Grumpe, A., Felder, M. P., et al. 2017, Icarus, 284, 126
Rubino, S., Lantz, C., Baklouti, D., et al. 2020, Planet. Sci. J., 1, 61
Salisbury, J. W., Daria, D. M., & Jarosewich, E. 1991, Infrared (2.08-14 micron) spectra of powered stony meteorites, a Bibliography of Planetary Geology and Geophysics Principal Investigators and their Associates (USA: NASA), 1990
Salisbury, J. W., Basu, A., & Fischer, E. M. 1997, Icarus, 130, 125
Sanchez, J. A., Reddy, V., Nathues, A., et al. 2012, Icarus, 220, 36
Sanchez, J. A., Reddy, V., Kelley, M. S., et al. 2014, Icarus, 228, 288
Sasaki, S., Nakamura, K., Hamabe, Y., Kurahashi, E., & Hiroi, T. 2001a, in Lunar and Planetary Science Conference, Lunar. Planet. Sci. Conf., 32 1610
Sasaki, S., Nakamura, K., Hamabe, Y., Kurahashi, E., & Hiroi, T. 2001b, Nature, 410, 555
Sasaki, S., Hiroi, T., Nakamura, K., et al. 2002, Adv. Space Res., 29, 783
Schwenn, R. 2000, Solar Wind: Global Properties, ed. P. Murdin (Bristol: IOP Publishing Ltd), 2301
Shirk, M. D. 1999, Retrospective Theses and Dissertations, 12483, Iowa State University, USA
Sunshine, J. M., Pieters, C. M., & Pratt, S. F. 1990, J. Geophys. Res., 95, 6955
Sunshine, J. M., Pieters, C. M., Pratt, S. F., & McNaron-Brown, K. S. 1999, Lunar Planet. Sci. Conf., 30, 1306
Sunshine, J. M., Bus, S. J., Corrigan, C. M., McCoy, T. J., & Burbine, T. H. 2007, Meteor. Planet. Sci., 42, 155
Vernazza, P., Brunetto, R., Strazzulla, G., et al. 2006, A&A, 451, L43
Vernazza, P., Binzel, R. P., Rossi, A., Fulchignoni, M., & Birlan, M. 2009, Nature, 458, 993
Vernazza, P., Fulvio, D., Brunetto, R., et al. 2013, Icarus, 225, 517
Weber, I., Stojic, A. N., Morlok, A., et al. 2020, Earth Planet. Sci. Lett., 530, 115884
Wehner, G. K., Kenknight, C. E., & Rosenberg, D. 1963, Planet. Space Sci., 11, 1257, IN1, 1259
Yamada, M., Sasaki, S., Nagahara, H., et al. 1999, Earth Planets Space, 51, 1265
Yang, Y., Zhang, H., Wang, Z., et al. 2017, A&A, 597, A50
Zeidler, S., Posch, T., Mutschke, H., Richter, H., & Wehrhan, O. 2011, A&A, 526, A68
Ziegler, J. F., & Biersack, J. P. 1985, The Stopping and Range of Ions in Matter (Berlin: Springer), 93

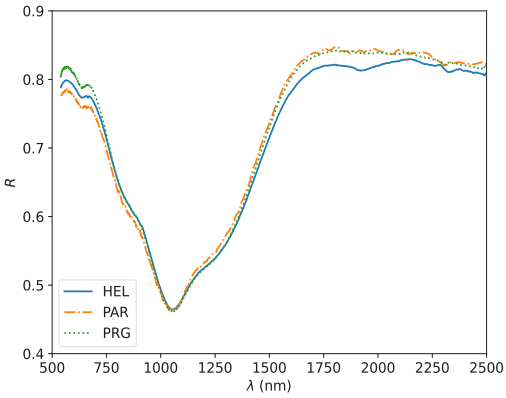

Fig. A.1. Comparison of fresh olivine spectra measured on different spectrometers. Reflectance is marked by R, wavelength by λ, HEL indicates the University of Helsinki laboratories, PAR indicates the INGMAR set-up at IAS-CSNSM in Orsay, and PRG indicates the laboratories at Charles University in Prague.

Appendix A: Experimental set-up

Our spectral measurements were made using three different spectrometers, with varying observation geometries; in one case we used the integrating sphere, and in the other two cases we measured with fixed incidence and collection angles, in each case slightly differently (see Table 1 for more details). We did not apply any corrections to the spectra to equalize the observation circumstances. There are two main reasons for this. Firstly, in the majority of cases we were comparing spectra with their fresh analogue measured with the same spectrometer. The relative trends thus did not suffer from the lack of correction. Secondly, as Beck et al. (2012) showed, in the case of the Moon the difference between the spectral slope measured at a phase angle of 15° and 30° (our situation) is only a few percentage points, which is within the limits of our error bars. In addition, Sanchez et al. (2012) pointed out that in their sample of 12 Q- and S-type asteroids, there needs to be a change in phase angle of about 90° to obtain spectral changes similar to those of the space weathering effects.

Additionally, the integrating sphere spectrometer we used has a port in the sphere in the specular direction. The port can be closed with a PTFE-coated plate or opened with a beam trap attached to the port. In our spectral measurement we always used the configuration with the beam trap in the specular direction to avoid specular reflectance that would affect the measurements. A comparison of measurements of a fresh olivine pellet on different spectrometers can be seen in Fig. A.1. We can see that the difference is indeed only a few percentage points.

Even though there were slight variations in the wavelength ranges of individual spectrometers and some spectrometers could provide information for a wider wavelength range, for the final evolution we used those spectral ranges that were covered by all the set-ups. For the VIS–NIR spectra we worked from 540 to 2 500 nm and for the MIR spectra from 3 to 13 µm.

Appendix B: Notes on contamination

The rock samples we used for the experiments were terrestrial minerals. Compared with the space environment, some contamination is possible even with strict experimental handling, which includes cleaning the equipment using ethanol or deionized water, wearing gloves, and covering the samples during processing to protect them from the airborne dust.

The OPX samples contained pargasite, as said in the main text, which we accounted for. Otherwise the OPX samples were pure, but in the case of olivine we saw some sort of contamination in the form of darker grains. Even in the MIR wavelength range, at around 3 400 nm, we found several peaks. These peaks belong to organic material, most probably hydrocarbons and carboxylic acids, that may originate from terrestrial dust (Salisbury et al. 1991).

Analysing the samples using a scanning electron microscope (Tescan, Vega 3 XMU) with the energy dispersive spectroscopy method, we found that the majority of the contamination was a chromium-rich spinel (most probably chromite). Nevertheless, Cloutis et al. (2004) and Isaacson & Pieters (2010) showed that chromite is a common mineral in the solar system; it is usually found together with olivines in meteorites, in S- and K-type asteroids, and in lunar samples.

Based on X-ray diffraction measurement, we conclude that the contamination is less than 4 % (limit of reliability of the measurement), and the contamination thus has only a minor effect on our results. To give more precise numbers, by a comparison with the uncontaminated sample we estimated that the absolute spectral difference between contaminated and uncontaminated material is less than 3% in the area up to 650 nm and is even smaller at longer wavelengths. Among six fresh olivine pellets, the albedo varies by 1.7%, the strength of the absorption bands varies by less than 5%, and the positions of the minima of the bands do not change.

Chromite's spectrum is generally darker than the spectrum of olivine, and has absorptions around 2 µm (see e.g. Cloutis et al. 2004, Fig. 12). We do not see any alteration of the olivine spectrum around 2 µm, which is in contrast to Cloutis et al. (2004), who pointed out that spectral differences of olivine and chromite allow the detection of even small abundances of chromite in olivine. The effect of the contamination on the spectra is thus minor.

Appendix C: Timescales

Considering the ion irradiation experiments, the following estimates of the astrophysical timescales are a proxy for the situation at 1 au. If we wanted to evaluate the experiments, for example, in the main asteroid belt, the timescales would obviously be longer, as the flux of the solar wind ions would be smaller, as it decreases approximately with the square of the distance from the Sun (Schwenn 2000). We also use numbers valid for the typical situation in the solar system, which is the slow solar wind. In the case of solar wind flares, the fluxes and energies of the particles would be different. It should be noted that compared with the real solar wind, the energies of our ions were slightly higher, which means that our timescales should be taken as order of magnitude estimates rather than exact values. On the other hand, the relative values belonging to one type of irradiation are valid.

To calculate what timescales the irradiation fluences of ions corresponds to, we need to compare the experimental values with the typical fluxes of the individual ions. Based on Schwenn (2000) the flux of protons at 1 au is $\approx 2.9 \times 10^8$ ions/cm^2/s. If we consider the ratio of H^+ to He^+ ions in the solar wind, we get a flux of 1.9×10^7 ions/cm^2/s for He^+. For Ar^+, we have 4×10^2 ions/cm^2/s (Kaňuchová et al. 2010). By dividing our fluxes by the literature-based values, in the first approximation

we obtain the time that the material would be subject to irradiation at 1 au. To further improve the estimate, we approximate the object as a rotating sphere, in which case a correction factor of four is introduced into the calculation of the timescale. For bodies of other shapes the correction factor would be different, but this calculation is beyond the scope of our article and the relative trends we obtain in the first-approximation estimate are unaffected by the simplified solution.

Based on the number of individual pulses that were used during the laser irradiation, we can estimate the corresponding time the surface would experience a similar number of impacts at 1 au. The flux of dust particles several microns in size is, based on Sasaki et al. (2002) or Grün et al. (2001, page 194), $\approx 1 \times 10^{-4}$ m^{-2}s^{-1}. The calculation is then similar to the case of ions. The spot size of the laser beam was several times larger than these particles, so the corresponding timescale is probably the lower limit.

Appendix D: Amorphization

In Fig. 4 we can see that the spectral changes caused by various ions are similar. However, the trend representing H^+-irradiated olivine significantly deviates from the trends given by heavier ions at an energy density of about 100 J/cm^2. Our assumption is that the surface of the pellet exposed to the H^+ irradiation was subject to collapse of the crystalline structure (i.e. amorphization of the material).

If we compare our set-up with that of Brucato et al. (2004), who studied crystal–amorphous changes of forsterite samples in IR spectroscopy due to H^+, He^+, carbon, and Ar^{++} irradiation, we see that all our samples should be amorphized to a certain level. Demyk et al. (2001) also did He^+ irradiation of crystalline olivine. They found that even at the lowest used fluence (5×10^{16} ions/cm^2, using 4 and 10 keV ions), layers of several tens of nanometres amorphized. It is thus probable that all our samples have some fraction of the volume amorphized, but only H^+-induced trends show a significant break. The reason for this may be that the different ions cause different amorphization levels. As Demyk et al. (2004) pointed out, low-energy light ions and high-energy heavy ions have the greatest ability to amorphize silicates. Other combinations of energies and types of ions lead to the alteration of only a thin surface layer, whose contribution to the spectrum would only be minor. An interplay between the penetration depths of different ions (see Table 2) and the thickness of the sample (size of the particles on the surface) can also influence the amorphization because, as noted by Demyk et al. (2004), the maximum damage happens at the penetration depth of the ions. If the grain is smaller than the penetration depth, it will show less damage than if the grain is larger.

Brunetto & Strazzulla (2005) and Brunetto et al. (2014) pointed out that the spectral changes relate to the nuclear elastic dose (i.e. the number of vacancies per cm^2). We thus plotted a similar graph to Brunetto et al. (2014, Fig. 8). The dependence of the slope of the 1 µm band, defined similarly to Lazzarin et al. (2006) and calculated as a linear continuum from 540 to 920 nm of the spectra normalized at 550 nm, on the number of vacancies per cm^2 can be seen in Fig. D.1. Additionally, we estimated the slopes for the work of Loeffler et al. (2009) and Lantz et al. (2017). Loeffler's spectra were measured from $\approx$ 650 nm. In that case the spectral slope is calculated from this shifted value and may thus be a bit offset.

We can see that He^+ and Ar^+ irradiation show similar behaviour to that estimated from spectra in Loeffler et al. (2009) and Lantz et al. (2017). It seems that the slope correlates with the number of vacancies and that for a high number of vacancies both types of irradiation reach an asymptotic value. On the other hand, our H^+ irradiation reaches very high and significantly different values of the spectral slope even at a low number of vacancies. Even this figure thus points to the distinct behaviour of the most H^+-irradiated spectra. A complete understanding of the processes causing this discrepancy however requires transmission electron microscopy analyses and should be the subject of future work.

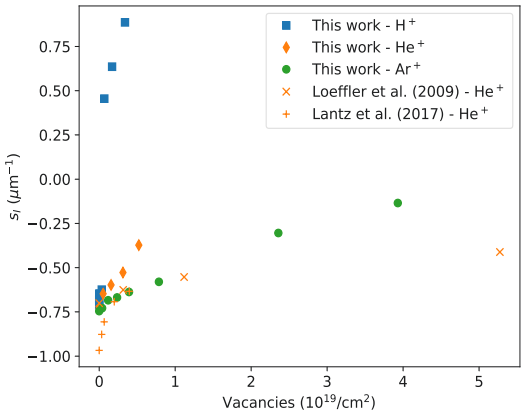

Fig. D.1. Slope of 1 µm band in olivines (s_I) as a function of the number of vacancies per cm^2 (taken from Table 2). The values of spectral slopes for the cited work are only estimations. H^+ stands for hydrogen, He^+ for helium, and Ar^+ for argon ions.

Appendix E: Ratios of mid-infrared spectra

Here we present ratios of irradiated and fresh MIR spectra affected by different irradiation types (see Fig. E.1). For both materials there is not a big change in the region up to 8 µm. At longer wavelengths, changes in the positions, shapes, and intensities of the bands are obvious from the ratios.

The reason for this behaviour may be the different scattering regime in these two regions of the spectra. Spectral features at shorter wavelengths than the Christiansen feature originate from the volume scattering, while features at the longer wavelengths, the reststrahlen bands, are caused by the surface scattering regime (Salisbury et al. 1991).

The difference at the shorter wavelengths of spectra of pyroxene irradiated by laser and by all other ions may thus be explained in the same manner as in the main text, that is by penetration depth (see Sect. 4.2). On the other hand, in the reststrahlen bands we obtain all the irradiation information from irradiated layers exclusively. (See the main text, Sects. 3.4 and 4.5, for a deeper evaluation of the changes in the reststrahlen bands.)

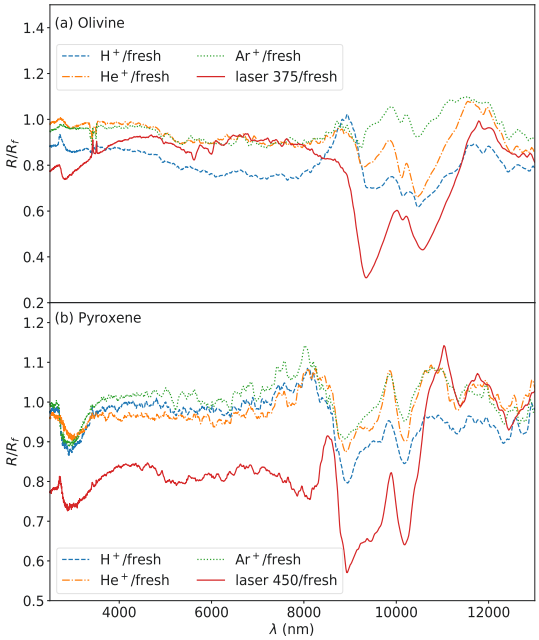

Fig. E.1. Ratios of reflectance (R) of irradiated to fresh (f) spectra of olivine (OL) and pyroxene (OPX). λ stands for wavelength. For ion irradiation, the spectra with the highest irradiation were always used. For laser irradiation, we plotted the ratios using the 375 J/cm^2 (OL) and 450 J/cm^2 (OPX) cases, as they represent similar energy densities. H^+ stands for hydrogen, He^+ for helium, and Ar^+ for argon ions.

Paper III

Chrbolková, K., Halodová, P., Kohout, T., Ďurech, J., Mizohata, K., Malý, P., Dědič, V., Penttilä, A., Trojánek, F., and Jarugula, R.

Sub-surface alteration and related change in reflectance spectra of space-weathered materials.

Astronomy & Astrophysics, 2022, 665, A14.

A&A 665, A14 (2022)
https://doi.org/10.1051/0004-6361/202243282

Astronomy & Astrophysics

Sub-surface alteration and related change in reflectance spectra of space-weathered materials

Kateřina Chrbolková[1,2,3], Patricie Halodová[4], Tomáš Kohout[1,3], Josef Ďurech[2], Kenichiro Mizohata[5], Petr Malý[6], Václav Dědič[7], Antti Penttilä[8], František Trojánek[6] and Rajesh Jarugula[4]

[1] Department of Geosciences and Geography, PO Box 64, 00014 University of Helsinki, Helsinki, Finland
e-mail: katerina.chrbolkova@helsinki.fi
[2] Astronomical Institute, Faculty of Mathematics and Physics, Charles University, V Holešovičkách 2, 18000 Prague, Czech Republic
[3] Czech Academy of Sciences, Institute of Geology, Rozvojová 269, 16500 Prague, Czech Republic
[4] Research Centre Řež, Hlavní 130, 250 68 Husinec–Řež, Czech Republic
[5] Department of Physics, PO Box 43, 00014 University of Helsinki, Helsinki, Finland
[6] Department of Chemical Physics and Optics, Faculty of Mathematics and Physics, Charles University, Ke Karlovu 3, 12116 Prague, Czech Republic
[7] Institute of Physics, Faculty of Mathematics and Physics, Charles University, Ke Karlovu 5, 12116 Prague, Czech Republic
[8] Department of Physics, PO Box 64, 00014 University of Helsinki, Helsinki, Finland

Received 8 February 2022 / Accepted 22 June 2022

ABSTRACT

Context. Airless planetary bodies are studied mainly by remote sensing methods. Reflectance spectroscopy is often used to derive their compositions. One of the main complications for the interpretation of reflectance spectra is surface alteration by space weathering caused by irradiation by solar wind and micrometeoroid particles.
Aims. We aim to evaluate the damage to the samples from H^+ and laser irradiation and relate it to the observed alteration in the spectra.
Methods. We used olivine (OL) and pyroxene (OPX) pellets irradiated by 5 keV H^+ ions and individual femtosecond laser pulses and measured their visible (VIS) and near-infrared (NIR) spectra. We observed the pellets with scanning and transmission electron microscopy. We studied structural, mineralogical, and chemical modifications in the samples. Finally, we connected the material observations to changes in the reflectance spectra.
Results. In both minerals, H^+ irradiation induces partially amorphous sub-surface layers containing small vesicles. In OL pellets, these vesicles are more tightly packed than in OPX ones. Any related spectral change is mainly in the VIS spectral slope. Changes due to laser irradiation are mostly dependent on the material's melting temperature. Of all the samples, only the laser-irradiated OL contains nanophase Fe particles, which induce detectable spectral slope change throughout the measured spectral range. Our results suggest that spectral changes at VIS–NIR wavelengths are mainly dependent on the thickness of (partially) amorphous sub-surface layers. Furthermore, amorphisation smooths micro-roughness, increasing the contribution of volume scattering and absorption over surface scattering.
Conclusions. Soon after exposure to the space environment, the appearance of partially amorphous sub-surface layers results in rapid changes in the VIS spectral slope. In later stages (onset of micrometeoroid bombardment), we expect an emergence of nanoparticles to also mildly affect the NIR spectral slope. An increase in the dimensions of amorphous layers and vesicles in the more space-weathered material will only cause band-depth variation and darkening.

Key words. methods: laboratory: solid state – methods: data analysis – techniques: spectroscopic – planets and satellites: surfaces – solar wind – meteorites, meteors, meteoroids

1. Introduction

Reflectance spectroscopy of planetary surfaces enables the determination of the mineralogy and physical state of airless planetary surfaces (see, for example, Burns 1989). Planetary spectra contain complex information as they are influenced by multiple additional factors, including temperature, the roughness of the surface, or the space weathering state. In this article, we focus on how space weathering influences planetary materials at the microscale and what consequences it has for the spectra. Such knowledge is crucial for the correct interpretation of spectroscopic observations.

Space weathering is caused by two major processes – solar wind irradiation and micrometeoroid bombardment – which alter the topmost layers of planetary surfaces (Hapke 1965, 2001; Wehner et al. 1963). As a result, the spectra of silicate-rich bodies darken, the spectral contrast decreases, and the visible (VIS) and near-infrared (NIR) slopes increase (reddening of the spectra), as documented, for example, by Hapke (2001), Pieters et al. (2000), and Pieters & Noble (2016). Other processes that influence the space weathering state are, for example, galactic radiation, sublimation, and mixing with the material of impactors, but these were not identified as the main drivers of space weathering change in previous studies of the Moon and of near-Earth asteroids (Pieters & Noble 2016).

Earlier studies reported on the sub-surface changes related to space weathering, especially changes due to solar-wind sputtering and impact melting with associated vaporisation and vapour

redeposition. Already in the lunar samples from the Apollo missions, Keller & McKay (1993, 1997) observed thin, 200 nm, amorphous rims with randomly dispersed inclusions of Fe metal, which they identified as the solar wind irradiation products. Since then, so-called nanophase Fe ($npFe^0$) particles have been identified in many laboratory simulations (see, for example, Fazio et al. 2018; Weber et al. 2020; Wu et al. 2017) and also in samples from asteroid (25143) Itokawa (Noguchi et al. 2014a,b) and the Moon (Kling et al. 2021). Other abundant types of structures in the altered sub-surface layers are vesicles and blisters, as documented, for example, by Dobrică & Ogliore (2016) and Matsumoto et al. (2015) for Itokawa particles.

Because of the sparsity of the natural samples and the slow natural evolution of space weathering, a significant part of our understanding comes from laboratory experiments. The effect of the solar wind is usually simulated by irradiation of the samples by various ions (see, for example, the work of Brunetto et al. 2014; Demyk et al. 2001; Hapke et al. 1970, or Loeffler et al. 2009 for more details). The effect of micrometeoroid impacts is mainly studied using individual or repeated laser pulses of various durations and energies (see, for example, Sasaki et al. 2001, 2002, and Yamada et al. 1999 for usage of nanosecond laser pulses or Fazio et al. 2018 and Chrbolková et al. 2021 for femtosecond laser pulses). Only rarely do experiments include actual impacts of dust particles, such as in Fiege et al. (2019).

This article is a follow-up of Chrbolková et al. (2021), where we evaluated the difference in the spectra influenced by solar-wind irradiation and micrometeoroid bombardment. This was done through laboratory irradiations of olivine and pyroxene pellets using low-energy 5 keV H^+ ions and individual femtosecond laser pulses as in Fazio et al. (2018). We found that there was a difference in the influence of the two types of irradiation on NIR wavelengths; the laser influenced VIS and the NIR range, while ion irradiation had only a mild effect in the NIR wavelength range. However, in general, the spectral evolution was determined more by the original mineralogy of the samples than by the space weathering agent. This result agreed with earlier observations of Sasaki et al. (2002).

In Chrbolková et al. (2021), we only evaluated the spectral change, but we did not have information on the material changes within the pellets. In this article, we aim to find the connection between the spectral changes and the sub-surface alteration caused by the different space weathering agents.

2. Methods

2.1. Samples, irradiations, and spectroscopy

We used samples identical to those in Chrbolková et al. (2021), that is pellets made of a pressed powder (with particle sizes < 106 µm) of olivine (forsterite number Fo90), further denoted as OL, and pyroxene (enstatite number En67), further denoted as OPX, on top of a KBr base. We refer the reader to Chrbolková et al. (2021) for more details.

For the microscopical observations, we used four different irradiated pellets from Chrbolková et al. (2021). Two of them were produced by H^+ irradiation, and the other two by femtosecond laser irradiation. In each case, one OL and one OPX pellet were selected.

The H^+-irradiation was done using 2×10^{17} H^+ cm^{-2} 5 keV ions. The ion beam covered the whole 13-mm pellet and was oriented perpendicularly to the surface of the pellet. Samples were placed in a vacuum chamber with a pressure of $\approx 10^{-7}$ mbar during the irradiations.

A femtosecond laser was set to shoot individual, spatially separated 800-nm pulses perpendicularly to the surface of the pellet. The duration of one pulse was 100 fs, and for the OL sample the energy of one pulse corresponded to 1.5 mJ, while for OPX it was 1.8 mJ. The laser spot on the surface of the pellet was ≈ 50 µm in diameter. The pressure in the vacuum chamber was $\approx 10^{-4}$ mbar. For microscopic observations, we selected pellets in which the spatial separation of the individual laser-induced microcraters was the largest possible so that we were sure that the studied crater is not influenced by the neighbouring craters, that is OL irradiated by 1.7 mJ cm^{-2} (equivalent crater distance 300 µm) and OPX irradiated by 1.5 mJ cm^{-2} (200 µm).

To compare the spectral evolution with the observed microstructures, we used spectra measured in Chrbolková et al. (2021). The H^+-irradiated spectra were measured using an OL-750 automated spectroradiometric measurement system by Gooch & Housego with polytetrafluoroethylene (VIS) and gold (NIR) standards and an incident angle of 10° (Chrbolková et al. 2021; Penttilä et al. 2018). The laser-irradiated spectra were measured using a Vertex 80v from Bruker with an A513/Q variable angle reflection accessory using the Spectralon standard, an incident angle of 0°, and a collection angle of 30°. As we only compared relative trends within one dataset, the differences in the experimental set-up do not inhibit further interpretation.

A straightforward visualisation of the spectral change is the ratio plot of the weathered to fresh material. For H^+ irradiation, we used the ratio plot for the 2×10^{17} H^+ cm^{-2} case, which exactly matched the samples studied here with the microscope. For laser irradiation, we studied individual craters. To obtain a representation of the spectrum of one crater, which is too small to be captured by our spectrometer, we selected a spectrum captured over a surface homogeneously covered by craters that lie tightly next to each other but do not overlap. Based on microscopical observations, the craters are approximately 100 µm in diameter; we thus selected spectra of the pellet in which the centres of the craters were 100 µm apart. These spectra were influenced by the unaltered material located in the corners of the squares circumscribed to the craters, but its contribution was smaller than that from the irradiated material.

2.2. New analyses

Using the pellets described in the previous section, we carried out the following analyses to study the surface structures related to space weathering: scanning electron microscopy (SEM) using secondary electrons (SEM-SE) for morphology, backscattered electrons (SEM-BSE), and energy-dispersive X-ray analysis (SEM-EDS) for compositional information. For sub-surface structures, we used transmission electron microscopy (TEM) in conventional (CTEM), high-resolution (HR-TEM), and scanning (STEM) modes combined with EDS for compositional information.

2.2.1. Scanning electron microscopy

A Tescan Lyra 3GMU Dual-Beam Scanning Electron Microscope equipped with a field emission gun (FEG) and focused Ga ion beam was used for SEM and in situ lift-out of the lamellae dedicated to TEM analysis. The pellet samples were coated with carbon prior to the electron microanalysis to prevent charging.

The samples were at first characterised with top-view SEM and EDS imaging. The SEM operational conditions were as

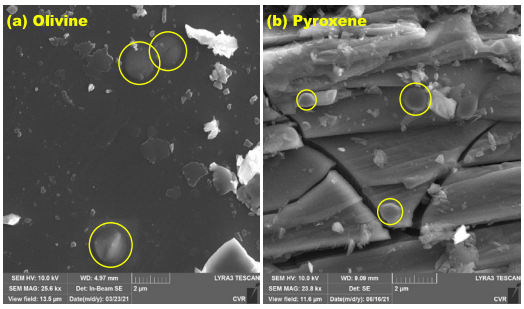

Fig. 1. Blisters (highlighted with yellow circles) created by H^+ irradiation. Top view of (*a*) olivine and (*b*) pyroxene surface captured by scanning electron microscopy. The scale bar in both figures corresponds to 2 µm.

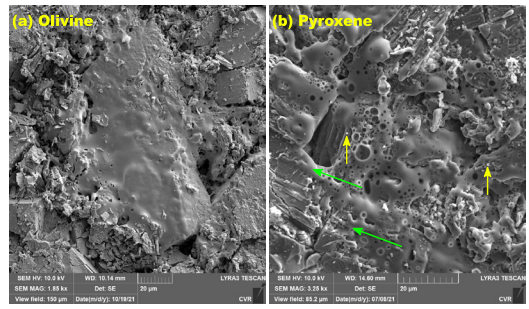

Fig. 2. Scanning electron microscopy images (top view) of one individual crater in the (*a*) olivine and (*b*) pyroxene sample. The centre of each crater is approximately in the middle of the image. The craters lie in the molten areas in both figures, but marking the border of them would be highly inaccurate. The scale bar in both figures corresponds to 20 µm. The yellow arrows point to melt drops, and the green arrows show examples of melt splashes.

follows: i) surface imaging conditions – accelerating voltage of 10 kV, 5–9 mm working distance, SE or in-beam SE imaging modes; ii) analytical conditions – accelerating voltage of 15 kV, 9 mm working distance, SE, and BSE imaging modes. Chemical analysis was carried out using an EDS system composed of an 80 mm^2 X-Max^N Oxford Instruments Silicon Drift Detector and Oxford Instruments AZtec acquisition and processing software.

After the SEM characterisation, thin lamellae for subsequent TEM were prepared by focused ion beam milling. To avoid charging and drifting during the ion preparation, the non-conductive pellets were coated with a 100 nm layer of gold. Thin, cross-sectional specimens were extracted from the regions of interest of the pellet samples with the use of an OmniProbe OP400 nanomanipulator and attached to a copper grid for further ion thinning and polishing to electron transparency (<100 nm thickness). The protective Pt strip was deposited on the surface at the area of interest before the milling process to prevent Ga^{2+} ion beam damage of the laser- and H^+-irradiated sample surface. The ion beam operational conditions were as follows: accelerating voltage of 30 kV and beam current of 2 nA for the trench milling, 500 pA for cross-section polishing, 160 pA for further thinning, and 10 kV and 40 pA for the final polishing steps to minimise the Ga ion damage of the thin lamellae.

2.2.2. Transmission electron microscopy

The CTEM, HR-TEM, and STEM investigations were carried out using a Jeol JEM 2200FS FEG microscope equipped with an Oxford Instruments Ultim Max TEM EDS system, which was used for the acquisition of elemental maps, line scans, point analysis and chemical quantification. The microscope was operated at 200 kV. TEM images were acquired using conventional imaging mode for the bright field (BF) and HR. In STEM, high-annular dark-field, BF, and dark-field detectors were used. Selected area diffraction patterns and HR images were captured on a TVIPS TemCam-XF416 4k × 4k CMOS camera.

Analyses with STEM-EDS were obtained using a spot size of 1 nm and integration time of 120 s. Acquisition of the EDS elemental maps had a typical duration of ≈ 30 min. Mapping and line scans were acquired using the AutoLock function for drift correction. The data were further processed using the AZtecTEM software, and deconvolution of the elements was solved using the Tru-Q technology. Factory standards (Oxford Instruments) were used for quantification. Quantitative analysis used background subtraction by filtered least-squares fitting (Statham 1977), and Cliff-Lorimer correction procedures were used for quantification. Unwanted peaks of non-sample elements (C, Cu, Co, Ga) were excluded for the purpose of quantitative analysis.

2.3. SRIM irradiation simulations

To support our observations from the H^+ irradiations, we conducted The stopping and range of ions matter (SRIM; Ziegler & Biersack 1985) simulations using 1000 5 keV H^+ ions propagating through the OL and OPX materials with compositions matching our samples. We focused on ion penetration depths and also on the distribution of the collision events in the samples to correlate these with the distribution of the disturbances in the samples.

3. Results

3.1. Surface changes

All four samples show visible darkening of their irradiated surfaces. The OL and OPX irradiated by H^+ ions do not show major changes in surface morphology. The only visible alteration in the SEM images is in the form of blisters, which are more frequently found in the OPX than in the OL, where the blisters are observed only rarely (see Fig. 1). We estimated that the size of the blisters is ≈1.7 µm in the OL, while in the OPX it is ≈0.9 µm. The morphology of the two surfaces differs, which could have influenced the blister size.

Considering the laser-irradiated samples, the surface changes are more extensive, as expected. We observe extensive melting in the area of the crater. In the OL, melting is restricted to the area of the crater and the melt is smooth with a minor amount of bubbles and depressions after gas release. In the OPX, the melting is more pronounced, and we also see melt splashes and melt drops (see Fig. 2). The bubble-rich melted layer often encompasses large continuous areas of the sample surface, and it is more difficult to identify individual craters.

Maps of irradiated surfaces from SEM-EDS (Fig. 3) do not show any measurable spatial variation in the composition related to the space weathering experiments. The only visible features are linear structures in one OPX sample related to terrestrial weathering (amphiboles).

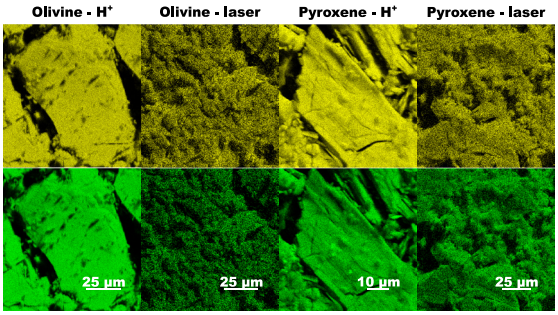

Fig. 3. Maps of two selected elements from scanning electron microscopy using energy dispersive X-ray analysis. Si is in yellow (*top row*), and Mg is in green (*bottom row*).

3.2. Sub-surface changes

The images of H^+-irradiated samples from TEM reveal radiation damage with abundant vesicles in thin altered layers. In the OL, the influenced layer is approximately 200 nm thick, while in the OPX it is approximately 150 nm thick (see Figs. 4a, b). The two samples differ also in the size and abundance of the vesicles. In the OL, the vesicles are in multiple, tightly packed layers. Their shape is elongated, with a size of approximately 10×50 nm (longer side parallel to the surface). In the OPX, the vesicles are more spherical and less abundant, with sizes of approximately 20 nm.

Diffraction patterns of the sub-surface layers show that the crystalline structure is extremely damaged and in both cases contains fully amorphous areas. We refer to such a structure as a partially amorphous layer.

Laser-irradiated OL and OPX samples differ significantly from each other. While the OL sample is the only one in which we identify Fe nanoparticles ($npFe^0$, 7–10 nm in diameter), the OPX sample is characterised by a huge number of vesicles with sizes ranging from several nm to 2 µm and no nanoparticles (see Fig. 4c, d). In the OL, the completely amorphous surface layer is approximately 300 nm thick, and the nanoparticles are directly below it concentrated in a thin irregular zone. The thickness of the fully amorphous layer in the OPX is typically around 400 nm but it significantly varies and can reach up to 2.5 µm in some extreme cases. Tiny black dots in the TEM image of the OPX irradiated by laser represent redeposited particles of Pt and Au that we used for imaging and extraction of the thin section for TEM analyses (see Fig. 4 d).

In Fig. 5, we show the ratio of irradiated to fresh spectra of the samples, as described in Sect. 2.1. Spectral ratios of the OL and OPX irradiated by H^+ show similar behaviour, that is a strong decrease of the albedo at shorter wavelengths (resulting in an increase of the spectral slope) and nearly no change at longer wavelengths. The spectrum of the laser-irradiated OL also behaves similarly but shows additional changes in the NIR slope. In contrast, spectra of the laser-irradiated OPX do not show changes in spectral slope, although darkening and enhancement of mineral absorption bands are observed.

In Fig. 6, we show depth profiles of the chemical composition of all four samples. All the samples show a similar change – depletion of Mg and enrichment of Si within the sub-surface amorphous and partially amorphous zones compared to the unaltered part of the sample. This trend is more pronounced in the OL samples. This happens at ≈250 nm for H^+ irradiation and at ≈800 nm for laser irradiation. The composition is stabilised as we approach underlying unaltered areas. The depths below which the composition does not change significantly are as follows: ≈350 nm and 1000 nm for H^+- and laser-irradiated OL, respectively, and ≈180 nm and 900 nm for H^+- and laser-irradiated OPX, respectively. In general, the influenced layer in the OL is always slightly thicker than in the OPX irradiated by

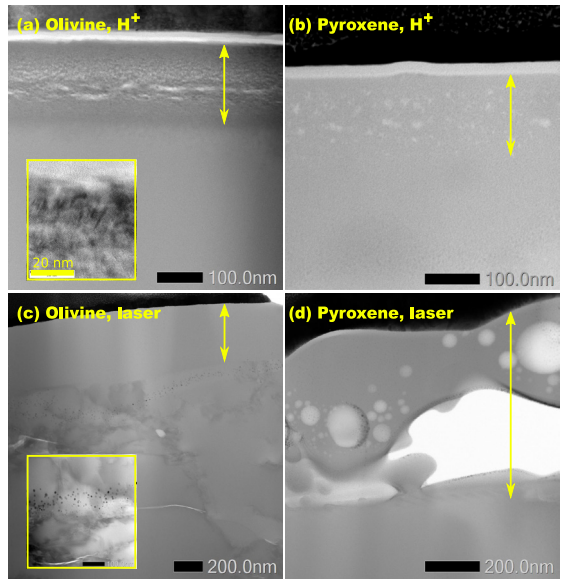

Fig. 4. Bright-field scanning transmission electron microscopy images of the lamellae of all samples. Inset in (*a*) is the high-resolution transmission electron microscopy image of the altered layer in the H^+-irradiated sample. Inset in (*c*) is the zoomed-in picture of the area containing nanophase Fe particles. Double-headed arrows mark the areas that are partially or fully amorphised.

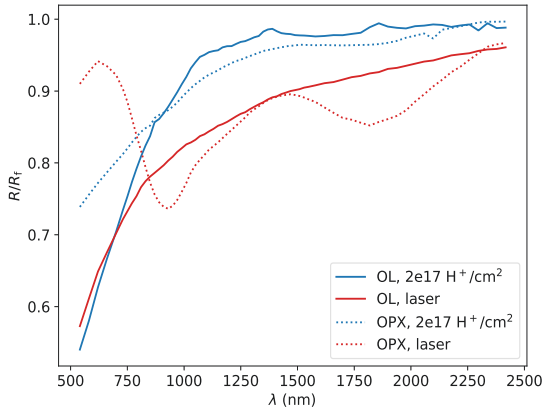

Fig. 5. Ratio of mature to fresh spectra of our samples. R stands for the reflectance, R_f for reflectance of the fresh material, and λ for wavelength. Laser-irradiated spectra were measured on samples in which the craters were 100 µm apart. The OPX absorption bands lie at ≈930 nm and 1820 nm in the un-irradiated spectra; see Chrbolková et al. (2021) for comparison.

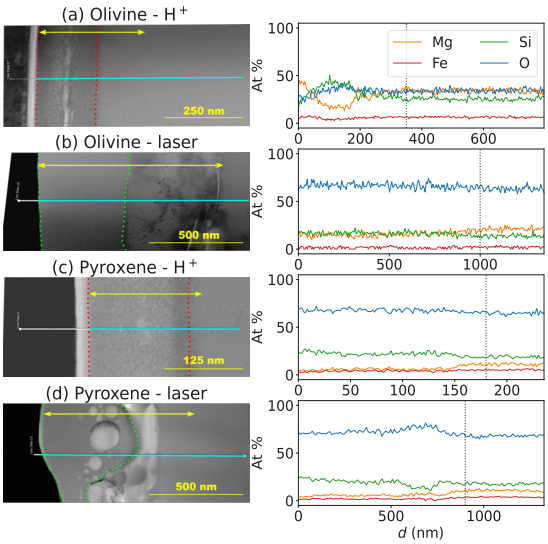

Fig. 6. Composition variation in the sub-surface layers. Sample cross-section (*left*) with the marked (turquoise) position of the composition profile that is shown on the right. The surface of the samples is to the left from the beginning of the turquoise line. The red dashed lines mark the boarders of the regions of partially amorphous layers, and the green dashed lines mark the boarders of the completely amorphous layers. The yellow arrows show an approximate region of chemical changes. *Right*: the black dashed lines in the graphs mark an approximate depth, *d*, under which the composition does not change significantly.

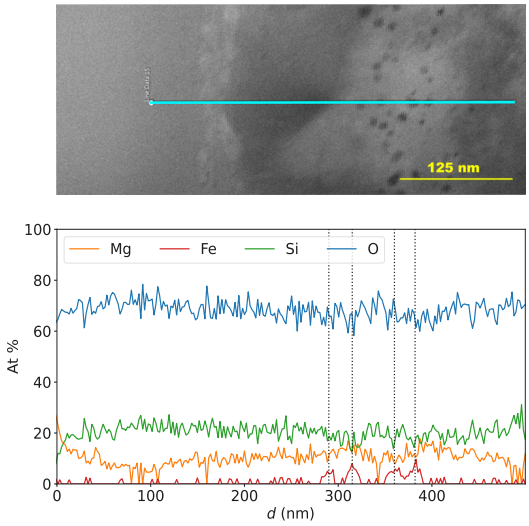

Fig. 7. Line scan through the area of nanophase Fe particles. *Top*: bright-field scanning transmission electron microscopy image of an area rich in nanophase Fe particles in the olivine sample irradiated by laser with marked position (turquoise) of the composition profile. *Bottom*: composition profile plot, with the dashed lines indicating approximate locations of nanophase Fe particles.

the same agent. Laser irradiation results in a thicker layer than ion irradiation.

Figure 7 shows a zoomed-in STEM-BF image of the zone containing nanoparticles in the OL irradiated by laser together with a composition profile. The locations of the nanoparticles correlate positively with the abundance of Fe. Also, based on the TEM-EDS point analysis, there is a significant increase in the amount of Fe in the particles, which points to the fact that these are indeed the npFe^0 particles.

4. Discussion

4.1. Observed changes

Our experiments show that the sample surface (viewed from the top) does not exhibit elemental abundance variations. We thus cannot discern between the two weathering agents by observation of changes in elemental abundances on the surface. The immediate sub-surface layers, on the other hand, experience changes in the abundance of some elements. These changes go even deeper into the sample than the amorphous zone. Sudden drops in elemental abundances are indicative of the presence of vesicles (see Fig. 6).

We see that there is a difference in the sub-surface structure of H$^+$- and laser-irradiated samples. Those irradiated by H$^+$ mainly show vesicular structures. We notice, as in Figs. 4a, b, that the OL has multiple layers of elongated vesicles, while the OPX shows more spherical and randomly distributed ones. We thus calculated the collisions in the two samples in our experimental conditions (5 keV H$^+$ ions penetrating into a layer of OL or OPX with chemical composition matching our samples) using the SRIM software (see Sect. 2.3). Based on the SRIM results, we plotted the distributions of the collision events with respect to the depth below the surface for the two samples, as shown in Fig. 8. We can see that both in OL and OPX, the collisions of H$^+$ ions within the sample happen in a very similar range of depths below the surface. These simulations thus do not explain the different distributions of vesicles we observe in our samples. Nevertheless, the SRIM simulations operate in the so-called zero-dose regime. This means that each ion, when impacting the sample in the simulation, behaves as if the sample was un-irradiated. It thus does not take into account the cumulative damage in the sample caused by the previous ions. Olivine is known to be more compliant to maintaining structural changes than pyroxene (Quadery et al. 2015). We therefore hypothesise that the collision events in the OL sample were distributed differently to the SRIM simulation as the incoming ions experienced a more altered environment than in the case of OPX, where the vesicles could have distributed more homogeneously.

The penetration depths of H$^+$ ions in OL and OPX, which we obtained from SRIM, agree with the similar thicknesses of the altered layers. In the OL and OPX, we observe that approximately the top 200 nm and 150 nm, respectively, are altered. The penetration depths are not significantly different; they are approximately 60 nm with dispersions of ≈30 nm.

The changes in the laser-irradiated samples are mainly caused by melting. The OPX sample shows a more global melting pattern spanning across individual laser spots, while in the case of the OL, the melting is rather localised to the area near the laser spot (Fig. 2). This observation agrees with the fact that OPX melts already at lower temperatures than OL. The melting temperature of OL of our composition is approximately 1820°C (Weizman et al. 1997; Ctibor et al. 2015), while for OPX it is approximately 1500 °C (Huebner & Turnock 1980). The OPX

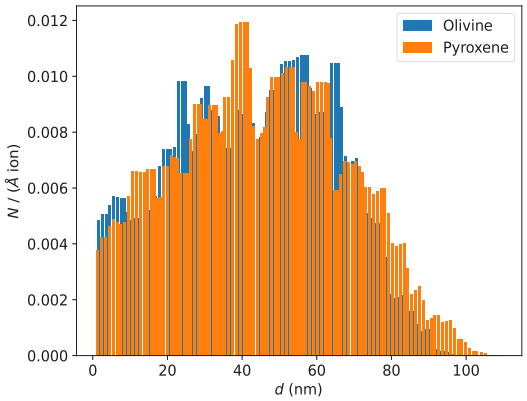

Fig. 8. Histogram of collision events in H^+-irradiated samples of olivine and pyroxene. *d* stands for the depth below the sample surface, and *N* is the number of events.

thus has a more developed molten surface full of melt drops and melt splashes than the OL sample.

For all the space weathering agents, the altered layers in the OL are thicker than those in the OPX irradiated by the same agent. This is potentially connected to the fact that OPX has a greater ability to heal the defects than OL, as was mentioned by Quadery et al. (2015).

4.2. Comparison with previous work

The images of our samples from TEM reveal stratigraphy in the sub-surface layers. Some samples show a purely amorphous layer, such as the laser-irradiated OL; other samples show a partially amorphous layer, such as the H^+-irradiated OL. Similar to our findings, Noguchi et al. (2014a,b) observed olivine- and pyroxene-rich Itokawa particles and found that their sub-surface structure may be divided into (three) zones. The first zone is composed of sputter and vapour deposits. We observed this only in the laser-irradiated samples. The second zone is composed of partially amorphous material, and the third zone is the underlying unchanged mineral. Weber et al. (2020) also observed nano-stratigraphy of the sub-surface layers in their laser-irradiated pressed pellets. In agreement with us, they found that the nano-stratigraphy differs for olivine and pyroxene samples. The thickness of the altered zone observed in our samples is similar to the work of Fazio et al. (2018) and Weber et al. (2020).

Our samples contain abundant vesicles, which are small in the H^+-irradiated samples and large in the OPX irradiated by laser. Demyk et al. (2001) observed vesicles in their samples irradiated by He^+ ions as well. The sizes they saw are similar to those in our ion experiment. Even Laczniak et al. (2021) observed vesicles in olivine irradiated by H^+ and He^+ ions. Based on Laczniak et al. (2021), the vesicles are usually smaller than 80 nm for the Moon, which agrees with our H^+ experiments. Kaluna et al. (2018) carried out ion irradiations of pristine lunar soils, predominantly made of pyroxene with accessory olivine, and in agreement with us they found vesicles in glassy rims, with sizes similar to our OL case. Olivine- and pyroxene-rich Itokawa particles contain lenticular vesicles that were, based on Matsumoto et al. (2015), created by He^+-irradiation. Lenticular vesicles with a longer side parallel to the surface, observed not only by Matsumoto et al. (2015) but also Noguchi et al. (2014b), match our H^+-irradiated OL observations.

Blisters observed in the H^+-irradiated samples are significantly larger than those observed on natural samples. For example, the olivine-rich samples from asteroid Itokawa showed abundant blistering with blister sizes around 30 nm (varying by a factor of two; see Dobrică & Ogliore 2016). This may be because Itokawa grains are young and not exposed to the space environment for a long time, as suggested by the presence of completely unblistered regions on the grains (our samples represent approximately 10^3 yr of exposure at 3 au). We only observe blisters in the H^+-irradiated samples. In agreement, Matsumoto et al. (2018) observed blisters in the surroundings of the micrometeoroid impact craters but never inside them.

There are several possible reasons for the discrepancy in the blister size between our samples and natural samples. One of them may be the five-times-higher energy of individual H^+ ions we used for irradiation compared to the standard solar wind. Demyk et al. (2001) used standard solar wind energy of He^+ ions and a five-times-higher fluence than in our experiment. As a result, the bubbles they observed did not exceed the size of ≈400 nm. Also, the size of blisters may be influenced by the crystal orientation to the incident angle of the ion beam of low-Ca pyroxene as was pointed out by Matsumoto et al. (2015). Based on Sznajder et al. (2018), the size of blisters is proportional to the irradiation time, which matches the observations of Demyk et al. (2001). We disregard the too high fluence as a reason for the discrepancy as Demyk et al. (2001) and Keller et al. (2015) used a higher fluence and did not obtain such large blisters. Matsumoto et al. (2013), on the other hand, also used a five-times-higher fluence and obtained blisters as large as 3 µm (which is larger than blisters in our experiment). However, in their experiments, H_2^+ ions were used, not H^+, which results in a significant difference.

We observe chemical changes in sub-surface layers in agreement with Laczniak et al. (2021), who observed Mg-depleted, Si-enriched layers in their samples. Their explanation is that this may be due to preferential sputtering of Mg, which leads to non-stochiometric concentrations (see also, for example, Cassidy & Hapke 1975; Lantz et al. 2017). Similarly to us, they found that the chemically distinct layer is thicker than the visually observed one, which may be due to radiation-enhanced diffusion that makes sputtered atoms mobile.

The only sample in which we identify $npFe^0$ particles is the laser-irradiated OL. Weber et al. (2020) observed similar behaviour. While the $npFe^0$ particles were observed in olivine, they were sparse and smaller or completely absent from pyroxene in their experiment with nanosecond laser pulses.

The $npFe^0$ particles we observe are of similar size or smaller than in other experiments or natural samples. Nanoparticles of a similar size have been identified in the laser experiments of Wu et al. (2017) or in ion-irradiated pristine lunar soils and mature lunar soils from the Apollo 17 mission (Kaluna et al. 2018; Kling et al. 2021). Based on Noguchi et al. (2014a,b), Itokawa grains contain only small $npFe^0$ particles (5 nm) induced by solar wind ions, while particles from the Moon have greater nanoparticle size variation (Noble et al. 2007). Larger $npFe^0$ particles were observed, for example, by Fazio et al. (2018) and Weber et al. (2020). The greater size of nanoparticles may be due to a slightly different set-up of the laser compared with our set-up (e.g. smaller spot size resulting in a higher concentration of energy or greater energy and repeating pulses). As Fulvio et al. (2021) noted, the laser spot size significantly influences the resulting craters. Also, the difference in the forsterite content of our samples and samples in Fazio et al. (2018) could have

played a role. The nature of the sample was different as well; Fazio et al. (2018) used a monocrystalline sample, while we used a porous pressed powder surface, which may influence the laser sputtering. Fazio et al. (2018) found $npFe^0$ particles both in the glassy layer and in the polycrystalline layer below it. In our case, the majority of the $npFe^0$ particles are situated below the glassy layer.

Notes on laser set-up

The main difference between (previously widely used) ns laser pulses and fs laser pulses is in the interaction between the laser and the material. Nanosecond pulses mainly cause heating and melting of a target. In this regime, a thermal wave propagates through the material, which results in a significant and widespread layer of melt. In the fs regime, on the other hand, the thermal conduction to the target may be, in the first approximation, neglected (Chichkov et al. 1996). Because of the short timescale of the pulse, the interaction proceeds in a different way. The material may undergo fragmentation and immediate transformation from solid to vapour. The brevity of the pulse also disables the interaction of the laser with the vapour plume. At high peak irradiance, the material undergoes melting, which is only confined to the area of the laser spot, which contrasts with the ns regime (Fazio et al. 2018; Perez & Lewis 2003).

The wavelength of the laser pulse we used (800 nm) is different to the usually applied Nd-YAG or ultraviolet (UV) lasers (1064 nm or 248 nm see, for example, Sasaki et al. 2001; Brunetto et al. 2006; Matsuoka et al. 2015). As Brunetto et al. (2006) noted, the 1064-nm pulses cause the laser to behave as a heat source, resulting in uncontrolled melting. The UV pulses, on the other hand, cause direct breaking of the bonds in the target with little damage to the surrounding material. The wavelength of our laser experiment is closer to the 1064-nm than to the UV experimental set-up. Also, both, the 800 and 1064 nm lasers operate at the wavelengths matching the main absorptions in the olivine (and pyroxene) materials. Nevertheless, the evaluation of the differences in the influence of the two set-ups on the final state of the material is beyond the scope of this article, and we refer the reader to the original publication (Fazio et al. 2018) for a deeper discussion of the experimental set-up.

4.3. Sub-surface structure and reflectance spectra

While the OPX irradiated by laser shows a major layer of amorphous material, for all the other types of irradiation, the sub-surface alteration does not exceed 300 nm. If we compare this information with the spectral evolution (Fig. 5), we see that at shorter wavelengths the thickness of the altered layer is similar to the wavelength of light. With longer wavelengths, this does not hold. The incident light at longer wavelengths probes more deeply into unaltered layers, and the spectral change is thus smaller as the spectrum represents a mixture of the fresh and mature material.

The H^+ irradiation causes a similar sub-surface change in the OL and OPX sample (Fig. 4), that is partial amorphisation of topmost 200 nm and 150 nm, respectively. The subsequent spectral change is characterised by a strong decrease in reflectance in the VIS and nearly no change in the NIR region. This darkening may be explained by a change in the imaginary part of the refractive index after amorphisation that can be of up to several orders of magnitude (see, for example, olivine refractive indices in Dorschner et al. 1995 and Zeidler et al. 2011). The absorption in the volume is a function of the thickness of the volume compared to the wavelength. As the thickness of the amorphous layer is small (a few hundred nanometres), the VIS wavelengths are absorbed much more than the longer wavelengths. The partially amorphous layer is thicker in the OL sample, which causes the greater change in the spectrum (see Fig. 5). The small vesicles in the samples probably cause scattering, which may mildly increase the brightness. Nevertheless, this effect seems to be minor compared to the darkening.

Table 1. Sub-surface structure for different materials and irradiation sources.

	$npFe^0$	Vesicles	Amorphization	t (nm)
OL – H^+	No	Yes	Partial	200
OL – laser	Yes	No	Full	300
OPX – H^+	No	Yes	Partial	150
OPX – laser	No	Yes	Full	400–2500

Notes. OL stands for olivine, OPX for pyroxene, $npFe^0$ for nanophase Fe particles, and t for thickness of the altered layer. The individual columns state whether we identified the object in our samples or not.

The OL irradiated by laser shows a similar spectral change to the one irradiated by H^+, but the absolute value of the change differs. The reason for this may be that the amorphous layer is thicker and the amorphisation in the laser-irradiated sample is complete compared to the partial amorphisation in the ion irradiation case. Also, the laser-irradiated samples show a molten surface, which is smoother than the original surface. As a result, the spectra darken because of the smaller contribution of the reflection from the rough surface. Laser irradiation of OL causes the additional creation of $npFe^0$ particles. Their presence also causes a slight change in the NIR spectral slope, as observed in previous work (see, for example, Pieters & Noble 2016).

The OPX irradiated by laser shows a different sub-surface structure to the OL, the main features being a thick glassy layer and plenty of large (tens to hundreds of nm) vesicles. The light scatters on the vesicles, which decreases the effect of darkening compared to the other cases. On the other hand, we hypothesise that the significant amorphous layer makes the material in the top layers compact, causing that the scattering on the microroughness is disabled. Due to the presence of large vesicles, the light penetrates deep into the material, where the volume scattering and absorption are enhanced, which may hypothetically increase the absorption bands' depths compared to the pristine sample, where surface scattering on the individual grains diminishes the contribution of the volume absorption. All these observations are summarised in Table 1.

4.4. Application to Solar System research

Based on our findings we can make the following prediction of the sub-surface and spectral evolution due to space weathering. In the first 10^3–10^4 yr after exposure of the material to the space environment, the solar wind dominates (e.g. Blewett et al. 2011) and the airless planetary surfaces will mainly suffer from partial amorphisation, which will induce rapid changes in the VIS spectral slope. Only later will small (<5 nm) $npFe^0$ particles appear, as we now see in Itokawa particles brought by the Hayabusa mission, which will also mildly influence the NIR slope. On timescales longer than 10^8 yr, we expect micrometeoroid bombardment to become significant (Blewett et al. 2011;

Noguchi et al. 2011), which may create larger npFe^0 particles (as seen in the OL sample) and/or large vesicles in thick amorphous layers (as seen in the OPX sample). The OPX changes will not influence spectral slope any more but will have an effect on absorption bands, as we observe in asteroids (433) Eros and (4) Vesta.

5. Conclusions

Our analyses revealed a significant difference in the morphology of laser- and ion-irradiated surfaces. While ions (simulating the influence of solar wind) induced the creation of blisters, laser shots (representing micrometeoroid impacts) caused melting with the associated creation of bubbles and melt splashes. We did not identify any spatial variation in chemical abundances of the surfaces irradiated by laser and by H^+, which means that the two space weathering agents are not distinguishable by this analysis.

Samples irradiated by H^+ showed a very similar sub-surface structure rich in small vesicles in thin (up to 200 nm), partially amorphous layers. The laser-irradiated OL showed a fully amorphous layer below which we identified npFe^0 particles. The laser-irradiated OPX contained, unlike the previous cases, a thick amorphous layer full of large vesicles.

Based on a comparison of the irradiation-induced structures and the changes in reflectance spectra, we found that the thickness and the structure of the amorphous layer have a major influence on the spectra. In both materials, H^+ irradiation resulted mainly in VIS spectral slope changes due to the thickness of partially amorphous layers being comparable to VIS wavelengths. Spectral slope changes throughout the VIS-NIR wavelengths observed in the olivine sample irradiated by laser resulted from the presence of thicker, completely amorphous layers together with the presence of the npFe^0 particles. The pyroxene sample irradiated by laser showed the thickest, entirely amorphous layer that, in combination with large vesicles, probably caused changes of the absorption bands' depths and no continuum changes.

We may thus predict the sub-surface and spectral evolution of material exposed to the space environment with time: initially thin, partially amorphous layers with a thickness comparable to the wavelength of observation will cause significant changes to the VIS spectral slope. The later appearance of npFe^0 particles will also influence the NIR slope, and a subsequent increase in the thickness of the amorphous layer and vesicle size will induce only mild darkening and modification of depths of the absorption bands.

Acknowledgements. The authors would like to express many thanks to the anonymous referee and to the editor for thorough corrections and comments on this manuscript. This work was supported by the University of Helsinki Foundation and the Academy of Finland project nos 325805, 1335595 and 293975, and it was conducted with institutional support RVO 67985831 from the Institute of Geology of the Czech Academy of Sciences. The authors acknowledge funding from Charles University (Project Progres Q47). This work has been realized within the research infrastructure SUSEN established in the framework of the European Regional Development Fund in project CZ.1.05/2.1.00/03.0108 and of the European Structural and Investment Funds in project CZ.02.1.01/0.0/0.0/15_008/0000293.

References

Blewett, D. T., Coman, E. I., Hawke, B. R., et al. 2011, J. Geophys. Res. (Planets), 116, E02002
Brunetto, R., Romano, F., Blanco, A., et al. 2006, Icarus, 180, 546
Brunetto, R., Lantz, C., Ledu, D., et al. 2014, Icarus, 237, 278
Burns, R. G. 1989, Mineralogical Mag., 53, 135
Cassidy, W., & Hapke, B. 1975, Icarus, 25, 371
Chichkov, B. N., Momma, C., Nolte, S., von Alvensleben, F., & Tünnermann, A. 1996, Appl. Phys. A: Mater. Sci. Process., 63, 109
Chrbolková, K., Brunetto, R., Ďurech, J., et al. 2021, A&A, 654, A143
Ctibor, P., Neufuss, K., Pala, Z., Kotlan, J., & Soumar, J. 2015, Roman. Rep. Phys., 67, 600
Demyk, K., Carrez, P., Leroux, H., et al. 2001, A&A, 368, L38
Dobrică, E., & Ogliore, R. C. 2016, Earth Planets Space, 68, 21
Dorschner, J., Begemann, B., Henning, T., Jaeger, C., & Mutschke, H. 1995, A&A, 300, 503
Fazio, A., Harries, D., Matthäus, G., et al. 2018, Icarus, 299, 240
Fiege, K., Guglielmino, M., Altobelli, N., et al. 2019, J. Geophys. Res. (Planets), 124, 1084
Fulvio, D., Fuks Maron, L., Cires Perez, Y., Tahir, & Del Rosso, T. 2021, Icarus, 366, 114532
Hapke, B. 1965, Ann. N. Y. Acad. Sci., 123, 711
Hapke, B. 2001, J. Geophys. Res., 106, 10039
Hapke, B. W., Cohen, A. J., Cassidy, W. A., & Wells, E. N. 1970, Geochim. Cosmochim. Acta Suppl., 1, 2199
Huebner, S. J., & Turnock, A. C. 1980, Am. Mineralogist, 65, 225
Kaluna, H. M., Bradley, J. P., Ishii, H. A., & Gillis-Davis, J. J. 2018, in 49th Annual Lunar and Planetary Science Conference, 2421
Keller, L. P., & McKay, D. S. 1993, Science, 261, 1305
Keller, L. P., & McKay, D. S. 1997, Geochim. Cosmochim. Acta, 61, 2331
Keller, L. P., Christoffersen, R., Dukes, C. A., Baragiola, R., & Rahman, Z. 2015, in 46th Annual Lunar and Planetary Science Conference, 1913
Kling, A., Thompson, M., Greer, J., & Heck, P. 2021, Microsc. Microanal., 27, 2260
Laczniak, D. L., Thompson, M. S., Christoffersen, R., et al. 2021, Icarus, 364, 114479
Lantz, C., Brunetto, R., Barucci, M. A., et al. 2017, Icarus, 285, 43
Loeffler, M. J., Dukes, C. A., & Baragiola, R. A. 2009, J. Geophys. Res. (Planets), 114, E03003
Matsumoto, T. M., Tsuchiyama, A. T., Takigawa, A. T., et al. 2013, in 44th Annual Lunar and Planetary Science Conference, 1441
Matsumoto, T., Tsuchiyama, A., Miyake, A., et al. 2015, Icarus, 257, 230
Matsumoto, T., Hasegawa, S., Nakao, S., Sakai, M., & Yurimoto, H. 2018, Icarus, 303, 22
Matsuoka, M., Nakamura, T., Kimura, Y., et al. 2015, Icarus, 254, 135
Noble, S. K., Pieters, C. M., & Keller, L. P. 2007, Icarus, 192, 629
Noguchi, T., Nakamura, T., Kimura, M., et al. 2011, Science, 333, 1121
Noguchi, T., Bridges, J. C., Hicks, L. J., et al. 2014a, Earth Planets Space, 66, 124
Noguchi, T., Kimura, M., Hashimoto, T., et al. 2014b, Meteoritics Planet. Sci., 49, 188
Penttilä, A., Martikainen, J., Gritsevich, M., & Muinonen, K. 2018, J. Quant. Spec. Radiat. Transf., 206, 189
Perez, D., & Lewis, L. J. 2003, Phys. Rev. B, 67, 184102
Pieters, C. M., & Noble, S. K. 2016, J. Geophys. Res. (Planets), 121, 1865
Pieters, C. M., Taylor, L. A., Noble, S. K., et al. 2000, Meteorit. Planet. Sci., 35, 1101
Quadery, A. H., Pacheco, S., Au, A., et al. 2015, J. Geophys. Res. (Planets), 120, 643
Sasaki, S., Nakamura, K., Hamabe, Y., Kurahashi, E., & Hiroi, T. 2001, Nature, 410, 555
Sasaki, S., Hiroi, T., Nakamura, K., et al. 2002, Adv. Space Res., 29, 783
Statham, P. J. 1977, Anal. Chem. (United States), 49, 2149
Sznajder, M., Geppert, U., & Dudek, M. 2018, npj Mater. Degrad., 2, 3
Weber, I., Stojic, A. N., Morlok, A., et al. 2020, Earth Planet. Sci. Lett., 530, 115884
Wehner, G. K., Kenknight, C. E., & Rosenberg, D. 1963, Planet. Space Sci., 11, 1257
Weizman, A., Prialnik, D., & Podolak, M. 1997, J. Geophys. Res., 102, 9205
Wu, Y., Li, X., Yao, W., & Wang, S. 2017, J. Geophys. Res. (Planets), 122, 1956
Yamada, M., Sasaki, S., Nagahara, H., et al. 1999, Earth Planets Space, 51, 1265
Zeidler, S., Posch, T., Mutschke, H., Richter, H., & Wehrhan, O. 2011, A&A, 526, A68
Ziegler, J. F., & Biersack, J. P. 1985, The Stopping and Range of Ions in Matter (Springer US), 93